The origin of magnetism in anatase Co-doped TiO_2 magnetic semiconductors

Yunjae Lee

PROMOTIECOMMISSIE

VOORZITTER *(Chairman)*:	Prof. dr. ir. A.J. Mouthaan	
SECRETARIS *(Secretary)*:	Prof. dr. ir. A.J. Mouthaan	Univ. Twente, EWI
PROMOTOR *(Supervisor)*:	Prof. dr. ir. W.G. van der Wiel	Univ. Twente, EWI
ASS.PROMOTOR:	Dr.ir. M.P. de Jong	Univ. Twente, EWI
REFERENT(EN) *(Referee(s))*:	Prof.dr. T. Dietl	Warszawa Univ., Poland
	Dr. O. Karis	Uppsala Univ., Sweden
LEDEN *(Members)*:	Prof. dr. ir. J.W.M. Hilgenkamp	Univ. Twente, TNW
	Prof. dr. J.C. Lodder	Univ. Twente, EWI
	Prof. dr. R.A. de Groot	Radboud Univ.
	Prof. dr. J. Aarts	Univ. Leiden

UNIVERSITEIT TWENTE.

MESA+ INSTITUTE FOR NANOTECHNOLOGY

nano ned

The research described in this thesis was carried out in the Nanoelectronics group of the MESA$^+$ Institute for Nanotechnology, University of Twente. The work was funded by NANONED, supported by the Ministry of Economic Affairs, the Netherlands.

Printed by: Wöhrmann Print Service, Zutphen

ISBN: 978-90-365-3082-8

The origin of magnetism in anatase Co-doped TiO_2 magnetic semiconductors

Dissertation

to obtain
the doctor's degree at the university of Twente,
under the authority of the rector magnificus,
prof. dr. H. Brinksma,
on account of the decision of the graduation committee,
to be publicly defended
on Thursday 7 October 2010 at 15:00

by

Yunjae Lee

born on 1 November 1976

In Daejon, South Korea

This dissertation is approved by

the promotor: Prof. dr. ir. W.G. van der Wiel
the assistant promotor: Dr.ir. M.P. de Jong

Contents

Chapter 1

Introduction

In Chapter 1, a brief introduction to semiconductor spintronics and dilute magnetic semiconductors (DMS) is given. A brief history of dilute magnetic semiconductors and a discussion of the present controversy about the origin of magnetism in transition metal doped oxides are given. Finally, the motivation and outline of the thesis are given.

1. 1 Spintronics

Conventional electronics has developed with the exploitation of the electronic charge properties of carriers in semiconductor materials, as can be seen in present electronic and optoelectronic semiconductor devices. For instance, various types of memory chips, information processors, and light emitting devices utilize the charge properties of carriers through materials by electrical control. However, the electron has another degree of freedom that can be used, namely spin, which is an intrinsic angular momentum of the electron. The spin state of an electron is represented by the spin quantum number, which can assume the values $+^1/_2$ (spin-up) and $-^1/_2$ (spin-down) with respect to a reference magnetic field. Spintronics or spin electronics refers to an emerging research area that focuses on employing spin in charge based electronics [1-2]. Spin dependent effects controlled by electrical and optical tools can render new functionalities into existing electronic devices or create new devices.

Spintronics has already shown its success by using ferromagnetic metals in the computer industry, in the form of hard disk drive (HDD) read heads which use the giant magneto-resistance (GMR) effect. GMR is the effect that the resistance depends on the relative magnetic orientation (parallel or anti-parallel) of neighboring magnetic layers in multilayer structures in which two (or more) ferromagnetic layers are separated by a non-magnetic metal spacer [3-4]. GMR-based technology formed the main contribution to the enormous increase of the storage density in hard disks during the last decade. This scientific success of spintronics received recognition in the form of the Nobel Prize in physics, 2007 which was awarded to Albert Fert and Peter Grünberg who discovered GMR independently in 1988. Nowadays, the tunneling magneto-resistance (TMR) effect is employed in HDD read heads and magnetic random access memory (MRAM), which are the most successful examples of spintronics in terms of applications (see Figure 1.1) [5].

Considering that the spin dependent effects in HDD and MRAM are present in metal-only (GMR) or metal-oxide (TMR) structures, however, semiconductor spintronics has much more room to progress than metal/oxide spintronics, since most electronic devices used in information processing are based on semiconductors. Among the most promising prospects of semiconductor spintronics are combined memory and logic at the single device level, enabling reprogrammable logic circuits, and the development of building blocks for solid state quantum computation. For successful spintronic applications

comprising non-magnetic semiconductors [6-7], spin injection, spin manipulation, and spin detection should be demonstrated. Alternatively, intrinsic spin-ordering can be realized, since semiconductors can be made magnetic by doping magnetic elements [8]. In dilute magnetic semiconductors, ferromagnetism is mediated by carriers that in turn can be controlled by doping, light, and electric fields, as has been well established in conventional charge-based semiconductor technology. Therefore dilute magnetic semiconductors are ideal candidates for semiconductor spintronic applications [8].

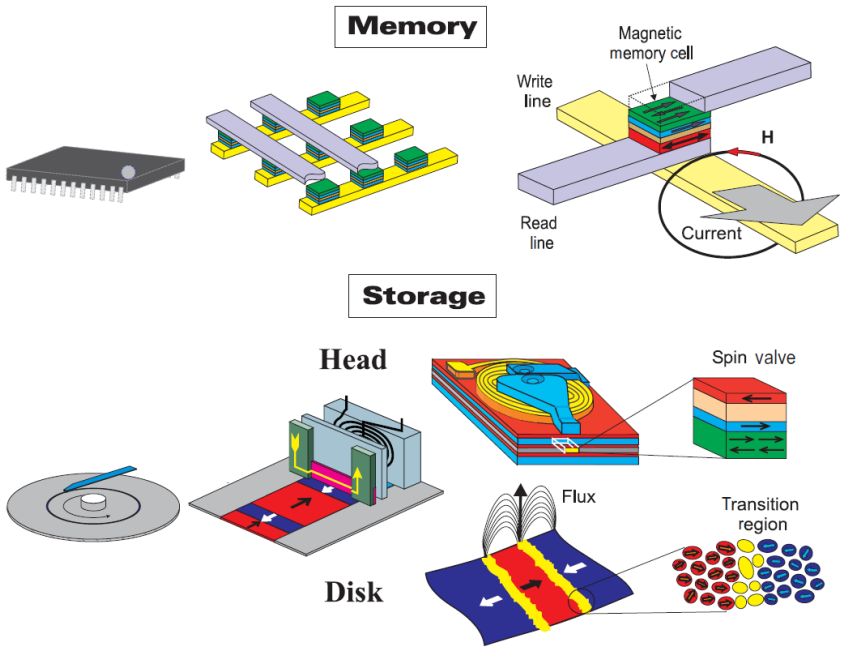

Figure 1.1 Illustration of various structures used for magnetic random access memory (MRAM) and hard disk drive (HDD) storage applications [5].

1.2 Dilute magnetic semiconductors

With respect to magnetic properties, semiconductors can be classified as magnetic semiconductors, dilute magnetic semiconductors, and non-magnetic semiconductors in terms of the amount and distribution of magnetic dopants as shown in Figure 1.2 [8]. Magnetic semiconductors such as magnetites, and europium- and chromium chalcogenides, have a periodic array of magnetically ordered spins in their crystal structure. These materials received intensive attention in the late 1960s since the exchange interaction between the electrons in the semiconductor bands and the localized electrons at the magnetic sites gives rise to a number of intriguing phenomena, but were abandoned later since they are difficult to grow and have a low Curie temperature, well below 100K [8].

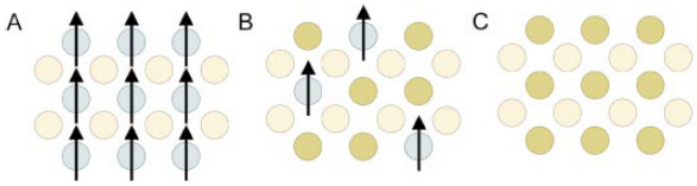

Figure 1.2 Three types of semiconductors: (A) a magnetic semiconductor, in which a periodic array of ordered spins is present; (B) a dilute magnetic semiconductor: a nonmagnetic semiconductor to which a dilute concentration of ions carrying an unpaired spin has been added; and (C) a nonmagnetic semiconductor [8]

Dilute magnetic semiconductors are doped with a small amount of magnetic ions, i.e. ions carrying unpaired spins, making nonmagnetic semiconductors magnetic. The magnetic interactions between the isolated spins in such systems are mediated by mobile carriers, which can be controlled by external parameters. One of the most technologically relevant examples is electric field control of ferromagnetism, in which a magnetic property is changed reversibly by applying an electric field in, for example, a field-effect transistor structure [9]. Since the ferromagnetism is mediated by holes in (InMn)As, the reduction of the hole density by applying a positive voltage at the gate leads to suppression of the ferromagnetic interaction between the magnetic moments, which results in paramagnetic behavior. Furthermore, control of the magnetization direction by an electric field and photo-induced ferromagnetism have been demonstrated in (InMn)As [10-11], suggesting that DMS can play a crucial role for semiconductor spintronics.

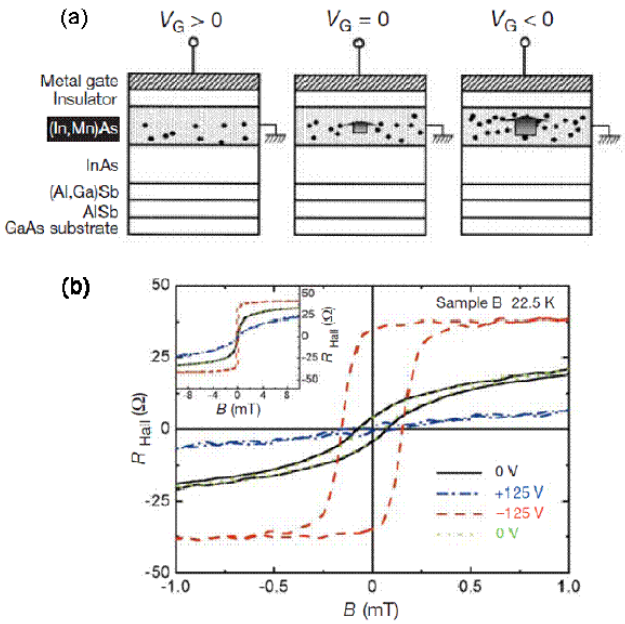

Figure 1.3 Field-effect control of the hole-induced ferromagnetism in dilute magnetic semiconductor (In,Mn)As field-effect transistors. Negative V_G increases the hole concentration, resulting in ferromagnetic behavior, whereas positive V_G induces the opposite effect, namely paramagnetic behavior in anomalous Hall measurements [9].

1.3 The controversial origin of room temperature magnetism in $Co:TiO_2$.

As can be seen in Figure 1.3 b, the measurement temperature for observing the electric field control of magnetism in (In,Mn)As is 22.5K, too low for practical applications. In its 125th anniversary issue, the journal "Science" raised the following question, as one of the 125 critical unanswered scientific questions, "Is it possible to create magnetic semiconductors that work at room temperature [12]?". Dietl suggested several possible candidates for DMS systems with high Curie temperatures, such as zinc oxides and gallium nitrides, based on the Zener model [13]. It triggered a tremendous combinatorial research effort that involved doping every transition metal into various nitrides and oxides in order to find a robust DMS. Various ferromagnetic transition-metal doped oxides and nitrides with high Curie temperature have been reported to date, but there is still strong controversy about the origin of ferromagnetism in these materials: Is it *intrinsic* or *extrinsic*? Intrinsic means here that the ferromagnetism between localized spins is mediated by delocalized carriers with long range interaction, satisfying the term "dilute" in dilute magnetic semiconductors, while extrinsic means that ferromagnetism originates from magnetic clusters. The initial theoretical prediction concerns p-type material, with the sp-d exchange interaction as a key ingredient for magnetism mediated by mobile charge carriers. However, the doped oxides exhibiting ferromagnetism contain oxygen vacancies and are n-type semiconductors. It seems unlikely that the originally proposed theory is applicable to such systems.

$Co:TiO_2$ is an interesting example, due to conflicting results that point toward both an intrinsic and extrinsic origin for ferromagnetism. The view of an intrinsic origin is supported by observing results such as room temperature ferromagnetism, anomalous Hall effect [14-17], magneto-optical dichroism [18-19], and TMR [20] which are typical phenomena in real DMS systems. However, there are also many reports claiming an extrinsic origin, such as the observation of secondary phases [21-22]. The controversy persists largely due to imprudent conclusions relying on measuring magnetism without careful structural study of secondary phases in the material under investigation. Here, we approach the problem with a broad set of complementary techniques containing structural probes, spectroscopy, and transport characterization in order to investigate the origin of magnetism in $Co:TiO_2$.

1.4 Thesis outline

Chapter 2 starts with giving a brief introduction of the reported DMS materials, and a description of several theoretical models for carrier mediated magnetism in DMS. This information is required to understand the ongoing controversy about the origin of magnetism in dilute magnetic oxides. Several extrinsic origins of magnetism and possible scenarios for intrinsic origins in $Co:TiO_2$ are discussed.

Chapter 3 mainly introduces the experimental methods employed in this thesis. First, substrate preparation and sample growth by pulsed laser deposition (PLD) are described. Then, structural characterization by high resolution transmission electron microscopy (HRTEM), energy filtered transmission electron microscopy (EF-TEM), x-ray diffraction

(XRD) are described. Finally, the principles of x-ray absorption spectroscopy (XAS) and x-ray magnetic circular dichroism (XMCD) are introduced.
Chapter 4 deals with magnetism and heterogeneity of Co in $Co:TiO_2$, studied by x-ray magnetic circular dichroism (XMCD) in combination with x-ray absorption spectroscopy (XAS) and energy filtered transmission electron microscopy (EFTEM). The suppressed XAS multiplet structure and observation of charge transfer multiplets are described in relation to heterogeneity. EFTEM results also are given.
Chapter 5 concerns the effects of introducing a TiO_2 buffer layer at the substrate/$Co:TiO_2$ interface on the magnetic and structural properties of anatase $Co:TiO_2$. The validity of AHE measurements for confirming intrinsic carrier mediated magnetism in DMS systems is discussed in parallel with EFTEM and VSM results. Furthermore, the role of impurity band conduction is investigated.
In Chapter 6, the fabrication and characterization of magnetic tunnel junctions (MTJs) containing an ultrathin interfacial layer of $Co:TiO_2$ is described. Spin transport phenomena in ultrathin layers of $Co:TiO_2$ are investigated in an MTJ configuration.

References

[1] S. A. Wolf, D. D. Awschalom, R. A. Buhrman, J. M. Daughton,S. von Molnar, M. L. Roukes, A. Y. Chtchelkanova, and D. M. Treger, Science **294,** 1488 (2001).

[2] I. Zutic, J. Fabian, and D. Sarma, Rev. Mod. Phys. **76**, 323 (2004).

[3] M. N. Baibich, J. M. Broto, A. Fert, F. Nguyen Van Dau, F. Petroff , P. Etienne, G. Creuzet, A. Friederich, and J. Chazelas Phys. Rev. Lett. **61**, 2472 (1988).

[4] G. Binasch, P. Grünberg, F. Saurenbach, and W. Zinn, Phys. Rev. B **39**, 4828 (1989).

[5] J. Stöhr, H.C. Siegmann, *Magnetism*, Spinger series in solid state science, Ch.1 p27.

[6] D. D. Awschalom, and M. E. Flatte, Nature Phys. **3** 153 (2007)

[7] J. Fabian, A. Matos-Abiague, C. Ertlera P. Stano, and I. Zutic, Acta Phys. Slovaca **57,** 565 (2007).

[8] H. Ohno, Science **281,** 951 (1998).

[9] H. Ohno, D. Chiba, F. Matsukura, T. Omiya, E. Abe, T. Dietl, Y. Ohno and K. Ohtani, Nature **408,** 944 (2000).

[10] D. Chiba, M. Yamanouchi, F. Matsukura, and H. Ohno, Scinece **301,** 943 (2003).

[11] S. Koshihara, A. Oiwa, M. Hirasawa, S. Katsumoto, Y. Iye, C. Urano, H. Takagi, and H. Munekata, Phys. Rev. Lett. **78**, 4617 (1997).

[12] D. Kennedy, and C. Norman, Science **309**, 82 (2005).

[13] T. Dietl, H. Ohno, F. Matsukura, J. Cibert, and D. Ferrand, Science **287**, 1019 (2000).

[14] H. Toyosaki, T. Fukumura, Y. Yamada, K. Nakajima, T. Chikyow, T. Hasegawa, H. Koinuma, and M. Kawasaki, Nat. Mater. **3**, 221 (2004).

[15] S. R. Shinde, S. B. Ogale, J. S. Higgins, H. Zheng, A. J. Millis, V. N. Kulkarni, R. Ramesh, R. L. Greene, and T. Venkatesan, Phys. Rev. Lett. **92**, 166601 (2004).

[16] K. Ueno, T. Fukumura, H. Toyosaki, M. Nakano, and M. Kawasaki, Appl. Phys. Lett. **90**, 072103 (2007).

[17] R. Ramaneti, J. C. Lodder, and R. Jansen, Appl. Phys. Lett. **91**, 012502 (2007).

[18] H. Toyosaki, T. Fukumura, Y. Yamada, and M. Kawasaki, Appl. Phys. Lett. **86**, 182503 (2005).

[19] Y. Hirose, T. Hitosugi, Y. Furubayashi, G. Kinoda, K. Inaba, T. Shimada, and T. Hasegawa, Appl. Phys. Lett. **88**, 252508 (2006).

[20] H. Toyosaki, T. Fukumura, K. Ueno, M. Nakano, and M. Kawasaki, Jpn. J. Appl. Phys. Part 2, **44**, L896 (2005).

[21] S.A. Chambers, Surf. Sci. Rep. **61,** 345 (2006).

[22] J.-Y. Kim, J.-H. Park, B.-G. Park, H.-J. Noh, S.-J. Noh, J. S. Yang, D.-H. Kim, S. D. Bu, T.-W. Noh, H.-J. Lin, H.-H. Hsieh, and C. T. Chen, Phys. Rev. Lett. **90**, 017401 (2003).

Chapter 2

Survey of dilute magnetic semiconductors

In Chapter 2, a brief introduction to dilute magnetic semiconductors (DMS) and the corresponding theory is given. The theoretical models proposed to explain the origin of ferromagnetism in DMS are described, followed by a discussion of the validity and limitations of these models. The current controversy about the origin of magnetism in dilute magnetic oxides is discussed, and a description of possible sources of extrinsic origins is given. Finally, possible scenarios of dilute magnetic oxides with a high Curie temperature, and the criteria for confirming real DMS behavior, are described.

2. 1 Introduction

Dilute magnetic semiconductors are semiconductors doped with a small amount of transition metal ions that introduce local magnetic moments. The coupling between localized moments and delocalized band-electrons renders unique properties of DMS, such as a giant spin-splitting of electronic states and indirect ferromagnetic exchange interactions between magnetic moments [1]. The latter is controlled by the manipulation of carriers by means of, e.g., doping, electric fields, optical excitation, and quantum structures, which are all key technologies within the well-established field of conventional, charge-based electronics. Therefore, the tunable ferromagnetism attainable in DMS is one of the leading areas of semiconductor spintronics.

The reported DMS materials are summarized in Table 2.1. Most of the early dilute magnetic semiconductors were based on Mn-doped 2-6 semiconductors such as tellurides, selenides and sulfides. The valence match (i.e. identical charge state) of the cation of the 2-6 host semiconductors to the dopant (Mn) makes it easy to prepare samples with a large amount of Mn [2-3]. Another important aspect of these 2-6 materials is that they are model materials in which localized spins and delocalized holes can be introduced and controlled independently, while dimensional effects can be tested by using quantum heterostructures [4]. Early studies of 2-6 DMS showed that the dominant magnetic interaction between Mn spins is antiferromagnetic. It has also been proven difficult to create p- or n-type carriers to mediate ferromagnetic interactions, resulting in paramagnetic, antiferromagnetic or spin glass behavior [2-3]. Irrespective of their effects on fueling magnetism research, 2-6 DMS already found their applications in flat panel displays, since efficient electroluminescence can be obtained by doping Mn. Ferromagnetism was observed at temperatures below 2K after the discovery of carrier induced ferromagnetism in Mn-based zinc-blende 3-5 compounds [5]. Recently, ZnCrTe showed room temperature ferromagnetism, causing a revival of 2-6 DMS. However, Kuroda suggested that ferromagnetism in these materials is caused by the formation of Cr rich phases [6, 7].

In 3-5 DMS, divalent transition metal ions (Mn) substitute for trivalent cations, thus generating holes whereas in 2-6 DMS, additional doping of p-type or n-type elements is required. The holes introduced by magnetic ions mediate a ferromagnetic interaction between magnetic ions in 3-5 DMS. The reported Curie temperatures of 3-5 DMS are generally higher than those in 2-6 DMS but are still too low for industrial applications. The highest record Curie temperature in 3-5 DMS is 173K, for (GaMn)As [8]. Recently, several oxides and nitrides have been reported to have room-temperature ferromagnetism. As a matter of fact, the studies aimed at searching robust room-temperature DMS were triggered by a mean field Zener model based on RKKY exchange interaction developed by Dietl, which predicts as promising candidates for room-temperature DMS *p*-type ZnO and *p*-type GaN [9]. Also because oxides and nitrides were already popular materials for light-emitting devices in the industry, this prediction triggering tremendous works to dope transition metal ions into oxides and nitrides. However, oxides are naturally n-type because of oxygen vacancies formed during the growth, while the mean field Zener model concerns *p*-type wide band gap materials. As an alternative theoretical model, Coey suggested that oxygen vacancies forming a spin-split impurity band may play a vital role in forming carrier-induced ferromagnetism [10]. It is also reported, however, that oxygen vacancies act as active sites for forming clusters [11]. In fact, there are comparable amounts of (1) reports that indicate that the magnetism originates from magnetic clusters in oxides against (2) reports that claim intrinsic magnetism. It should be noted that in the latter case a careful study of the structural properties of the materials is often lacking [12, 13].

Material class	Material	Ref
2-6	p-$Cd_{1-x}Mn_xTe$:N	5
	p-$Zn_{1-x}Mn_xTe$:N	4
	$Zn_{1-x}Cr_xSe$	14
	$Zn_{1-x}Cr_xTe$	15
4-6	$Pb_{1-x-y}Sn_yMn_xTe$	16
3-5	$In_{1-x}Mn_xAs$	17
	$Ga_{1-x}Mn_xAs$	18
	GaMnN	19
	GaCrN	20
	GaMnP:C	21
	GaMnSb	22
4	$Ge_{1-x}Mn_x$	23
Oxide	Co-TiO_2	24
	Mn-ZnO	25
	Co-SnO_2	26
	Fe-SnO2	27
	Cr-In_2O_3	28

Table 2.1 Representative reported dilute magnetic semiconductor materials

2. 2 Theoretical models for the origin of carrier mediated ferromagnetism

2.2.1 Mean-field Zener model

Direct d-d exchange interaction in DMS is much less prominent than in 3d transition metal systems due to its short range interaction, such that indirect p-d ferromagnetic exchange interaction is mediated by delocalized carriers in the sp-band. 2-6 and 3-5 Mn based DMS are well described by the mean field Zener model [9]. Dietl demonstrated the equivalence of the RKKY- and Zener model in the mean field- and continuous approximations, which forms the basis of the mean-field Zener model. In the 1950s, Zener suggested that delocalized band-carriers promote ferromagnetic ordering between localized spins in magnetic metals, by lowering the energy of the carriers associated with a spin-split band coupled to local magnetic moments. [29]. In relation to the RKKY interaction, it is important that the mean distance between the nearest neighbor spins in dilute magnetic semiconductors is much smaller than the Fermi wave length of the carriers. This leads to a ferromagnetic interaction, because the first sign change of the RKKY function is at $2K_FR = 2.87$, where $K_F = (3\pi^2 n)^{1/3}$ is the Fermi wave vector, R is the distance to a localized spin, and n is carrier concentration. In this limit, the Zener ferromagnetic exchange interaction becomes equivalent to that of the RKKY theory [9]. The schematic representation in Figure 2.1 shows that the energy of the system is lowered when the total spin of the hole-band has the same orientation as that of Mn, that is the total valence band *electron* spin is opposite to that of the Mn ions [30].

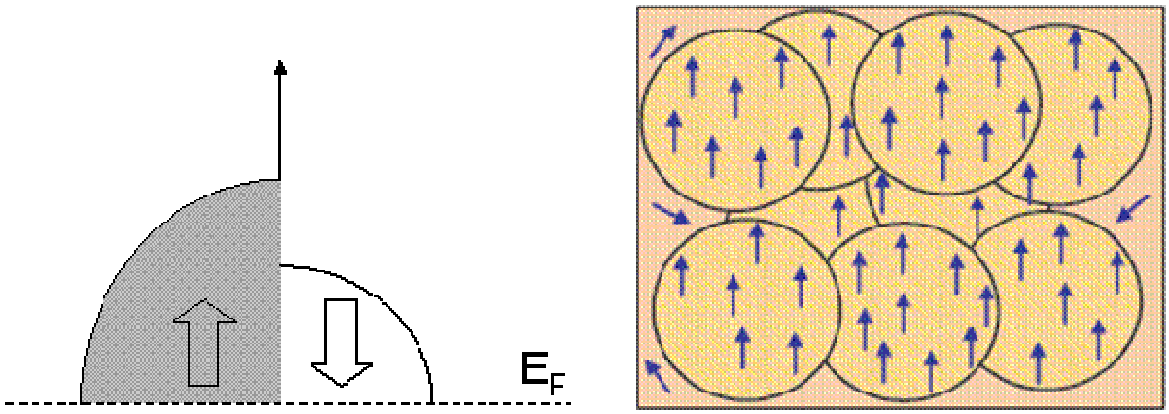

Figure 2.1 Schematic representation of carrier-mediated ferromagnetism in p-type DMS, according to a model proposed originally by Zener for metals. Owing to the p-d exchange interaction, ferromagnetic ordering of localized spins leads to spin-splitting of the valence band. The redistribution of the carriers between spin subbands lowers the energy of the holes [1, 30]. The doped holes should have a sufficient delocalization length and density, indicated by the overlapping spheres in the diagram on the right, such that they interact with a number of localized spins.

The mean-field Zener model is a phenomenological approach that introduces a single p-d exchange constant J_{p-d}, which can be calculated from experiments [9, 30]. It is based on the above described Zener p-d model, and the Kohn-Luttinger $k \cdot p$ theory of the valence band in tetrahedraly coordinated semiconductors, such as those that have zinc-blende and wurzite structures. This model takes into account spin-orbit coupling, $k \cdot p$ interaction in the valence band, and the effect of strain. The Curie temperature is calculated by determining the minimum of the Ginzburg-Landau free energy functional of the system [9]. According to this model, the Curie temperature can be increased by increasing the hybridization energy ($J \propto a^{-3}$) where a is the lattice constant, and by decreasing the spin orbit interaction [9]. This model proved its validity by explaining thermodynamic, micromagnetic, transport and optical properties [1]. It also predicted new candidate systems for room temperature dilute magnetic semiconductors in case of 5% Mn-doping and a carrier concentration of $3.5 \times 10^{20}/cm^3$. The general tendency for higher Curie temperatures in case of lighter elements stems from the corresponding increase of the p-d hybridization and reduction of the spin-orbit coupling. This suggests that wide band gap oxides and nitrides are promising candidates for DMS with high Curie temperatures, as represented in Figure 2.2 [2, 9].

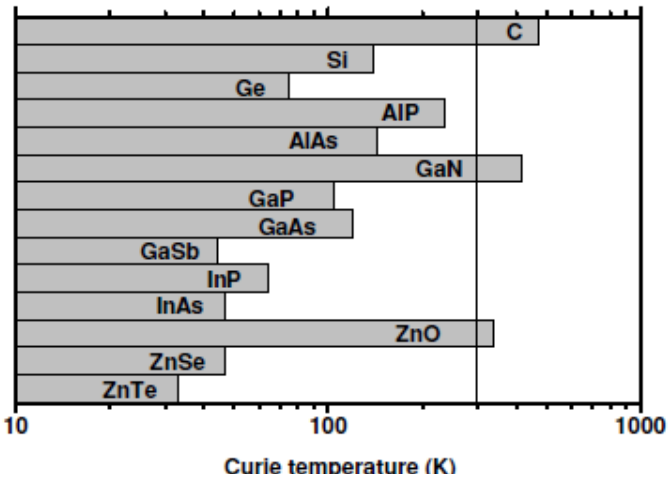

Figure 2.2 Computed values of the Curie temperature for various *p*-type semiconductors containing 5% of Mn and 3.5×10^{20} holes per cm^3 [2].

However, the mean field model may not be applicable to DMS containing magnetic impurities other than Mn, since the d-levels of other transition metals reside in the band gap and the corresponding correlation energy is relatively small [2]. The mean field Zener model assumes that holes are formed from states near the valence band edge. If the d-electrons participate in charge transport, the mean field Zener model is not appropriate for materials such as (Zn,Mn)O and (Ga,Mn)N. The hybridization increases when the energy gap between the occupied d-level and the hole states at the top of valence band becomes smaller [30].

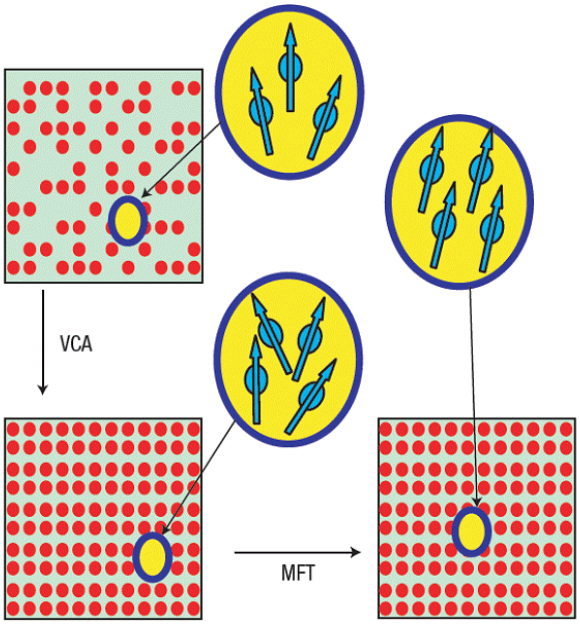

Figure 2.3 Two approximations of the mean field Zener model: the virtual crystal approximation (VCA) and mean field theory (MFT) [30]. Further explanation is provided in the text.

The mean field Zener model employs two approximations for long range coupling between Mn spins, illustrated in Figure 2.3. The first is the virtual crystal approximation (VCA), in which the random distribution of Mn ions is replaced by a periodic continuum with the same density [30]. The second approximation is the mean field theory (MFT), which neglects fluctuations of the spins of Mn ions. These approximations are not valid when strong p-d interactions and high carrier concentrations are present. The main message of the mean field Zener model, in relation to finding DMS with high Curie temperatures, is to look for systems with strong exchange interactions ($J_{p\text{-}d}$) and a large valence band density of states (DOS) [9, 30]. However, strong exchange coupling gives rise to more localized acceptor levels, and weaker effective coupling between Mn ions in the material. Then the VCA approximation fails since the Mn ions cannot be treated as a continuous medium. Furthermore, a large valence band DOS leads to a large effective hole mass (the DOS at the Fermi energy is proportional to the carrier effective mass) and also to more localized acceptor levels [30].

Additionally, a large DOS at the Fermi energy may also result in a variation of the sign of the RKKY exchange interaction, thus reaching the RKKY interaction region from mean field regime. If the concentration of holes is much larger than that of spins, a competition between ferromagnetic and antiferromagnetic interaction results, and then MFT fails. Upon decreasing the Mn concentration at a given hole concentration, the Kondo effect may appear [2]. These limitations of the mean field theory are illustrated in Figure 2.4 [31, 32]. In the mean field model, it should be noted that the transition temperature increases without limit, with both the exchange interaction strength and the hole density. However, these trends cannot continue indefinitely, because of localization effects induced by strong exchange interactions, and spin-frustration due to high carrier concentrations.

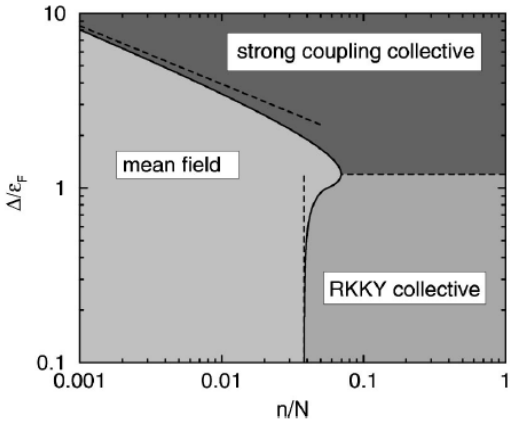

Figure 2.4 Schematic phase diagram indicating the requirements for ferromagnetic ordering in DMS. The y-axis represents the strength of the exchange coupling relative to the Fermi energy, and the x-axis the ratio between carrier- and local moment (i.e. spin) densities [31, 32].

2.2.2 Bound magnetic polaron (BMP) model

A limitation of the mean field Zener model is that charge carriers are treated as free carriers. It does therefore not explain the experimentally observed transport properties of insulating and ferromagnetic (GaMn)As, in particular the observation of a Mott variable range hopping behavior at low temperatures [33]. The "opposite" approach to the mean field Zener model is the bound magnetic polaron (BMP) model, which treats the carriers as quasi-localized states in an impurity band. In this limit, a localized hole in (GaMn)As exhibits antiferromagnetic exchange interaction with a number of magnetic impurities within its localization radius, leading to the formation of a bound magnetic bound polaron, illustrated in Figure 2.5. In contrast to the antiferromagnetic exchange interactions leading to their existence, the interaction *between* magnetic polarons is ferromagnetic. Since the effective radius of the magnetic polaron depends on the ratio of the exchange- and thermal energy, BMPs overlap at sufficiently low temperature. This gives rise to a ferromagnetic exchange interaction between percolated BMPs at low temperature. If the hole localization radius is much less than the distance between BMPs, disorder effects play a crucial role in the magnetic properties [34].

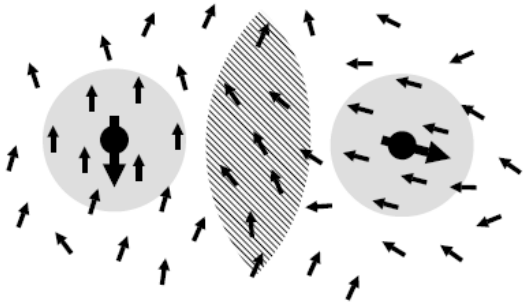

Figure 2.5 Interaction of two bound magnetic polarons (BMP). The small and large arrows show impurity and hole spins, respectively [33]. The shaded region indicates overlap affected by fields from the two BMPs.

2.2.3 Donor impurity band model

After the mean field Zener model prediction, finding promising candidates for room temperature DMS, such as p-ZnO and p-GaN, was of much interest in the scientific community. Beside the above predicted candidates, several oxides such as TiO_2, ZnO, SnO_2, and In_2O_3 [24-28] have been reported to show room-temperature ferromagnetism. However, a controversy arises from the fact that the mean field Zener model predicted *p*-type DMS systems, while the reported materials are *n*-type, except for a few cases. Furthermore, many of the reported dilute magnetic oxides have Curie temperatures *above* 300K. Later, Coey suggested the donor impurity band model, which is the extension of the above described BMP theory, to describe the properties of defect (e.g. oxygen vacancies) derived n-type dilute magnetic oxides [10]. Oxides are *n*-type, due to oxygen vacancies, and have a high dielectric constant. The main ingredients of the donor impurity band model are as follows. Shallow donors associated with defects form BMPs, via which ferromagnetic ordering of magnetic moments of dopants is mediated. At a sufficiently high BMP concentration, the polarons overlap, thus leading to a spin-split impurity band in the band gap and ferromagnetic ordering throughout the material. Figure 2.6 illustrates this ferromagnetic coupling between magnetic ions via an impurity band [10]. According to calculations based on this theory, a high Curie temperature is possible if the donor electron resides in the vicinity of magnetic impurity, even if the hybridization between the 3d levels and the conduction band states is just 1~2 % [10]. Considering that the 3d levels of transition metals in the series from Ti to Cu are below the conduction band, there are two possibilities for BMP formation. The first occurs near the beginning of the 3d series, where the majority 3d level crosses the Fermi level in the impurity band in Figure 2.6 (c), and the second is towards the end of the 3d series where the minority 3d level crosses the Fermi level in Figure 2.6 (b).

However, this donor impurity band model relies on donor formation from defects, which are also favored sites of forming metallic clusters. Furthermore, the weak s-d exchange interaction renders the model rather unrealistic. The exchange interaction between band electrons and the 3d-electrons of the magnetic ions consists of two contributions, 1) potential exchange and 2) kinetic exchange due to the hybridization. There always exists a potential exchange interaction, induced by the repulsive coulomb interaction between band- and d-electrons. This process tends to align the spins of the band electrons parallel to that of dopant magnetic moments. The kinetic exchange contribution, which stems from a reduction of kinetic energy by delocalization, is due to the hybridization of 3d levels with the s- and p-bands. At the Γ point, s-d hybridization is symmetry forbidden [35]. On the other hand, p-d hybridization is always allowed, which may be a reason why p-type materials are favored for DMS research. Summarizing, it is by now generally accepted that the impurity band model cannot explain the Curie temperatures above room temperature that have been observed in transition metal doped magnetic oxides and nitrides [36].

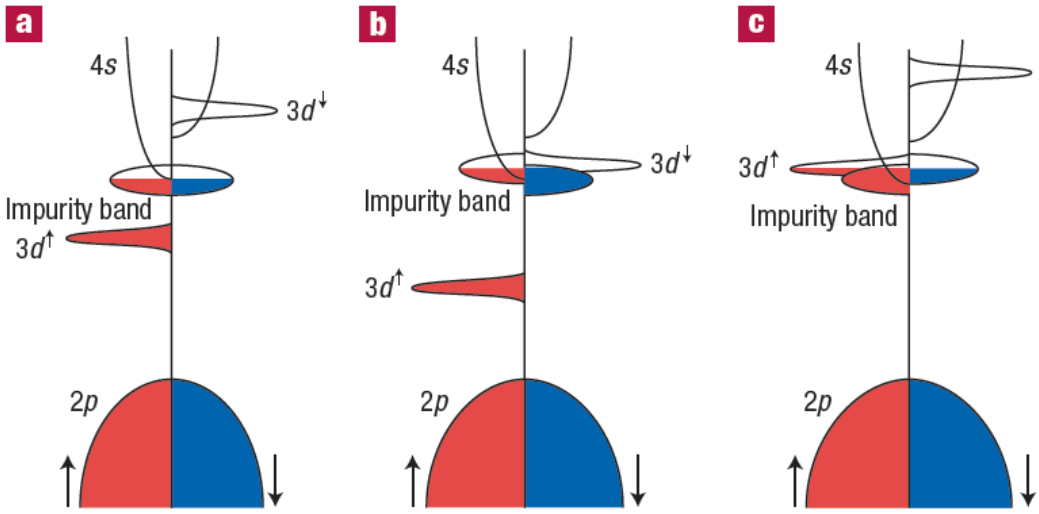

Figure 2.6 Schematic band structure of an oxide with 3d impurities and a spin-split donor impurity band. (a) A position of the 3d level for which the Curie temperature is low and the splitting of the impurity band is small. (b) and (c) show cases in which the minority- (b) or majority (c) 3d-states interact with the spin-split donor impurity band [10].

2. 3 Extrinsic origins of ferromagnetism in transition metal doped oxides

The undoubtedly high Curie temperatures, the largely varying magnetic moments of the dopants reported, and non-reproducibility of samples aggravates the controversy about the origin of ferromagnetism in transition metal doped oxides [36]. Possible origins have been suggested such as metallic clusters [12], spinodal phase separation [1, 7], contamination [36], d^0 magnetism [37], uncompensated spins at the surface of antiferromagnetic nanocrystal [38] and measurement artifacts [36]. The first report of a room temperature ferromagnetic oxide is Co:TiO_2 [24]. The view of an intrinsic origin of ferromagnetism was supported by scanning superconducting quantum interference (SQUID) results, confirming no evidence of metallic clusters. In addition, x-ray diffraction (XRD), and high resolution transmission electron microscopy (HRTEM) measurements also did detect clusters. However, these techniques all have their own limits for detecting tiny clusters (see e.g. Chapter 5 concerning XRD). Besides metallic clusters, spinodal phase separation, with rich and poor concentrations of dopants, is formed due to the limited solubility of the dopants. Spinodal phase separation is different from precipitation, in that the spinodally decomposed phase accommodates the same crystal structure as the host semiconductor, such that it is not easy to detect experimentally [1]. Figure 2.7 shows a TEM image of a Mn-rich (GaMn)As nanocrystal embedded in host GaAs matrix. It shows that the MnAs cluster (marked as 1) and GaAs (marked as 2) have the same symmetry, i.e. zinc-blende (ZB) type symmetry [39]. Spinodal decomposition induces these nanoclusters featuring a large concentration of the transition metal dopant, which may account for the current puzzle of high Curie temperatures reported for a large class of DMS and related oxides in which the concentration of transition metal dopants is far below the percolation limit for nearest-

neighbor coupling, and the carrier density is not enough to mediate a long-range ferromagnetic exchange interaction [1]. Interestingly, the presence of spinodal-decomposition-induced magnetic nanocrystals results in enhanced magneto-optical and magneto-transport phenomena, opening the possibility of controlled nano-crystal growth for device applications [1].

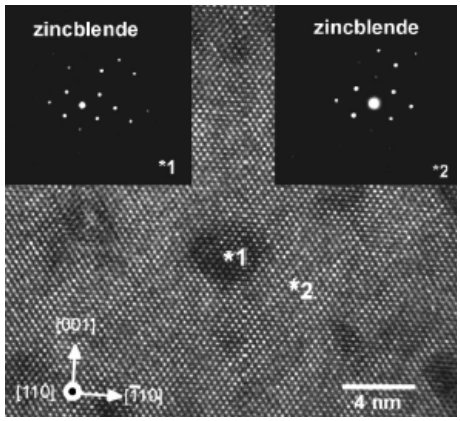

Figure 2.7 A TEM lattice image and two diffraction patterns of the same sample: *1 is from a MnAs cluster and *2 is from the GaAs matrix [39].

Contamination can also be a possible origin of ferromagnetism. It is already reported that handling samples with stainless steel tweezers gives rise to a source of magnetic signal [40]. In Figure 2.8, a Si wafer contaminated by stainless-steel tweezers leads to ferromagnetic behavior. The use of marker pens, and small particles remaining from calibration samples in vibrating sample magnetometry (VSM) can be also possible sources of magnetic signals. Another extrinsic source for magnetic signals may result from sharing deposition facilities with other users, since contamination can affect samples during the depositions. It is therefore good practice to check samples before and after deposition of the magnetic thin films by magnetometry, to exclude the effects of contamination.

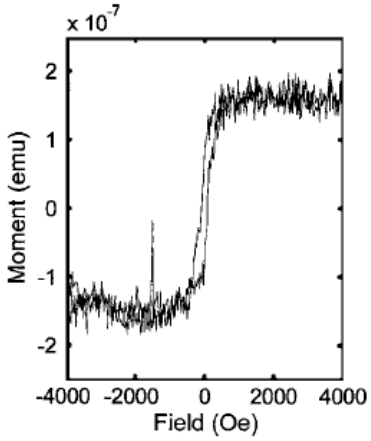

Figure 2.8 Magnetic moment measured from a silicon wafer after contamination by stainless-steel tweezers [40].

2. 4 Controversy about the origin of ferromagnetism in Co:TiO_2 dilute magnetic oxide

Co:TiO_2 is the first reported dilute magnetic oxide with high Curie temperature, after the mean field Zener model prediction, and followed by an avalanche of reports on the observation of room temperature ferromagnetism in various oxides such as ZnO, SnO_2, In_2O_3 etc. [12]. Among all dilute magnetic oxides (DMOs), only Co:TiO_2 has been reported consistently to show ferromagnetism at room temperature. TiO_2 has three polymorphs, namely rutile, anatase and brookite, as illustrated in Figure 2.9 [41]. Ferromagnetism has been reported in the rutile and anatase phases. The choice of the substrate determines the phase of the TiO_2 thin films. On $LaAlO_3$ (LAO) and $SrTiO_3$ (STO), the anatase phase is grown with lattice mismatch -0.26% and -3.1%, respectively. Anatase films are obtained independent of the growth method. Films grown on Si or Al_2O_3 always produce the rutile phase. Since rutile is known to be the most stable phase, it is often observed as outgrowths formed in anatase thin films. Figure 2.10 shows a TEM image of rutile nanocrystals in a pure (i.e. undoped) anatase TiO_2 thin film grown on LAO [42]. Related to this issue, there are some known factors to play a role for distributing Co homogeneously. Chambers *et al.* suggested that a low growth rate (0.01nm/s) in molecular beam epitaxy (MBE) leads to a layer-by-layer growth and homogenous Co distribution in the film [42]. In contrast, a higher rate (0.04nm/s) leads to a large density of rutile phases to which Co segregates above 550^0C. Post-annealing is reported to result in redistribution of the Co atoms but also an increased clustering of Co within the film [41]. Another possible factor for influencing the Co distribution could be the oxygen vacancies. With decreasing oxygen pressure during growth, an increasing tendency of Co to cluster is reported [41].

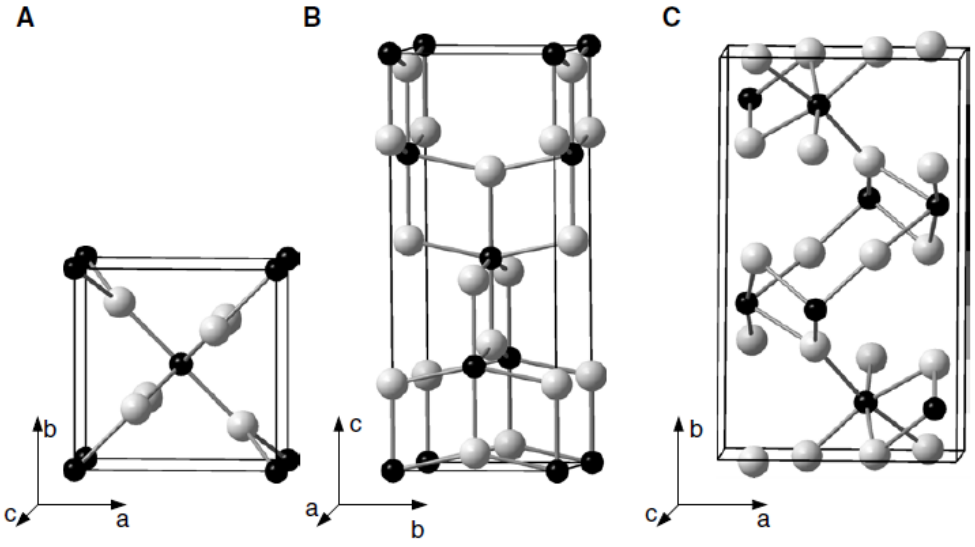

Figure 2.9 Different polymorphs of TiO2: (A) rutile, (B) anatase, and (C) brookite.

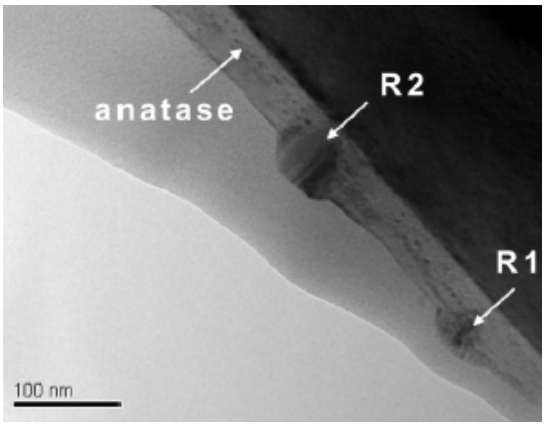

Figure 2.10 Bright-field TEM image for 50-nm pure TiO_2 on $LaAlO_3(001)$. Rutile nanocrystals are indicated by R1 and R2 [42] .

Initially, Chambers *et al.* suggested carrier mediated ferromagnetism by showing that ferromagnetic behavior is enhanced by increasing the carrier concentration in anatase Co:TiO_2 thin films [42]. Carrier mediated ferromagnetism is further supported by the observation of anomalous Hall effects (AHE) and magneto optical dichroism in rutile, and anatase Co:TiO_2 [43-46]. AHE is the well known ferromagnetic response of carriers in ferromagnetic materials. In Figure 2.11, it is shown that rutile Co:TiO_2 represents the anomalous Hall effect, while its magnetic field dependence is similar to that of the magnetization measured by magnetometry [47]. Toyosaki *et al.* measured the AHE and magneto optical dichroism in rutile samples, and found a correlation between them as a function of carrier concentration and external magnetic field. These observations suggest that carriers enhance the ferromagnetic exchange interactions between isolated Co magnetic moments in Co:TiO_2 [48].

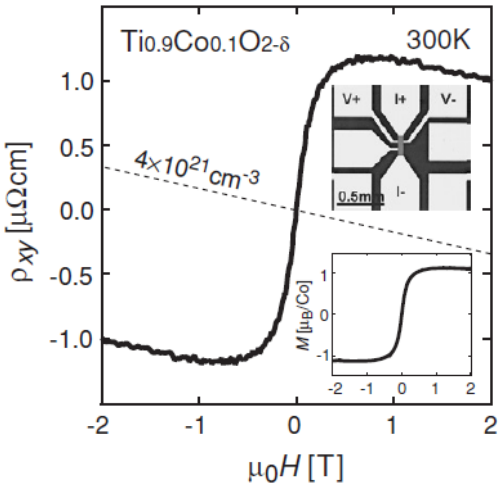

Figure 2.11 Magnetic field dependence of the Hall resistivity for rutile Co-doped TiO_2 at 300 K. The bottom inset is the magnetic field dependence of the magnetization for the same sample at 300 K [47].

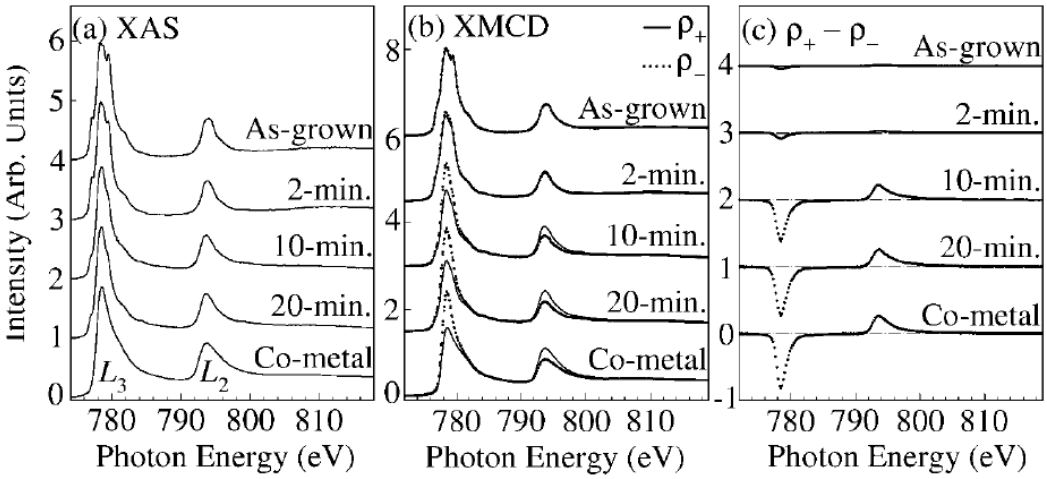

Figure 2.12 XMCD spectra of Co:TiO_2 for different post annealing times: 0 (as grown), 2, 10, and 20 min in comparison with those of Co metal. (a) Co $L_{2,3}$-edge XAS spectra (Co 10%) (b) Co $L_{2,3}$-edge XAS spectra recorded with right- and left circular polarization (Co 10%) (c) resulting difference spectra (MCD)

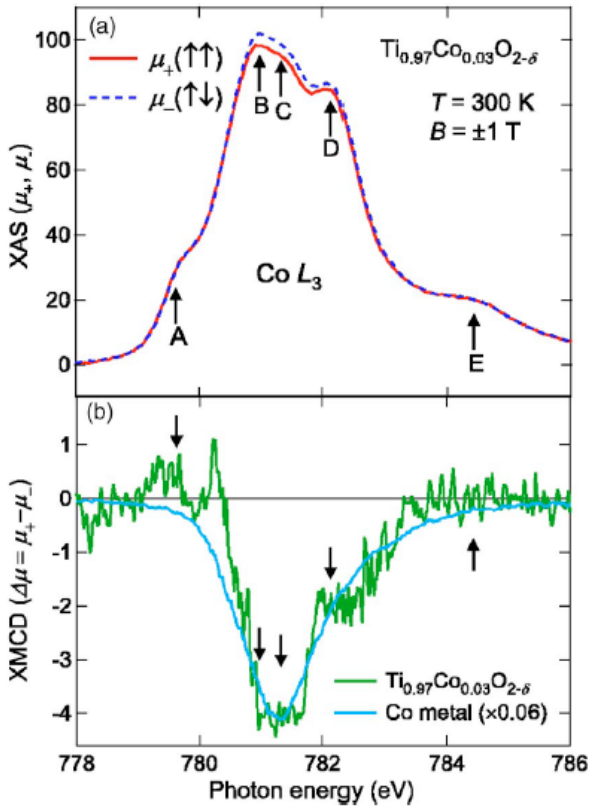

Figure 2.13 (a) Co L_3-edge region of a Co:TiO_2 thin film (3% Co), recorded with right- and left circular polarization. (b) Co L_3-edge XMCD, alleged multiplet features are denoted by arrows [51].

Shinde *et al.* suggested, however, that co-occurrence of superparamagnetic Co clusters and the AHE is possible in Co:TiO_2 films, indicating that observing an AHE is not a robust test for confirming carrier mediated ferromagnetism [49]. Kim *et al.* investigated the origin of ferromagnetism of anatase Co:TiO_2 with x-ray absorption spectroscopy (XAS) and x-ray magnetic circular dichroism (XMCD) [50]. XMCD is a useful probe since it reflects element specific contributions to magnetism. In Figure 2.12 (a), the ionic multiplet structure of the Co *L*-edge is smeared out gradually with increasing annealing time, and finally the spectral shape becomes identical to that of Co metal, suggesting that Co metal clusters are the cause for ferromagnetism. In Figure 2.12 (c), the weak MCD signal increases with the annealing time at 400^{o}C, indicating that most Co is segregated during the annealing process. In contrast, Mamiya *et al.* reported multiplet features in Co L-edge XMCD spectra in Figure 2.13, suggesting that Co^{2+} ions, and not metallic Co which is characterized by featureless spectra, contribute to magnetism [51].

2.5 The possibility of intrinsic dilute magnetic oxides

Many first-principle calculations were also proposed to explain the origin of room temperature magnetism in dilute magnetic oxides. However, the local spin density approximation (LSDA) is well known to overestimate the sp-d hybridization and the energy of the transition metal 3d level relative to the band edges, due to the underestimation of the band gap. Consequently, this approach leads to a lot of erroneous results in DMS studies [2, 10]. The impurity band model proposed by Coey *et al.* [10] may be a possible explanation for carrier mediated magnetism, but a recent calculation shows that oxygen vacancies in oxides induce deep levels, and cannot lead to long range ferromagnetic exchange interaction [52, 53].

A recent density functional calculation with band gap correction suggests that ferromagnetic Cr-Cr coupling in *n*-type In_2O_3 can be mediated by Sn doping [52]. Cr does not produce any carriers since the 3d levels of transition metals lie deep inside the gap in wide band gap oxides. However, the charge state of the transition metal can be controlled by changing the Fermi level through doping [52]. In Figure 2.14, the Cr state can be charged upon degenerate electron doping, and then undergoes a Jahn-Teller distortion (Cr^{-1}). If the charged state is partially occupied ($a^{0.5}$), there is an energy gain by splitting the highest occupied level into bonding and anti-bonding levels. If the charged state is fully occupied (a^{1}), there is no energy gain, and thus no ferromagnetic interaction. Therefore, in this model, the ferromagnetic interaction is mediated by the charge control of the 3d level through electron doping, rather than the *sp-d* exchange interaction.

For rutile Co:TiO_2, Quilty *et al.* suggested a strong hybridization between the conduction band and t_{2g}-states of a high spin Co^{2+} ion [54]. X-ray photoelectron spectroscopy (XPS) measurements showed that Co^{2+} is high spin state in which an unoccupied t_{2g} state is expected to hybridize with the Ti 3d t_{2g} derived conduction band, i.e. direct d-d hybridization, illustrated in Figure 2.15. The authors observed a shift of the conduction band, which may be expected due to its exchange splitting with increasing Co doping up to 10%.

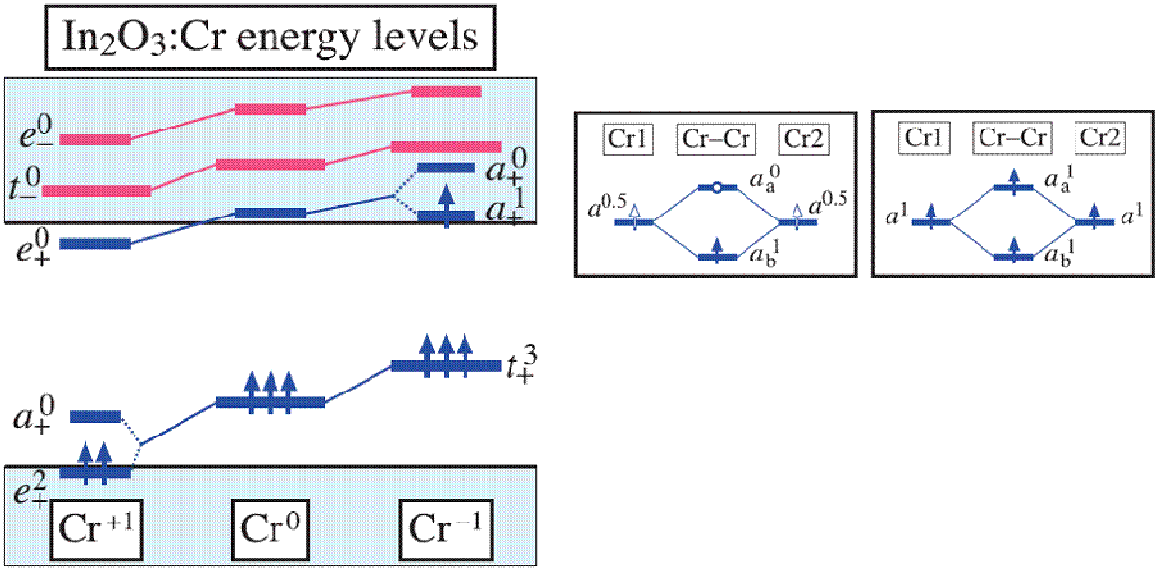

Figure 2.14 Electronic configuration of a single substitutional Cr atom in In_2O_3, for positively charged Cr^{+1}, charge neutral Cr^0, and negatively charged Cr^{-1} state. The shaded areas denote the valence and conduction bands [52].

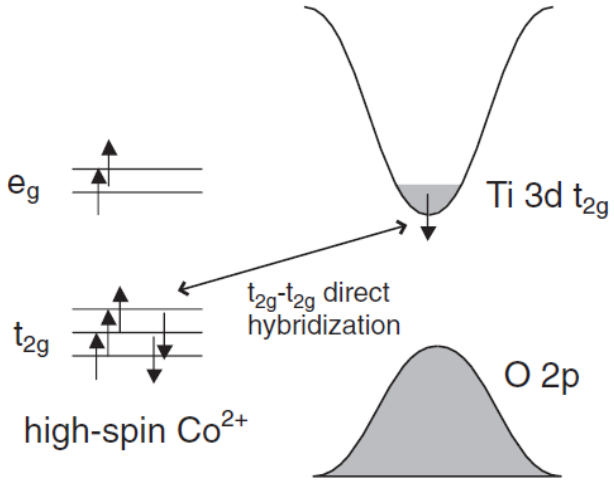

Figure 2.15 Schematic band diagram showing the high-spin Co^{2+} state and the resulting strong t_{2g}-t_{2g} coupling between the Ti 3d and Co 3d t_{2g} states [54].

For proving intrinsic DMS behavior, carrier mediated ferromagnetism such as tunable ferromagnetism and control of magnetization direction by electric fields should be demonstrated, along with the measurement of AHE. So far, these have not yet been demonstrated and the mystery of the origin of magnetism in dilute magnetic oxides still remains. If the reported room temperature dilute magnetic oxides are real DMS, they should show electric tunability of ferromagnetism, large tunnel magnetoresistance effects, strong magneto-optical effects, and the existence of a spin-split band of carriers [10].

References

[1] T. Dietl, and H. Ohno, Materials Today **9,** 18 (2006).

[2] T. Dietl, Semicond. Sci. Technol. **17,** 377 (2002); J. K. Furdyna, J. Appl. Phys **64,** R29 (1988).

[3] H. Ohno, Science **281,** 951 (1998).

[4] D. Ferrand, J. Cibert, A. Wasiela, C. Bourgognon, S. Tatarenko, G. Fishman, T. Andrearczyk, J. Jaroszynski, S. Kolesnik, T. Dietl, B. Barbara, and D. Dufeu, Phys. Rev. B **63,** 085201 (2001).

[5] A. Haury, A. Wasiela, A. Arnoult, J. Cibert, S. Tatarenko, T. Dietl, and Y. Merle d'Aubigné, Phys. Rev. Lett. **79**, 511 (1997).

[6] N. Samarth, Nature Mater. **6,** 403 (2007).

[7] S. Kuroda, N. Nishizawa, K. Takita, M. Mitome, Y. Bando, K. Osuch, and T. Dietl, Nature Mater. **6,** 440 (2007).

[8] T. Jungwirth, K. Wang, J. Masek, K. Edmonds, J. König, J. Sinova, M. Polini, N. Goncharuk, A. MacDonald, M. Sawicki, R. Campion, L. Zhao, C. Foxon, and B. Gallagher, Phys. Rev. B **72,** 165204 (2005).

[9] Dietl, H. Ohno, F. Matsukura, J. Cibert, and D. Ferrand, Science **287**, 1019 (2000).

[10] J. M. D. Coey, M. Venkatesan, and C. B. Fitzgerald, Nature Mater. **4**, 173 (2005).

[11] D. H. Kim, J. S. Yang, K. W. Lee, S. D. Bu, T. W. Noh, S.-J. Oh, Y.-W. Kim, J.-S. Chung, H. Tanaka, H. Y. Lee, and T. Kawai, Appl. Phys. Lett. **81**, 2421 (2002).

[12] A. Chambers, Surf. Sci. Rep. **61,** 345 (2006).

[13] Y. J. Lee, M. P. de Jong, and R. Jansen, Appl. Phys. Lett. **96,** 082506 (2010).

[14] G. Karczewski, *et al*., J. Supercond. **16**, 55 (2003).

[15] H. Saito, V. Zayets, S. Yamagata, and K. Ando, Phys. Rev. Lett. **90,** 207202 (2003).

[16] T. Story *et al*., Phys. Rev. Lett. **56,** 777 (1986).

[17] H. Ohno, H. Munekata, T. Penney, S. von Molnár, and L. L. Chang Phys. Rev. Lett. **68**, 2664 (1992).

[18] H. Ohno, A. Shen, F. Matsukura, A. Oiwa, A. Endo, S. Katsumoto, and Y. Iye, Appl. Phys. Lett. **69**, 363 (1996).

[19] S. Sonoda *et al*., J. Cryst.Growth **237**, 1358 (2002).

[20] S. E. Park, H.-J. Lee, Y. C. Cho, S.-Y. Jeong, C. R. Cho, and S. Cho, Appl. Phys. Lett **80**, 4187 (2002).

[21] N. Theodoropoulou, A. F. Hebard, M. E. Overberg, C. R. Abernathy, and S. J. Pearton, S. N. G. Chu, and R. G. Wilson, Phys. Rev. Lett. **89**, 107203 (2002).

[22] X. Chen, M. Na, M. Cheon, S. Wang, H. Luo, B. D. McCombe, X. Liu, Y. Sasaki, T. Wojtowicz, J. K. Furdyna, S. J. Potashnik, and P. Schiffer, Appl. Phys. Lett. **81**, 511 (2002).

[23] Y. D. Park, A. T. Hanbicki, S. C. Erwin, C. S. Hellberg, J. M. Sullivan, J. E. Mattson, T. F. Ambrose, A. Wilson, G. Spanos, and B. T. Jonker, Science **295**, 651 (2002).

[24] Y. Matsumoto, M. Murakami, T. Shono, T. Hasegawa, T. Fukumura, M. Kawasaki, P. Ahmet, T. Chikyow, S. Koshihara, and H. Koinuma, Science **291**, 854 (2001).

[25] P. Sharma, A. Gupta, K. V. Rao, F. J. Owens, R. Sharma, R. Ahuja, J. M. Osorio Guillen, B. Johansson, and G. A. Gehring, Nature Mater. **2**, 673 (2003).

[26] S. B. Ogale, R. J. Choudhary, J. P. Buban, S. E. Lofland, S. R. Shinde, S. N. Kale, V. N. Kulkarni, J. Higgins, C. Lanci, J. R. Simpson, N. D. Browning, S. Das Sarma, H. D. Drew, R. L. Greene, and T. Venkatesan, Phys. Rev. Lett. **91**, 077205 (2003).

[27] J. M. D. Coey, A. P. Douvalis, C. B. Fitzgerald, and M. Venkatesan, Appl. Phys. Lett. **84**, 1332 (2004).

[28] J. Philip, A. Punnoose, B. I. Kim, K. M. Reddy, S. Layne, J. O. Holmes, B. Satpati, P. R. LeClair, T. S. Santos, and J. S. Moodera, Nature Mater. **5**, 298 (2006).

[29] C. Zener, Phys. Rev. **81,** 440 (1950).

[30] A. H. MacDonald, R. Schiffer, and N. Samarth, Nature Mater. **4,** 195 (2005).

[31] J. Schliemann, J. König, H. Lin, and A. H. MacDonald, Appl. Phys. Lett. **78,** 1550 (2001).

[32] T. Jungwirth, J. Sinova, J. Masek, J. Kucera, and A. H. MacDonald, Rev. Mod. Phys.**78**, 809 (2006).

[33] A. Kaminski, and S. Das Sarma, Phys. Rev. Lett. **88,** 247202 (2002).

[34] M. Berciu, and R. N. Bhatt, Phys. Rev. Lett. **87,** 107203 (2001).

[35] G. M. Dalpian, and S. Wei, Phys. Rev. B **73,** 245204 (2006).

[36] J. M. D. Coey, Curr. Opin. Solid St. M. **10,** 83 (2006).

[37] J. M. D. Coey, Nature **430,** 630 (2004).

[38] K. N. Trohidou, X. Ziani, and J. A. Blackman, Phys. Status Solidi A **189,** 305 (2002).

[39] M. Yokoyama, H. Yamaguchi, T. Ogawa, and M. Tanaka, J. Appl. Phys. **97,** 10D317 (2005).

[40] D. W. Abraham, M. M. Frank, and S. Guha, Appl. Phys. Lett. **87,** 252502 (2005).

[41] R. Janisch, P. Gopal, and N. A. Spaldin, J. Phys. Condens. Matter **17,** R657 (2005).

[42] S.A. Chambers, C.M. Wang, S. Thevuthasan, T. Droubay, D.E. McCready, A.S. Lea, V. Shutthanandan, and C.F. Windisch Jr, Thin solid films **418,** 197 (2002).

[43] H. Toyosaki, T. Fukumura, Y. Yamada, K. Nakajima, T. Chikyow, T. Hasegawa, H. Koinuma, and M. Kawasaki, Nat. Mater. **3**, 221 (2004).

[44] K. Ueno, T. Fukumura, H. Toyosaki, M. Nakano, and M. Kawasaki, Appl. Phys. Lett. **90**, 072103 (2007).

[45] R. Ramaneti, J. C. Lodder, and R. Jansen, Appl. Phys. Lett. **91**, 012502 (2007).

[46] T. Yamasaki, T. Fukumura, Y. Yamada, M. Nakano, K. Ueno, T. Makino and M. Kawasaki, Appl. Phys. Lett. **94,** 102515 (2009).

[47] T. Fukumura, H. Toyosaki, and Y. Yamada, Semicond. Sci. Technol. **20,** S103 (2005).

[48] H. Toyosaki, T. Fukumura, Y. Yamada, and M. Kawasaki, Appl. Phys. Lett. **86**, 182503 (2005).

[49] S. R. Shinde, S. B. Ogale, J. S. Higgins, H. Zheng, A. J. Millis, V. N. Kulkarni, R. Ramesh, R. L. Greene, and T. Venkatesan, Phys. Rev. Lett. **92**, 166601 (2004).

[50] J.-Y. Kim, J.-H. Park, B.-G. Park, H.-J. Noh, S.-J. Noh, J. S. Yang, D.-H. Kim, S. D. Bu, T.-W. Noh, H.-J. Lin, H.-H. Hsieh, and C. T. Chen, Phys. Rev. Lett. **90**, 017401 (2003).

[51] K. Mamiya, T. Koide, A. Fujimori, H. Tokano, H. Manaka, A. Tanaka, H. Toyosaki, T. Fukumura, and M. Kawasaki, Appl. Phys. Lett. **89**, 062506 (2006).

[52] S. Lany, H. Raebiger, and A. Zunger, Phys Rev. B **77,** 241201(R) (2008).

[53] L. H. Ye, and A. J. Freeman, Phys Rev. B **73**, 081304(R) (2006)

[54] J. W. Quilty, A. Shibata, J. -Y. Son, K. Takubo, T. Mizokawa, H. Toyosaki, T. Fukumura, and M. Kawasaki, Phys. Rev. Lett. **96**, 027202 (2006).

Chapter 3

Experimental methods

In Chapter 3, the experimental methods employed in this thesis are introduced. First, substrate preparation and sample growth by pulsed laser deposition (PLD) are described. Then, structural characterization by x-ray diffraction (XRD), high resolution transmission electron microscopy (HRTEM), and energy filtered transmission electron microscopy (EF-TEM) are described. Finally, the principles of x-ray absorption spectroscopy (XAS) and x-ray magnetic circular dichroism (XMCD) are introduced.

3. 1 Deposition of epitaxial oxide films

All the samples investigated here by e.g. electrical transport, and spectroscopy measurements have been deposited by using a pulsed laser deposition (PLD) technique. PLD is a thin film deposition technique in which a high energy laser beam pulse is focused onto a target to ablate materials onto a substrate. It is illustrated in Figure 3.1. The process of material ablation depends on the properties of the laser (laser energy, and laser pulse intensity and width), target materials, as well as gas pressure in the chamber. In the process of ablation, the laser energy is first absorbed by the target material primarily by electronic excitations, and then converted to heat. Vaporized materials expand and form a luminous plasma plume extending from the surface of the target and condense on the substrate. In spite of the seemingly simple principle, the basic processes occurring during the transfer of material from a target to a substrate are not fully understood and are consequently the focus of research. The plasma plume may contain a large variety of different particles such as atoms, molecules, electrons, ions, clusters, and micron-sized particles.

PLD has many advantages over other deposition techniques. First, it allows material deposition in all kinds of environments because the energy source for ablation is located outside the chamber. For instance, an external energy source leads to an extremely clean process, e.g. without filaments as are employed in evaporation methods. Second, the use of a carousel, illustrated in Figure 3.1, enables the deposition of multilayer films without breaking vacuum when changing target materials. Third, it has the capability for stoichiometric transfer of compounds from target to substrate, while evaporation or sputtering using a single source/target typically yields thin films with different elemental composition as the target materials. Highly complex oxides, such as superconducting oxides, ferroelectric oxides, ferromagnetic oxides etc. can be deposited with exactly the same stoichiometric composition as the target materials by PLD. Furthermore, the deposition rate in the PLD technique is highly controllable. However, there is one big disadvantage compared to other methods. Since the plasma plume formed by the laser is forward directed, the thickness of the material collected on a substrate is not

homogeneous. The area covered by the deposited materials is also quite small, typically ~1cm^2, such that PLD is not appealing to industry.

There are many commercially available lasers which are used in PLD set-ups. Most commonly used lasers are excimer lasers and Nd:YAG (Neodymium doped Yttrium Aluminum Garnet) lasers. Here, a KrF excimer laser with a wavelength of 248nm is used, where KrF gas is excited to an excimer by an avalanche electric discharge.

.

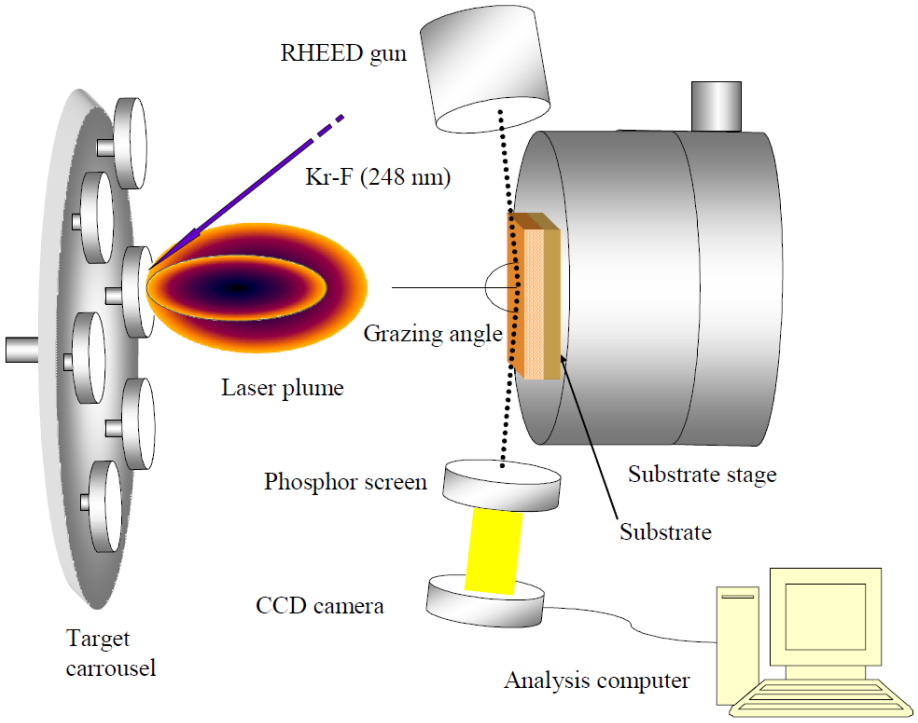

Figure 3.1 Schematic view of a typical pulsed laser deposition system [1]. The laser is focused on the target inside the vacuum chamber through a vacuum viewport using a lens, mask and mirrors (not shown). The reflection high energy electron diffraction (RHEED) system is used to monitor the thin film growth in real time.

Figure 3.2 shows the MASIF PLD system of the MESA$^+$ facilities. The excimer laser is aligned first on the target surface with several mirrors, a lens, and an additional guiding red laser. Since the laser beam has a Gaussian profile, a mask is placed in order to select a part of the beam where the spatial energy density variation is smallest, with the help of bum paper. The target is placed in the chamber in such a way that the laser beam impinges on its surface at 45 degrees with respect to the surface normal. The distance between mask and lens can be varied to obtain the desired growth parameters. The power and the repetition rate of the laser beam before entering the chamber can be measured over a series of pulses and controlled by an external controller. The laser beam enters the chamber through a vacuum viewport. The transmission of the viewport is monitored by calibration procedures, and kept optimal by regular polishing with cleaning powders. A

turbo molecular pump (TMP) is used to maintain a high vacuum in the chamber down to a pressure of 10^{-8}mbar. The layers used in this study are deposited at low pressure (10^{-1}mbar to 10^{-4}mbar) in an oxygen environment, except for metal layers which were deposited at high vacuum (10^{-8}mbar). The oxygen pressure inside the chamber is controlled by (1) a gas inlet with mass flow controller and (2) a variable valve between the chamber and the TMP. Inside the chamber, the targets and the sample can be mounted independently through a load lock. Before inserting targets into the chamber, they are grinded with sandpaper to achieve a smooth surface for ablation. Grinding the targets also helps to remove impurities and dust particles. Furthermore, the smooth surface helps to prohibit the ablation of big particles from the surface. There is a target carrousel to hold a maximum of 5 targets at a time. The target stage can be rotated to select a desired target for deposition.

A sample is first anchored on a sample holder using a non-magnetic conductive silver adhesive. The sample holder can be heated up to 850 ºC, as is required for the deposition of certain compounds. The temperature of the sample is monitored through a thermocouple, placed inside the sample heater just near the surface where the sample is anchored. Stepper motors can move targets and samples laterally and vertically in order to ensure that the laser hits the right position on the targets and the plasma flume hits the right position on a sample. A shutter is placed between the sample and the target such that before deposition, pre-ablation of the target is conducted in order to eliminate the deposition of surface contamination on the targets. Normally, single crystalline targets are preferred to deposit films of homogeneous composition and density. However, targets consisting of sintered pellets, with the highest possible density, can also be used for deposition. In our study, single crystalline targets of $SrTiO_3$(STO), and sintered pellet targets of LSMO and Co:TiO_2 have been used.

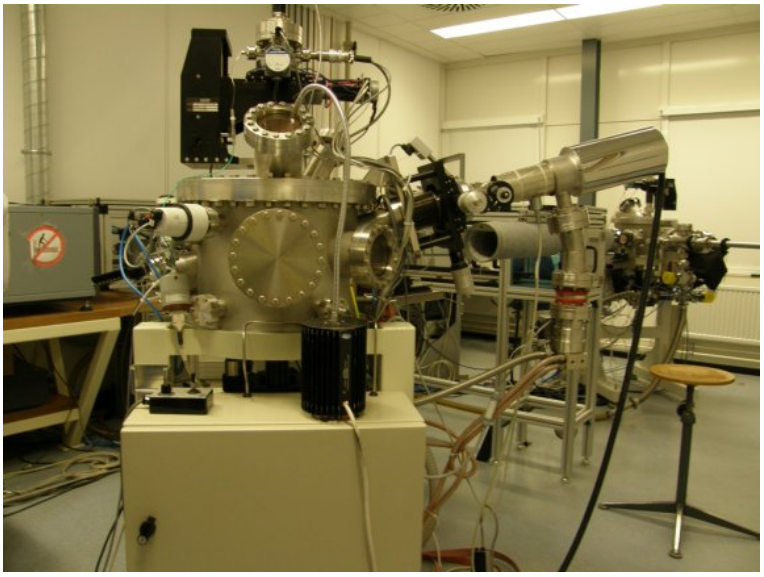

Figure 3.2 MASIF PLD system at MESA$^+$. A KrF eximer laser beam is guided to the chamber with several mirrors and a lens.

Single crystalline STO substrates are employed to deposit all anatase Co:TiO_2 films studied here, since the substrate treatment used to prepare the surface for epitaxial growth is well known, and STO enables the growth of TiO_2 in the anatase phase. The lattice of $SrTiO_3$ consists of two sub-lattices of SrO and TiO_2, layered alternately. STO substrates are obtained by cutting single crystals along a [100] plane and have a mixture of these sub-lattices on the surface [2]. To facilitate well controlled epitaxial growth on STO substrates, it is better to have a single surface termination with atomically flat terraces. The surfaces must also be free of contamination such as dust particles, carbon-dioxide molecules, water molecules *etc.*, which affect the growth of thin films. TiO_2 termination has been selected since it has been calculated and observed that TiO_2 termination has the lowest surface energy, resulting in the most stable surface. STO [100] substrates with small miscut angle (below 0.1^o) have well defined steps on the surface when only one type of termination has been achieved (see Figure 3.3).

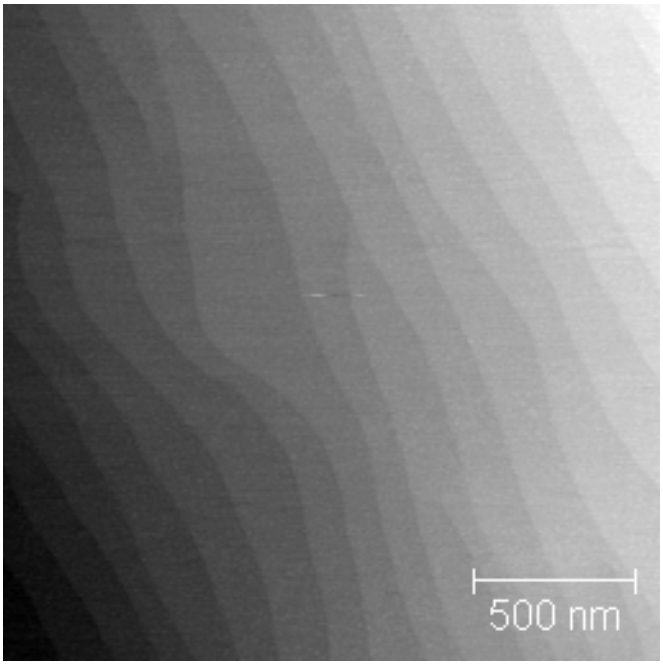

Figure 3.3 Atomic force microscopy image of a STO surface, after treatment according to reference [3].

A proper chemical and heat treatment is performed to achieve the TiO_2 surface termination of the substrate [3]. The treatment is performed as follows. To remove contamination from the surface, the substrate is first cleaned in acetone, followed by ethanol using an ultrasonic bath for 5 minutes each. The ultrasonic excitation helps removing contaminants from the surface. After that, the sample is checked for remaining contamination on the surface using an optical microscope. If necessary, the cleaning process is repeated until the contamination is removed. Then, the substrate is soaked in de-ionized (DI) water for 30 minutes in an ultrasonic bath to let SrO at the surface hydrolyze into $Sr(OH)_2$. Now, $Sr(OH)_2$ can be selectively etched away by dipping the

sample in Buffered hydrofluoric (BHF) acid for 30 seconds in an ultrasonic bath. BHF consists of NH_4F and HF acid in the ratio of 7:1 with a pH of 5.5. Then the substrate is cleaned in DI water and subsequently in ethanol to remove any remaining residues. This treatment yields a TiO_2 terminated substrate. The terrace steps are found to be rough. To obtain atomically smooth terrace steps the substrate is annealed at 950 ºC for 1 hour in an ambient of oxygen pressure of 1 bar. Annealing at these parameters causes the surface to relax by reducing the step edge density. Figure 3.3 shows an atomic force microscopy (AFM) image of a surface with terrace steps of a unit cell of TiO_2.

3.2 X-ray diffraction

When x-rays interact with materials, two processes may occur: x-rays are scattered or absorbed. The first process is related to elastic scattering which is used in diffraction measurements and the second process is related to a resonant process which will be described in section 3.4 [4]. The incident x-ray is an electromagnetic wave with its electric and magnetic field vectors changing sinusoidally with time and space. This electromagnetic wave exerts a force on electrons in atoms, causing them to vibrate with the same frequency of the x-ray. The re-oscillation of the electrons generates x-ray radiation in all directions again.

Diffraction is due to a constructive phase relation of scattered x-rays from matter. x-rays scattered from a periodic structure interfere constructively to form enhanced signals in certain directions, illustrated in Figure 3.4. If all the x-rays originating from the oscillating electrons are summed, the distribution function $f(Q)$ is simply the same as a Fourier transformation of the electron density $\rho(r)$, as given in equation 3.1:

$$f(Q) = \int \rho(r) e^{iQ \cdot r} dr , \qquad (3.1)$$

$$Q \cdot r = 2\pi N , \qquad (3.2)$$

$$2d \sin\theta = n\lambda , \qquad (3.3)$$

where Q is the momentum transfer, d is the plane-to-plane distance, λ is the wavelength of the X-ray, θ is the incident angle, and N and n are integers. The constructive condition applied to the Fourier transformation is known as the Laue condition, given in equation 3.2 (the momentum transfer should be a multiple of a reciprocal lattice vector), which is identical to the Bragg condition in equation 3.3 (the path difference should be a multiple of the x-ray wavelength). The latter is mostly used by material scientists to represent the conditions for constructive interference in a simple view. Therefore, the scattered electric field (or magnetic field) is the reciprocal space representation of electron density in terms of the wave. The magnetic field is usually neglected since its contribution is much smaller by a factor of approximately 10^{-4} than the electric field [5]. Magnetic scattering was not possible before the availability of high flux synchrotron x-ray radiation sources.

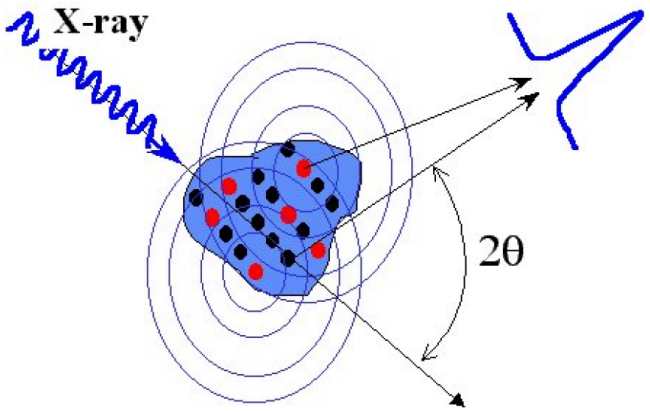

Figure 3.4 Schematic diagram of x-ray diffraction from matter [4].

The Bragg peak position is directly related to the atomic spacing, employed for the identification of compounds, or chemical phases. The peak width is related to the coherent volume of a scattering object, which is simply calculated from a Fourier transformation, and used in the calculation of the size of the object (e.g. the grainsize for polycrystalline samples). It is simply known as the Scherre formula, equation 3.4:

$$W(2\theta) = \frac{0.94\lambda}{L\cos\theta}, \qquad (3.4)$$

where $W(2\theta)$ is the full width half maximum of the Bragg peak, λ is the wave length of the x-ray, and L is the size of the object.

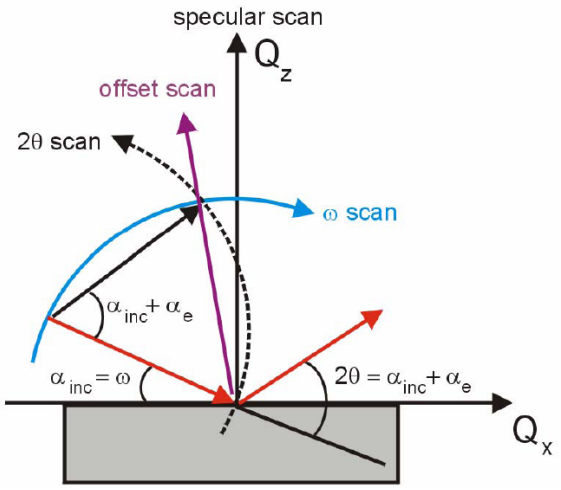

Figure 3.5 Schematic diagram of the x-ray diffraction geometry in reciprocal space [6]. α_{inc} is an incident angle to the sample or called as the Omega. α_e is the sum of θ and offset angle.

A so-called "theta-two theta" (θ - 2θ) measurement is measuring normal Bragg points, which is called a specular scan (Q_z), illustrated in Figure 3.5. When the sample is rotated such that the incident angle of the x-rays equals θ, the detector is positioned at an angle of 2θ in this measurement, simply satisfying the Bragg condition for crystal planes parallel to the sample surface. In case of thin films, or a certain phase in the film grown offset in angle with respect to a substrate, the offset should be corrected for since the Bragg points are offset in the reciprocal space. Therefore, an offset scan is a simple theta-two theta scan with a certain offset applied. This is illustrated in Figure 3.5. It is not easy to detect tiny clusters grown offset by a normal point-like detector such that a two dimensional detector is preferable to cover a large region of reciprocal space.

3.3 High resolution transmission electron microscopy

Transmission electron microscopy (TEM) is a technique in which an electron beam is transmitted through an ultra thin specimen, and then used for constructing an image with various contrast mechanisms based on its interaction with the matter. In contrast to optical microscopes, the high energy electron beam emitted from a filament is focused by electromagnetic lenses, whose focus is adjusted by controlling currents [7]. TEM is capable of imaging at a much higher resolution than optical microscopes, owing to the small *de Broglie* wavelength of high energy electrons. As illustrated in figure 3.6, the transmitted electrons interact with the matter both elastically and inelastically. Elastically transmitted electrons, including diffracted electrons, are used for imaging while characteristic x-rays or inelastically scattered electrons are used for chemical analysis.

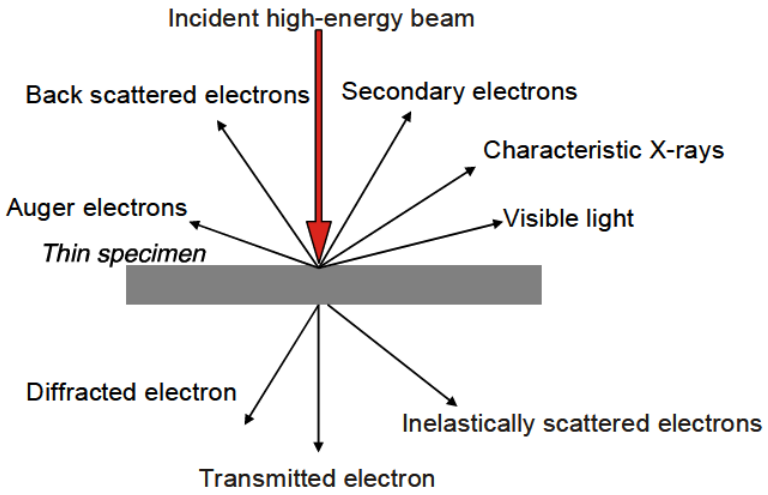

Figure 3.6 Schematic diagram of the interaction of high energy electrons with matter.

The contrast for TEM imaging arises from three mechanisms: mass or thickness dependent absorption (hereafter simply abbreviated as mass-thickness contrast), diffraction-, and phase contrast. In Figure 3.7, the imaging methods can be classified as bright field, dark field and phase contrast modes by employing the above contrast

mechanisms. In the bright field (BF) mode (Figure 3.7.a), an aperture is placed in the back focal plane of the objective lens to allow only the directly transmitted electrons to pass. In this case, the image contrast is realized by weakening the transmitted beam by its interaction with the matter. Therefore, mass-thickness and diffraction contrast are the main contribution to the image formation. For instance, thick areas, areas in which heavy atoms are more present, and crystalline areas in the specimen appear with dark contrast. In dark field (DF) images (Figure 3.7.b), the direct beam is not used while a diffracted beam is chosen for imaging. Since diffracted beams have strongly interacted with matter by satisfying the Bragg condition, very useful information can be obtained such as planar defects, stacking faults or particle size.

To obtain high resolution images, a large objective aperture is selected such that many beams including the direct beam are allowed to pass. The atomic lattice image is formed by the interference between the diffracted beams and the transmitted beams (phase contrast). Crystalline samples oriented along a zone axis are imaged in high-resolution TEM (HRTEM) with a suitable point resolution.

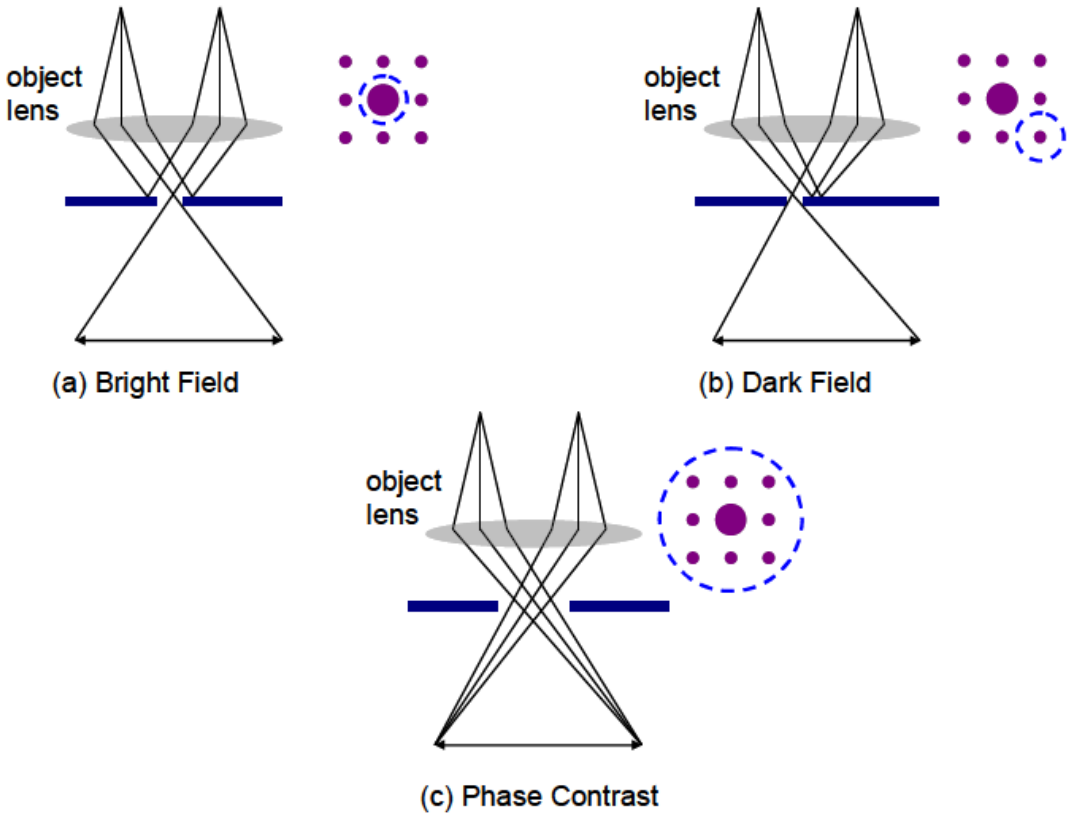

Figure 3.7 Three image modes of transmission electron microscopy: (a) bright field, (b) dark field, and (c) phase contrast.

3.4 Energy filtered transmission electron microscopy

Energy-filtered transmission electron microscopy (EFTEM) is the imaging technique based on electron energy-loss spectroscopy (EELS), in which the amount of energy loss by high-energy electrons is measured through an energy filter. The loss of energy is due to inelastic interactions with matter, and since core-level excitations are involved it is element specific. This element specific energy loss yields quantitative information about local chemical composition, and therefore the inelastically scattered electrons can be used to construct a two-dimensional elemental image. Figure 3.8 shows an EFTEM configuration with a parallel EELS system attached to the bottom of a TEM, [8].

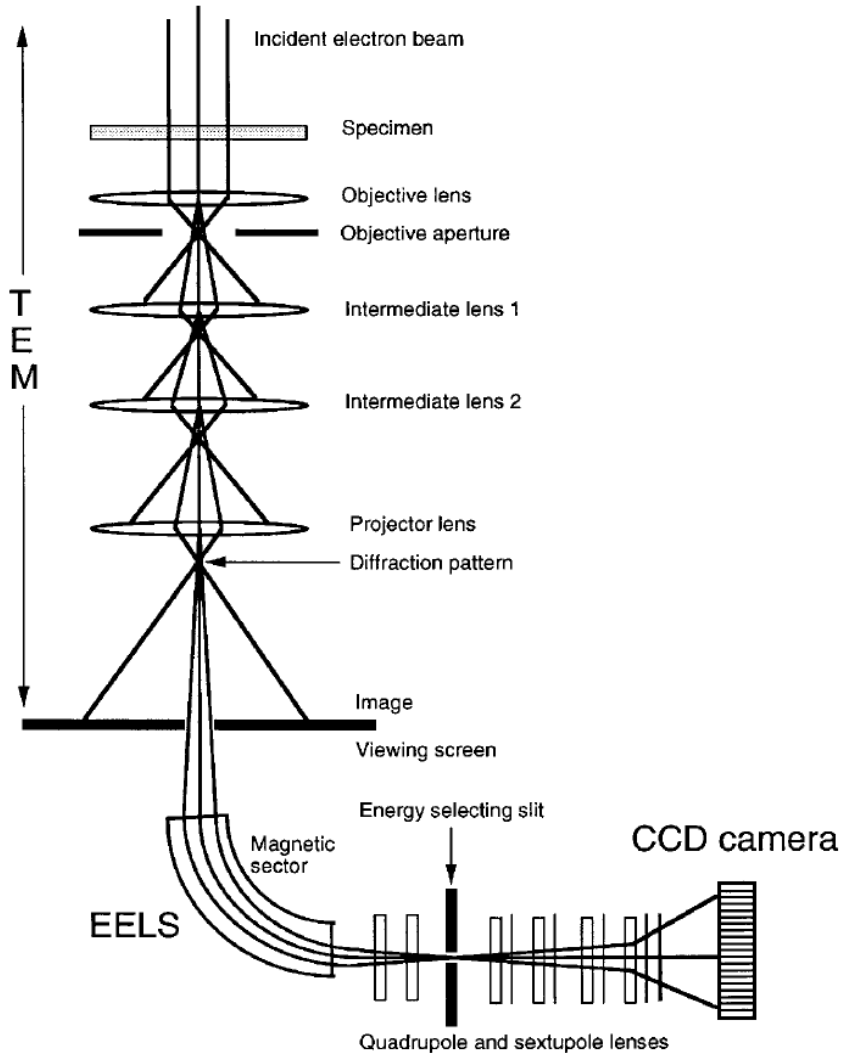

Figure 3.8 A schematic diagram showing the energy-filtering system attached to the High resolution TEM [8].

The EFTEM can be operated independent of the energy-filtering system, since the energy filtering is performed after the electrons are transmitted through all the lenses in the TEM. The transmitted electrons are then dispersed by magnetic sectors in the EELS detector, and electrons with different velocities (or energies) are focused on different positions in the plane of the energy-selecting slit. The electrons with a specific range of energy losses are selected by the slit. The above energy filter system can be attached to any existing TEM without any modification to the electron optics. Therefore, energy filtering of high-resolution TEM images can be conducted by using this method. However, the fact that only a limited portion of the transmitted electrons allows for energy-filtering limits this technique for high resolution imaging [8]. Alternatively, EFTEM can be carried out by using a scanning transmission electron microscope (STEM). However, in this case the spatial resolution and image acquisition time are governed by the number of points sampled by the beam as it scans across the specimen [9]. Therefore, the acquisition time for STEM EFTEM images with high spatial resolution is long, and therefore damage to the specimen may result. Figure 3.9 shows the EFTEM at MESA$^+$ used in this thesis.

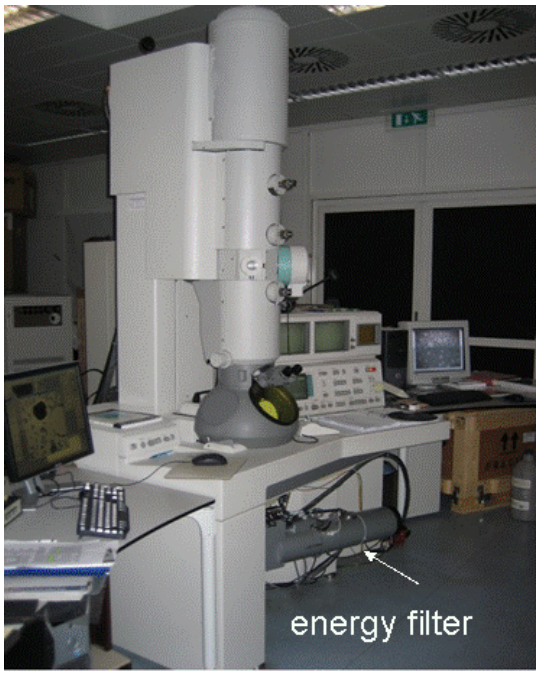

Figure 3.9 Transmission electron microscope equipped with GATAN energy filter at MESA$^+$.

As is depicted in Figure 3.6, a part of the kinetic energy of the incident electrons can be transferred to matter, and this energy loss produces x-rays, auger electrons, secondary electrons, phonons, plasmons, and cathodoluminescence. If the energy transfer of an incident electron is absorbed by an electron localized in inner shells, a core electron may be then excited to unoccupied states in the specimen, or ejected from the sample. The resulting electronic state is energetically unstable, such that another electron drops down from a higher level to fill the core hole, emitting for example a characteristic x-ray.

However, the excess energy released upon refilling the core hole can also eject loosely bound electrons. These electrons are called Auger electrons. Phonons are also generated by an up-take of energy from the electron beam. If incident electrons impinge onto atoms and transfer a small part of their energy, atoms begin to vibrate and phonons are formed. Plasmons can also be formed if the electrons pass through an assembly of "free" electrons. The transfer of energy may then induce collective oscillations inside the electron gas, i.e. plasmons. They can be formed in any material with free or weakly bound electrons and are the most frequently produced species by inelastic interactions between electrons in metals. In case of semiconductors, an electron beam bombardment produces visible light, called cathodoluminescnece, since the transfer of energy can excite valence electrons to the conduction band. This electron-hole pair disappears by recombination, emitting visible light. All inelastic interactions in matter described above can be used in electron energy loss spectroscopy.

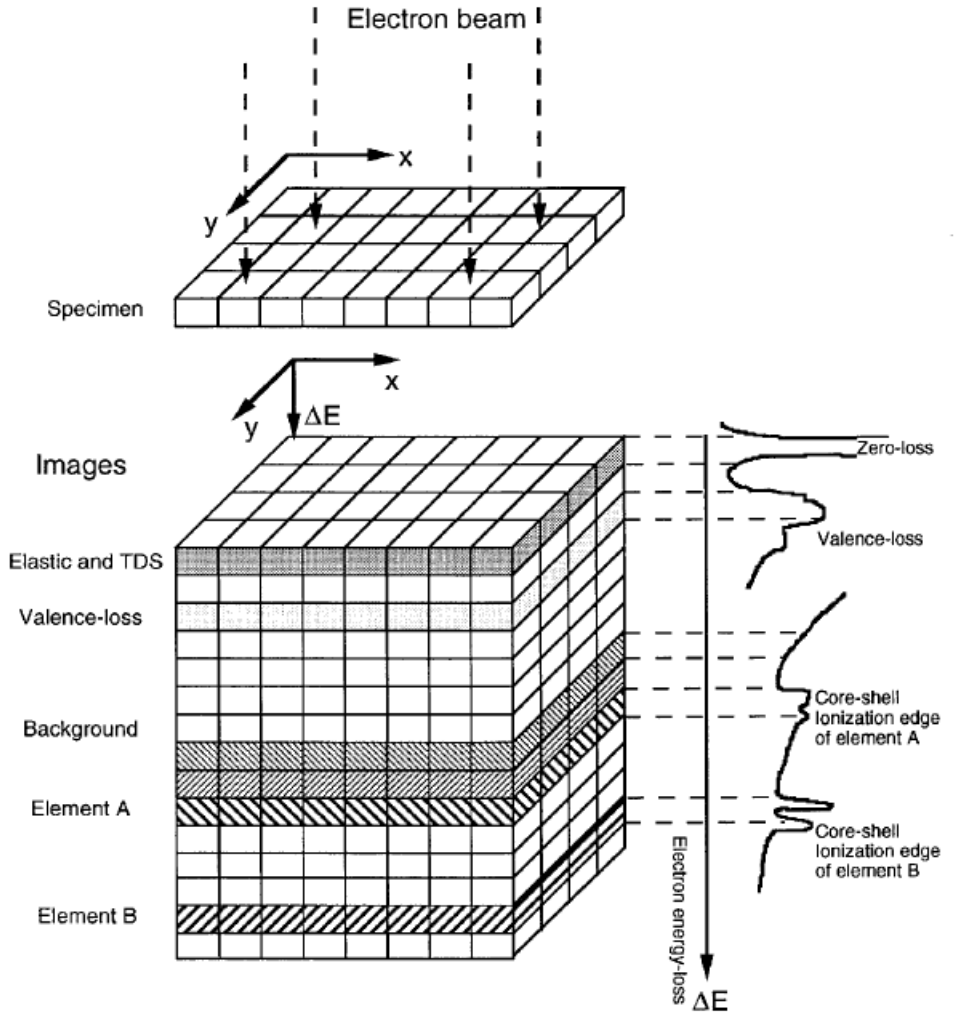

Figure 3.10 Schematic diagram showing energy-selected electron imaging in TEM. The energy-selected electron images corresponding to different characteristic energy loss features are shown [8].

The various energy loss features are schematically illustrated in Figure 3.10 [8]. A zero loss (ZL) peak appears at an energy loss of zero, without any inelastic interaction with matter. Valence losses include plasmon losses between the ZL peak and about 100eV. Above an energy loss of 100eV, the signal intensity drops rapidly. There are core shell ionization edges of elements in the EELS signal above the background. These ionization edges appear at energies which are element specific, and thus qualitative chemical analysis of a material is possible by EELS. The absorption edge corresponds to the energy which is necessary to promote an electron in an inner shell to the lowest unoccupied level. It also reflects spin-orbit coupling and fine structure due to the electronic transition. Measurements for specific elemental mapping are carried out by collecting signals at the corresponding ionization edge, and then subtracting a background signal extrapolated from measurements far below the edge.

3.5 X-ray absorption spectroscopy and X-ray magnetic circular dichroism

3.5.1 Synchrotron x-ray Sources

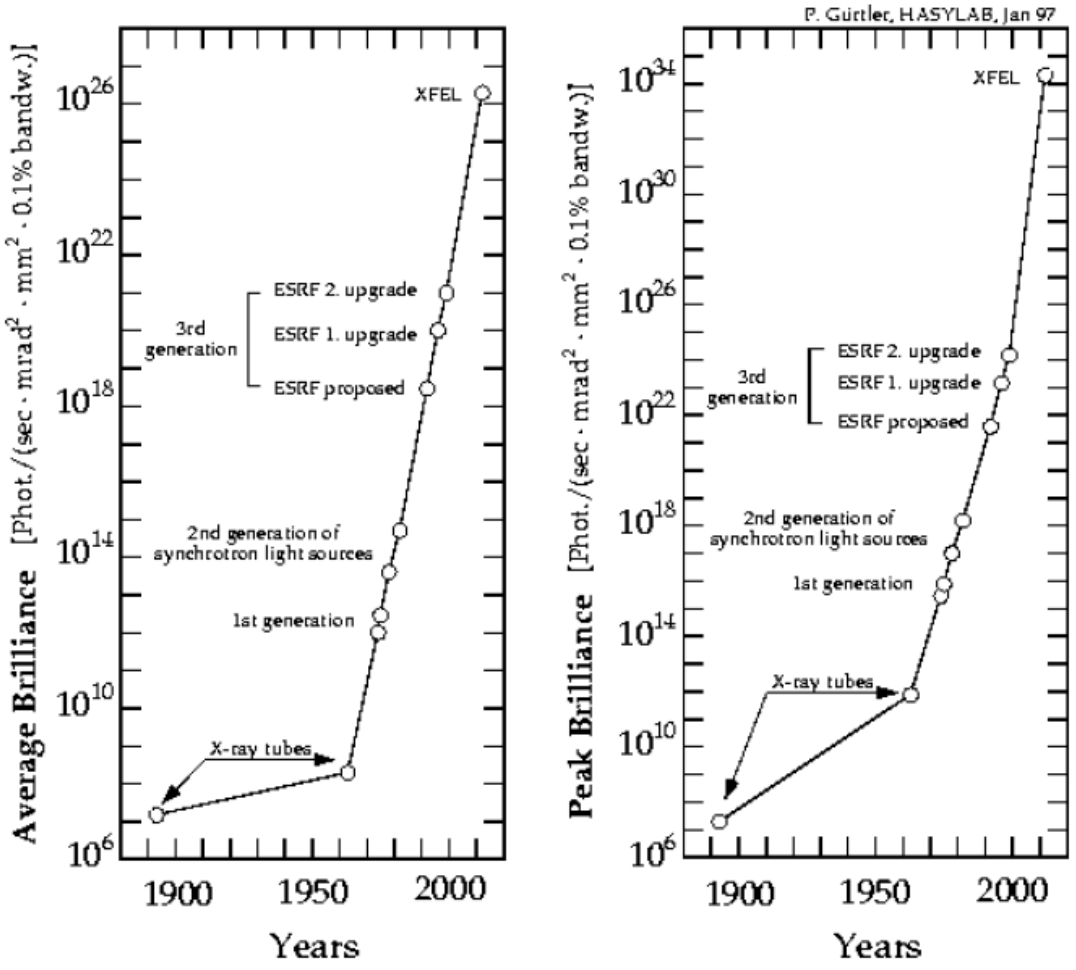

Figure 3.11 The average- and peak brilliance of x-ray sources as a function of time [10].

Normal laboratory x-ray sources are x-ray tubes or rotating anodes onto which electrons emitted from filaments impinge. The produced x-rays from theses sources have two contributions. The first contribution is known as *bremsstrahlung*, or "brake radiation", resulting from the phenomenon that high energy electrons are decelerated and finally stopped in the metal, giving rise to x-rays with a quasi continuous spectrum. The second contribution consists of characteristic x-rays arising from fluorescent emission between two atomic shells. Commercial x-ray diffractometers and spectrometers commonly use a single characteristic x-ray line, *e.g.* the K_α line, by filtering other continuous and characteristic x-ray emission contributions, such as the K_β line. However, x-rays generated from the above sources cannot be tuned continuously to the optimal wavelength for experiments. Furthermore, these x-rays are not polarized such that magnetic scattering cannot be carried out.

Synchrotron x-rays do not have these drawbacks. For 3rd generation synchrotron sources, the emitted radiation is approximately 10^{12} times brighter than that for in-house lab sources as can be seen in Figure 3.11 [5, 10]. Synchrotron radiation refers to a radiation from charged particles (*e.g.* electrons or positrons) travelling at relativistic speed under applied magnetic fields which curve their path. In a synchrotron facility, electrons travel in a closed "ring" (storage ring) in which electrons move linearly in straight sections, while their directions of motion are changed by several bending magnets, thus traveling in a closed orbit. For a 3rd generation synchrotron facility, insertion devices such as wigglers or undulators can be installed. Figure 3.12 shows a schematic of a typical beam line in a 3rd generation synchrotron facility. Alternating magnet lattices in the undulator force electrons to oscillate, thus producing light. The coherent superposition of light produced at each oscillation yields a high flux of light. The wavelength of the light used for experiments can be selected by a monochromator installed in the beamline.

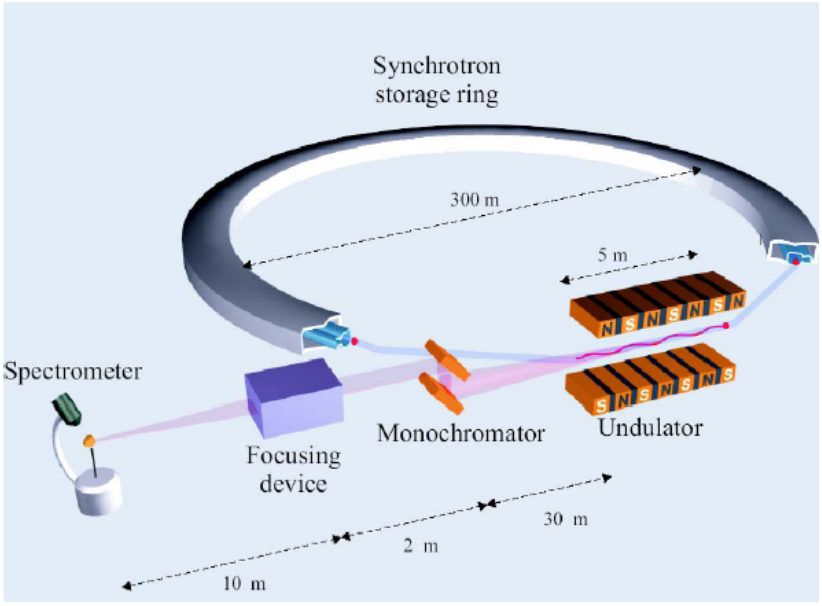

Figure 3.12 Schematic of a 3rd generation synchrotron beam line with undulator [5].

3.5.2 X-ray absorption spectroscopy

Photoelectronic absorption is a quantum mechanical phenomenon and can be described by time dependent perturbation theory. Upon interaction with an electromagnetic wave, the momentum of an electron should be expressed as the canonical momentum in equation 3.5, and then the Hamiltonian as given in equation 3.6 applies:

$$\vec{p} \to \vec{p} - e\vec{A}\,, \tag{3.5}$$

$$H = \frac{\vec{p}^{\,2}}{2m} + \frac{e}{m}\vec{A}\cdot\vec{p} + \frac{e^2\vec{A}^2}{2m}\,, \tag{3.6}$$

$$\vec{A} \sim \vec{\varepsilon}(a_k e^{ikr} + a_k^{+} e^{-ikr})\,, \tag{3.7}$$

where $\vec{A}$ is a vector potential of the photon field and $\vec{\varepsilon}$ is a polarization vector.
$\vec{A}$ is expressed linearly with annihilation (a_k) and creation operators (a_k^{+}) in terms of the quantization of the electromagnetic field in equation 3.7. Since the annihilation operator destroys the photon, the second term, $\vec{A}\cdot\vec{p}$ leads to absorption. The last term in equation 3.6 corresponds to Thomson scattering, i.e. elastic scattering. Therefore, the absorption process is calculated by the $\vec{A}\cdot\vec{p}$ matrix M_{if} in equation (3.8):

$$M_{if} = \left\langle f \middle| \frac{e}{m}\vec{A}\cdot\vec{p} \middle| i \right\rangle, \tag{3.8}$$

where *i* (*f*) represent the initial (final) states.
It is worth noting that the absorption is driven by the electric field of the electromagnetic wave, since the electric field is derived by a vector potential in free space ($\vec{E} = -\partial\vec{A}/\partial t$). The vector potential of the incident photon field ($\vec{A}$) contains plane waves in equation 3.7. Equation 3.8 can be formulated as equation 3.9 in the dipole approximation, in which the size of the absorbing atomic shell is taken to be small relative to the x-ray wavelength, such that the electric field inducing the electronic transition is constant over the atomic volume [11]. Since in the soft x-ray region (below 1000eV), the corresponding wavelength is above 1.2nm, and the 2p core shell radius of transition metals is on the order of 0.01nm, it is valid to use the dipole approximation for x-ray absorption at L-edges of transition metals [11].

$$\begin{aligned} M_{if} &= \left\langle f \middle| \vec{p}\cdot\vec{\varepsilon} e^{i\vec{k}\cdot\vec{r}} \middle| i \right\rangle \\ &= \left\langle f \middle| \vec{p}\cdot\vec{\varepsilon}(1 + \vec{k}\cdot\vec{r} + \cdots) \middle| i \right\rangle \\ &\cong \left\langle f \middle| \vec{p}\cdot\vec{\varepsilon} \middle| i \right\rangle \\ &= imw\left\langle f \middle| \vec{r}\cdot\vec{\varepsilon} \middle| i \right\rangle \end{aligned} \tag{3.9}$$

where w is the photon frequency associated with the transition, and m is electron mass [11].

The matrix in equation 3.9 was originally derived by Dirac, and called by Fermi "Golden Rule No. 2", but now it is often called by a misleading name, "Fermi's golden rule" [11]. The dipole operator in equation 3.9 includes the polarization vector ($\vec{\varepsilon}$) and position vector ($\vec{r}$). This means that the absorption depends on the orientation of the sample, whose physical properties are generally not isotropic. It also depends on the photon polarization, which can be manipulated by e.g. an undulator. The conditions for obtaining non-zero matrix elements are known as selection rules. For the dipole approximation and its associated selection rule, the orbital quantum number from initial to final state differs by 1 ($\Delta l = \pm 1$), and spin is conserved ($\Delta s = 0$).

In 1s x-ray absorption, the active electron approximation or single electron approximation is used. This approximation assumes that the absorption is a one electron process, and all other electrons are neglected in the excitation process [12]. In the final state, a core electron is excited to an unoccupied state and a hole is generated in a core level. Therefore, the final state in equation 3.9 can be rewritten as equation 3.10, which corresponds to the one electron approximation [13].

$$M \sim \left\langle f \left| \vec{r} \cdot \vec{\varepsilon} \right| i \right\rangle = \left\langle i\underline{c}e \left| \vec{r} \cdot \vec{\varepsilon} \right| i \right\rangle = \left\langle ie \left| \vec{r} \cdot \vec{\varepsilon} \right| c \right\rangle, \quad (3.10)$$

where e is an excited electron in an occupied state, $\underline{c}$ is a core hole, and c is a core electron.

In the case of 2p x-ray absorption (L-edge), the single electron approximation is not valid due to strong overlap of the core- and valence wave functions, such that other electrons participate in the transition. For L-edges, the matrix elements are expressed in equation 3.11:

$$M \sim \left\langle 2\underline{p}3d^{N+1} \left| \vec{r} \cdot \vec{\varepsilon} \right| 3d^{N} \right\rangle, \quad (3.11)$$

where $\underline{p}$ is a core hole in a p-orbital.

The final state of the x-ray absorption process for L-edges is affected by the core hole and thus shows multiplet effects. Coupling between the core hole and the electrons in the 3d orbital leads to many terms with different angular momenta and thus different energies, which are further split by the ligand field- and spin-orbit interactions. Figure 3.13 shows the calculation of fine structures in the L-edge for transitions from a $3d^8$ ground state to a $2p^5 3d^9$ final state. The evolution of the spectrum can be obtained by adjusting parameters such as Coulomb and exchange interactions, U (p,d) and 2p SO splitting [14]. In principle, XAS spectra render the basic information of an element's electronic states such as the valence state, high- or low spin state, and local coordination symmetry, which determine the matrix elements.

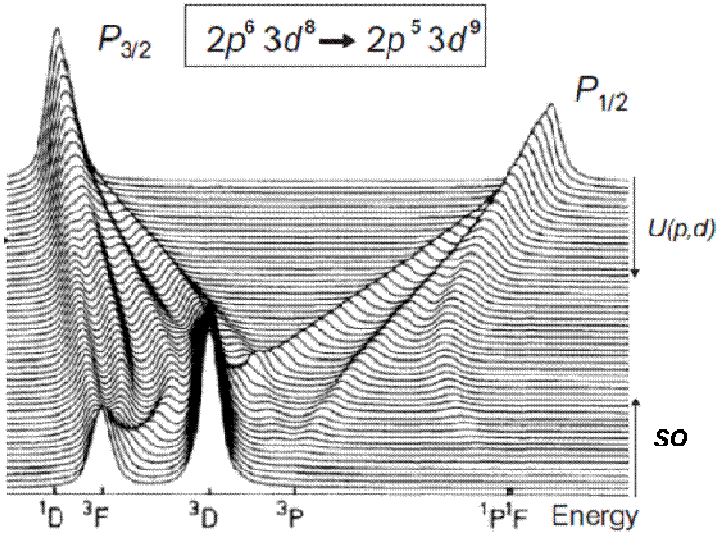

Figure 3.13 Calculated *L*-edge transition probability from a $2p^6 3d^8$ configuration with a ^3F ground state to the $2p^5\ 3d^9$ electronic final state configuration [14].

3.5.3 X-ray magnetic circular dichroism

In optics, optical properties of materials are explained by refractive indeces, as in equation 3.12 below. Dichroism refers to the dependence of the absorption part, $\beta(w)$ on the light polarization [11]. Since some materials absorb one color of white light preferentially depending on the crystal axis, such material appears to have two different colors for the two light directions. *Di* means two and *chroic* means colored. Today, the term dichroism is employed in scientific research for polarization-dependent photon absorption of a material. The origin of the dichroism effect can be anisotropies in the charge or the spin in the material. X-ray magnetic circular dichroism concerns the latter.

$$n(w) = 1 - \delta(w) + i\beta(w), \qquad (3.12)$$

where $n(w)$ is the refractive index, $\delta(w)$ is related to refraction, and $\beta(w)$ is related to absorption.

X-ray absorption is the process of x-ray induced electron excitation to empty levels, or to the vacuum. Ferromagnetic materials have a spin-unbalanced empty (and also filled) density of states (DOS). If the x-ray absorption process is spin dependent, the difference of the absorption intensity corresponds to the spin-imbalance of the empty DOS. This can be achieved by employing circularly polarized x-rays. Circularly polarized light has orbital angular momentum (light or left), which is also called the photon spin. XMCD is just the difference of two circularly polarized x-ray absorption spectra. For maximum XMCD signal, the direction of the magnetization of the sample and the photon spin are first chosen to be collinear. The dichroism signal is then obtained by taking the difference of two L-edge x-ray absorption intensities, which are measured for photons with positive

angular momentum and negative angular momentum parallel to the magnetization direction of the sample. The principle is illustrated in Figure 3.14 [11, 15]. Alternatively, the x-ray photon spin direction (circularity) is fixed and the magnetization directions are switched.

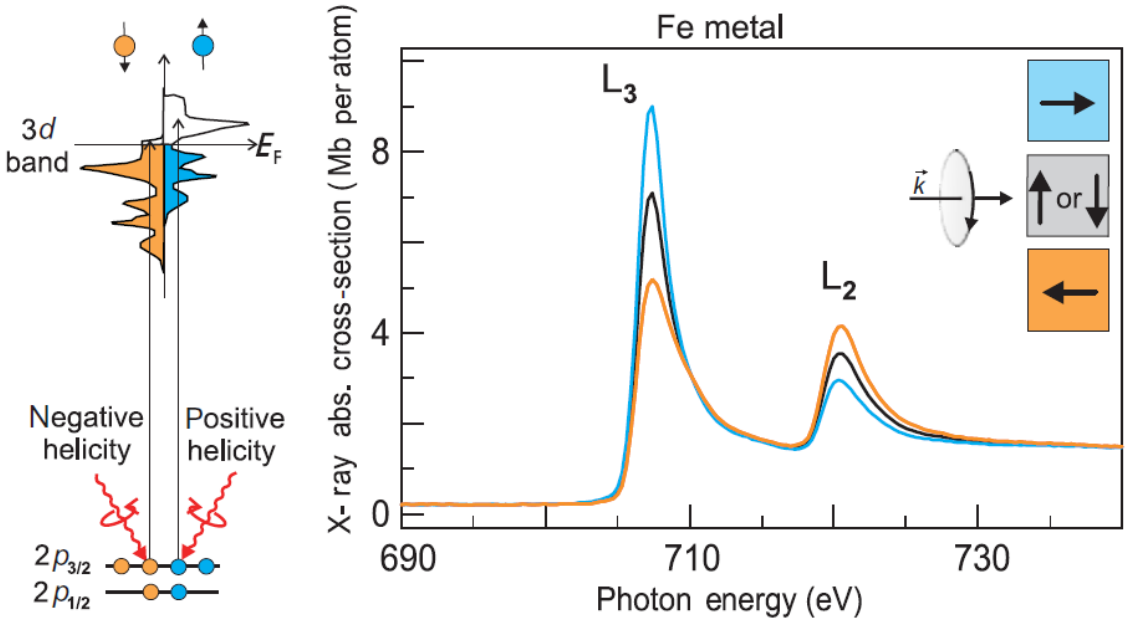

Figure 3.14 The XMCD effect illustrated for the L-edge absorption in Fe metal [15].

The origin of XMCD results from the conservation of angular momentum. A circularly polarized photon transfers its angular momentum to the excited photoelectrons. If the photoelectron is excited from a spin–orbit split level (L_3-L_2), the photoelectrons from each level L_3, and L_2 are spin polarized. Under SO interaction, spin is not a good quantum number, but the total angular momentum J is a good quantum number instead, such that spin-up and spin-down states are mixed, forming a basis for J. However, if the angular momentum of the photon is transferred to these SO-split states, the spin can be resolved. As is illustrated in Figure 3.15, the spin polarization of photoelectron is opposite for incident x-rays with positive and negative angular momentum quantum numbers. Furthermore the spin polarization of photoelectron is opposite at the two edges (L_3, L_2) since the $2p_{3/2}$ and $2p_{1/2}$ levels have opposite spin-orbit coupling (l+s, l–s).

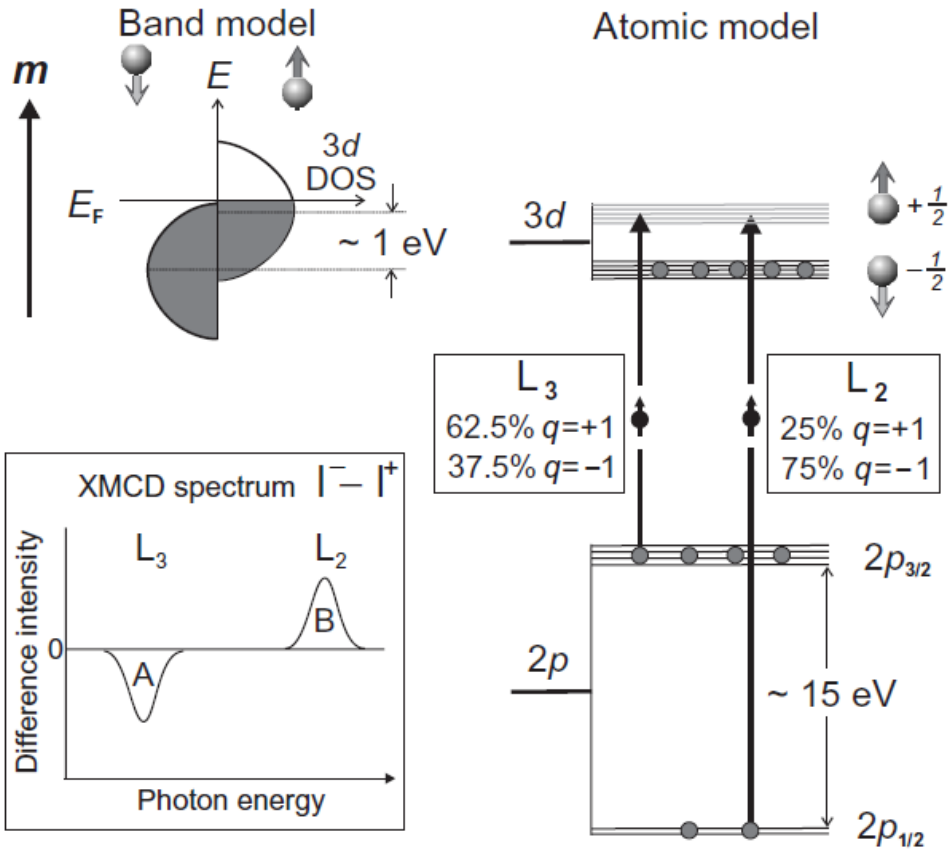

Figure 3.15 Illustration of the L-edge X-ray absorption processes of circularly polarized photons with angular momentum quantum number q = ±1(ħ).

From Figure 3.15, x-rays with positive spin (q = +1) at the L_3 edge excite 62.5% spin-up and 37.5% spin-down electrons, meaning 25% spin-up polarization, while x-rays with positive spin (q = +1) at the L_2 edge excite 25% spin-up and 75% spin-down electrons, meaning 50% spin-down polarization. Since the population of the $2p_{3/2}$ level is twice that of the $2p_{1/2}$ level, ΔI (A) = A at the L_3 edge and ΔI (B) =B at the L_2 edge are identical in magnitude, but opposite in sign. In reality, there is also an orbital angular momentum contribution for the photoelectron, and A and B are not identical.

3.5.4 XAS and XMCD measurements

All XAS and XMCD measurements were carried out at beam line I1011 of MAX-lab in Lund, Sweden. All spectra were measured in the total electron yield mode. Incident x-rays create core holes that are later filled, emitting Auger electrons. These Auger electrons go through inelastic scattering processes on their way to the surface, leading to a collision cascade. The emitted electrons are measured by a picoammeter and are (in most cases) simply proportional to the absorption signal. The measurement scheme is illustrated in Figure 3.16 [11]. Beam line I1011 is equipped with an Octupole magnet for

the generation of an arbitrary magnetic field direction. It consists of 8 magnets in which the current direction is controlled by MOSFET switching.

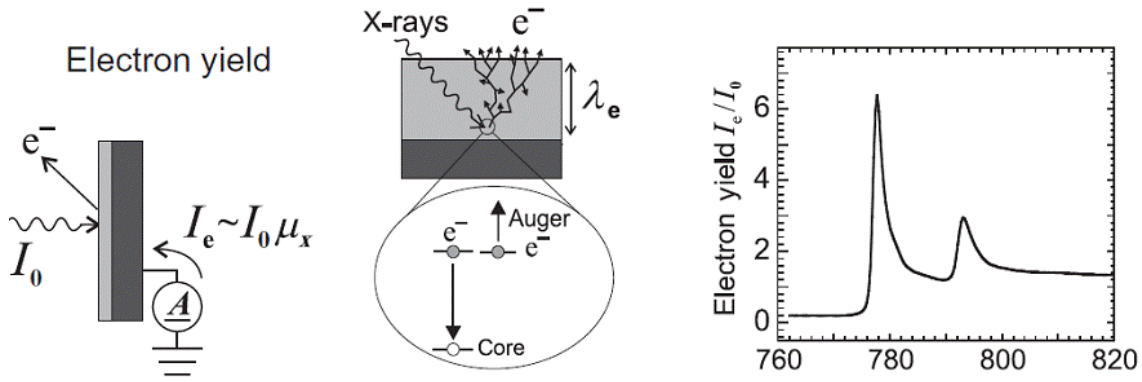

Figure 3.16 Illustration of the principle of recording X-ray absorption spectra by total electron yield detection [11].

References

[1] http://www.neocera.com

[2] F. M. Postma, *Epitaxial oxide spintronic structures (ferromagnets and semiconductors)*, PhD thesis University of Twente (2005).

[3] G. Koster, B. L. Kropman, G. J. H. Rijnders, D. H. A. Blank and H. Rogalla, Appl. Phys. Lett. **73**, 2920 (1998).

[4] X-ray scattering lecture note, D.Y. Noh from GIST

[5] J. Als-Nielsen, and D. McMorrow, *Elements of Modern X-ray physics*, John Wiley & Sons, Ltd. (2001)

[6] A. Ulyanenkow, Bruker AXS, *Introduction to high resolution X-ray diffraction*,

[7] D. Brandon, and W. D. Kaplan, *Microstructural characterization of materials*, John Wiley & Sons, Ltd. (1999)

[8] Z. L. Wang, D. van Heerden, D. Josell, and A. J. Shapiro, J. Res. Natl. Inst. Stand. Technol. **102**, 1 (1997).

[9] K. T. Moore, D. C. Elbert, and D. R. Verblen, American Mineralogist, **86,** 814 (2001).

[10] http://www-hasylab.desy.de

[11] J. Stöhr, H.C. Siegmann, *Magnetism*, Spinger (2006)

[12] F. M. F. de Groot, Chem. Rev. **101,** 1779 (2001).

[13] F. M. F. de Groot, Coordin. Chem. Rev. **249,** 31 (2005).

[14] G. van der Laan, and B.T. Thole, Phys. Rev. Lett. **60**, 1977 (1988).

[15] C. T. Chen, Y. U. Idzerda, H. J. Lin, N. V. Smith, G. Meigs, E. Chaban, G. H. Ho, E. Pellegrin, and F. Sette, Phys. Rev. Lett. **75**, 152 (1995).

Chapter 4

Magnetism and heterogeneity of Co in anatase $Co:TiO_2$ magnetic semiconductors

In this chapter 4, the origin of ferromagnetism in anatase $Co:TiO_2$ magnetic semiconductors with low Co concentration (1.4 at.%) is investigated using x-ray magnetic circular dichroism (XMCD) in combination with x-ray absorption spectroscopy (XAS) and energy-filtered transmission electron microscopy (EFTEM). The main focus is on Co-heterogeneity in relation to the magnetic properties of $Co:TiO_2$ thin films prepared under different conditions. XAS and XMCD spectra of the Co L-edges of $Co:TiO_2$ thin films are described, supplemented with measurements of structural properties using EFTEM. We will show heterogeneity of Co in the thin films, indicating an extrinsic origin of magnetism in $Co:TiO_2$.

4. 1 Introduction

The prediction of magnetism in wide band gap oxides and nitrides [1] has triggered much interest in room temperature dilute magnetic semiconductors (DMS) for practical spintronic devices. One of the most well-studied semiconductors is the Co doped TiO_2 for which room temperature ferromagnetism [2], the anomalous Hall effect (AHE) [3-6], magneto-optical dichroism [7,8] and transport studies [9-12] have been reported. However, there is still controversy about the origin of the observed ferromagnetism and related effects, i.e., whether the ferromagnetism is induced by a carrier-mediated exchange interaction between substitutional magnetic ions, or by defects or extrinsic sources (e.g. Co agglomerations) [4, 13-15].

In previous work, we observed ferromagnetism and the AHE at room temperature in anatase $Co:TiO_2$ thin films grown under oxygen poor conditions [6,11]. In Figure 4.1, vibrating sample magnetometry (VSM) measurements show that ferromagnetism develops under oxygen poor conditions, while the remanence and coercivity disappear for films grown under oxygen rich conditions (10^{-3} mbar). In Figure 4.2, AHE measurements of oxygen poor samples (7×10^{-5} mbar) with 550 nm thickness show that the shape of the AHE curve is consistent with the out-of-plane magnetization curve, including the remanence and coercivity values [6]. In the same material, conduction in a metallic impurity band was demonstrated [11]. These findings are, in principle, consistent with a mechanism of ferromagnetic exchange interaction between localized moments via this donor impurity band [16]. As Figure 4.3 shows, indications were also found in similar samples for Kondo-like behavior, which could be due to the resonant interaction of conduction electrons with local Co magnetic moments [11]. However, the strong coupling between carriers and a local moment in the Kondo regime causes screening and no long range ferromagnetic order [17]. For weaker coupling, ferromagnetic order can arise through a long-range interaction mediated by spin-polarized conduction electrons [17]. A combined observation of ferromagnetism and the Kondo effect in $Co:TiO_2$ therefore might indicate an inhomogeneous distribution of Co. This problem will be discussed in more detail in Chapter 5.

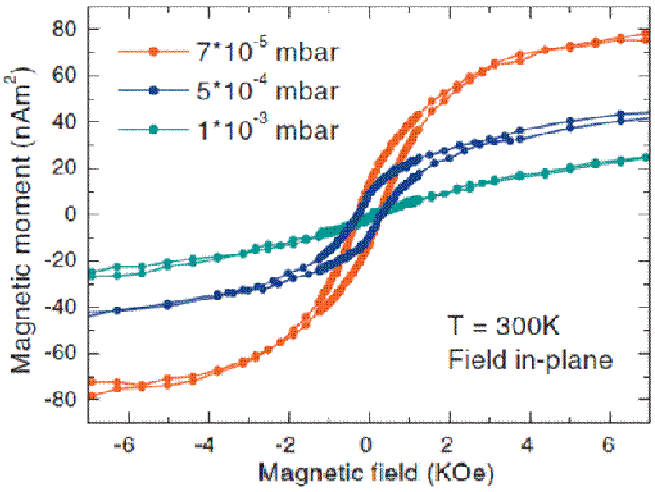

Figure 4.1 Magnetic moment versus magnetic field (applied in-plane) for Co:TiO_2 films grown at different oxygen pressure, as determined from VSM measurements [11].

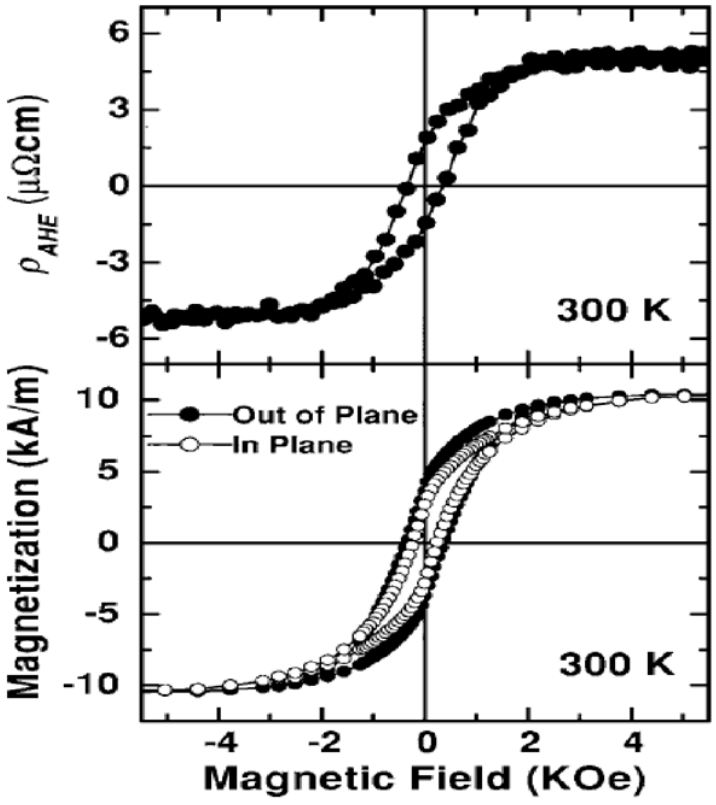

Figure 4.2 Top panel: Anomalous Hall resistivity ρ_{AHE} vs magnetic field (applied out of plane) for a 550nm Co:TiO_2 thin film. Bottom panel: Magnetization measured by VSM with the field applied in plane (open circles) and out of plane (solid circles) of the same sample [6].

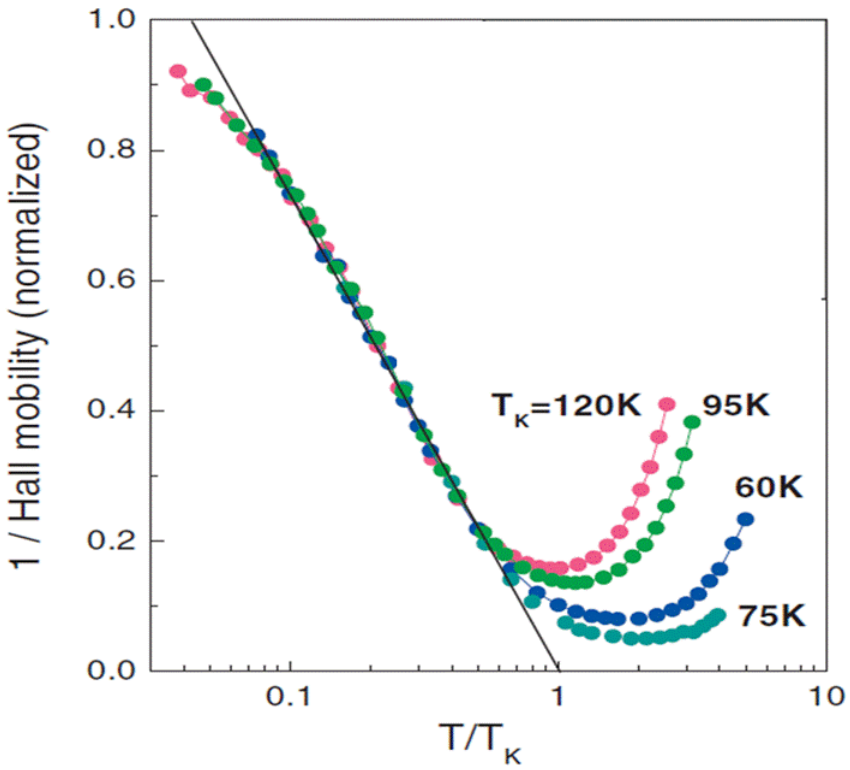

Figure 4.3 Kondo-like behavior in Co:TiO_2, shown as the inverse of the Hall mobility versus temperature normalized to the extrapolated Kondo temperature T_K. The vertical scale is normalized to have a value of 0.5 at T/T_K=0.2 for each curve. All films are grown at 9×10^{-5} mbar [11].

To investigate this conjecture, we present a combined soft x-ray absorption spectroscopy (XAS), x-ray magnetic circular dichroism (XMCD) and EF-TEM study of anatase TiO_2 with a low Co concentration of 1.4 at.%.

XAS and XMCD rely on the excitation of core-level electrons by soft x-rays, and thus provide element specific information on the electronic and magnetic properties of materials. Here, Co $L_{2,3}$-edge XAS and XMCD are employed to investigate i) the chemical bonding environment of the Co dopants, and ii) the Co-derived magnetic moments in Co:TiO_2. Co $L_{2,3}$-edge spectra mainly arise from electric dipole transitions between 2*p* core levels and empty 3*d* valence states, while additional contributions of $2p\rightarrow 4s$ transitions are negligible. Since the Coulomb-interaction between the 2*p* core holes and the 3*d* valence electrons is strong, the core-excited states remain largely localized on the Co ions. Consequently, the $L_{2,3}$-edge XAS (and XMCD) spectra of Co (and other transition metals) in a large variety of compounds can be interpreted in terms of *atomic* multiplet structure, which provides a "finger print" for Co ions in different charge states and local crystal fields. However, in the case of Co-metal, *d*-state hybridization quenches the orbital moment and strong delocalization of electronic states renders XAS spectra featureless [18]. This effect is illustrated in Figure 4.4 (reproduced from ref [18]), which shows XMCD spectra of Co clusters with increasing size obtained by depositing Co with sub-monolayer coverage on K substrates. It is clear that the atomic-like multiplet structure (e.g. the shoulder at 781 eV) in the XMCD spectra

becomes broadened and eventually resembles the featureless spectrum of bulk Co-metal as the Co cluster size grows. Also note the sign-reversal of the XMCD signal at the Co L_2-edge with increasing cluster size. Both the transition to a featureless spectrum and the sign-change at the L_2-edge are related to the increased amount of electronic delocalization in larger clusters. The above described effects allow distinction of different chemical Co-species based on their characteristic multiplets (or lack thereof), which in turn provides detailed information on the possible relation between Co-heterogeneity and magnetic behavior. EFTEM analysis is employed to corroborate the XAS/XMCD measurements via elemental (in particular Co) mapping.

We examine films grown under oxygen rich (10^{-3} mbar) and oxygen poor (9×10^{-5} mbar) conditions (hereafter referred to simply as "oxygen rich" and "oxygen poor" samples) having different magnetic properties at room temperature, i.e., paramagnetic and ferromagnetic, respectively (see Figure 4.1). Furthermore, we investigated the dependence of Co heterogeneity in oxygen poor samples on film thickness.

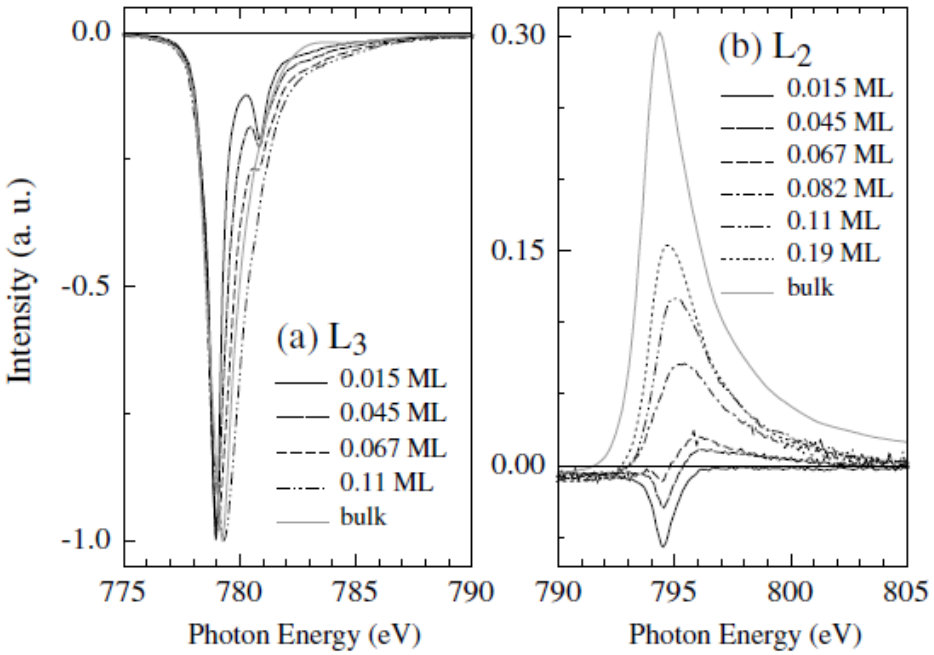

Figure 4.4 XMCD spectra recorded for Co on K showing pronounced line shape changes as the atomic Co forms clusters with increased coverage. [18].

4.2 Experimental details

Epitaxial thin films of anatase Co:TiO_2 (1.4 at.%) were grown by pulsed laser deposition on TiO_2-terminated (100) $SrTiO_3$ substrates under oxygen rich (10^{-3} mbar) and oxygen poor (9×10^{-5}mbar) conditions. $SrTiO_3$ substrates were chemically treated and annealed at 950°C to obtain a TiO_2 termination. Ablation of a $Co_xTi_{1-x}O_2$ (x=0.014) target was carried out using a KrF excimer (λ=248 nm) laser with a fluence of 1.8 J /cm^{2}at a rate of 5 Hz. The substrate temperature during growth of the films was fixed at 550 °C. In

particular, a series of oxygen poor samples (2nm, 10nm, 40nm, 180nm) was grown to investigate Co heterogeneity in thin films.

For comparison, a 2 nm thick reference Co metal thin film was fabricated using e-beam deposition with a capping layer of 3 nm thick Al. The XAS and XMCD Co $L_{2,3}$ edge measurements were performed at beam line I1011 of MAX-lab in Lund, Sweden, which uses an elliptically polarizing undulator, providing linearly and circularly polarized radiation. For XMCD experiments, the undulator settings were chosen such that the degree of circular polarization was 60% (one should consider a trade-off between obtaining a higher degree of circular polarization and a loss of photon flux). All spectra were measured at room temperature in total electron yield mode, (by measuring the drain current from the sample), with a probing depth of about 10 nm [19]. The XMCD spectra were obtained at a fixed photon helicity and an angle of incidence of 45^o with respect to the sample normal. To reverse the sample magnetization, an in-situ magnetic field was applied colinear with the x-ray beam (for Co:TiO_2 samples) or in the film plane (Co metal reference sample. Applying the field along the x-ray beam (parallel to the photon k-vector) ensures that the maximum XMCD contrast is obtained, provided that the sample can be magnetized along that direction. Since Co:TiO_2 thin films do not show any magnetic anisotropy, the collinear geometry is preferred (magnetization at 45^o with respect to the sample normal). The Co metal thin film shows strong in-plane anisotropy, however, such that it is required to keep the magnetization in-plane.

4.3 XAS and XMCD study of Co-heterogeneity in relation to magnetism

First, we show the results of AFM measurements that were performed to determine the surface morphology. In Figure 4.5, AFM images of a 45nm thick oxygen rich sample, and 45nm and 160nm thick oxygen poor samples are shown. The oxygen rich sample has a relatively smooth surface, with 1.4nm RMS (root mean square) roughness, compared to the oxygen poor sample with the same thickness (45 nm), which exhibits 4.5nm RMS roughness. As the film thickness is increased, the roughness increases as well. In particular, the 160nm thick oxygen poor sample features significant outgrowths (about 90nm in height), which are repeatedly observed on the surface. It is well reported that rutile outgrowths may form on anatase TiO_2 thin films, due to the thermodynamic meta-stability of the anatase phase in TiO_2 polymorphs [15]. The nucleation sites for rutile crystallites are defects such as dislocations or grain boundaries. The outgrowths on the surfaces of our samples are therefore expected to consist of rutile, which is indeed confirmed by Ti *L* edge XAS spectra, shown in Figure 4.6.

Representative Ti *L*-edges XAS spectra are shown in Figure 4.6, measured for oxygen poor films (9×10^{-5} mbar) with 10nm[1] and 160nm thickness. For the 160nm thick film, an enhanced shoulder at hν=461 eV is observed. As is well known from the literature on Ti *L*-edge XAS, this shoulder is indicative of the presence of a rutile phase. The different Ti *L*-edges of purely rutile and anatase TiO_2 are shown in Figure 4.7 (reproduced from Ref. 20). The presence of a parasitic rutile phase is also confirmed by high-resolution transmission electron microscopy (HRTEM) measurements, shown in section 4.4.

[1] 40nm thick oxygen rich- and 2, 10, and 40nm thick oxygen poor samples show essentially the same spectral shape

The main features of the Ti *L*-edge spectra can be described well by a dipole transition matrix calculation from a ground state $3d^0$ to a final state $2p^5 3d^1$. The case of Ti^{4+} is exceptionally simple, since the ground state is characterized by an empty 3*d* orbital, with term symbol $^1S_0$. The final state $2p^5 3d^1$ yields twelve different combinations of the orbital (*L*), spin (*S*) and total (*J*) angular momenta (twelve different term symbols), with different energies determined by the 2*p* (core hole) spin-orbit coupling, the 2*p*3*d* Slater-Condon parameters, and the 3*d* spin-orbit coupling. The dipole selection rule reduces the number of accessible final states to only three, resulting in three peaks for the Ti *L*-edge. When interactions with the six oxygen ligands are taken into account, the symmetry of the electronic states on the Ti^{4+} ion changes from spherical symmetry (SO_3) to cubic symmetry. Consequently, the three peaks are further split by the crystal field, into a total number of seven for octahedral symmetry (O_h). Atomic multiplet calculations for Ti^{4+} in octahedral crystal fields indeed give a good description of the experimental *L*-edge spectra [20].

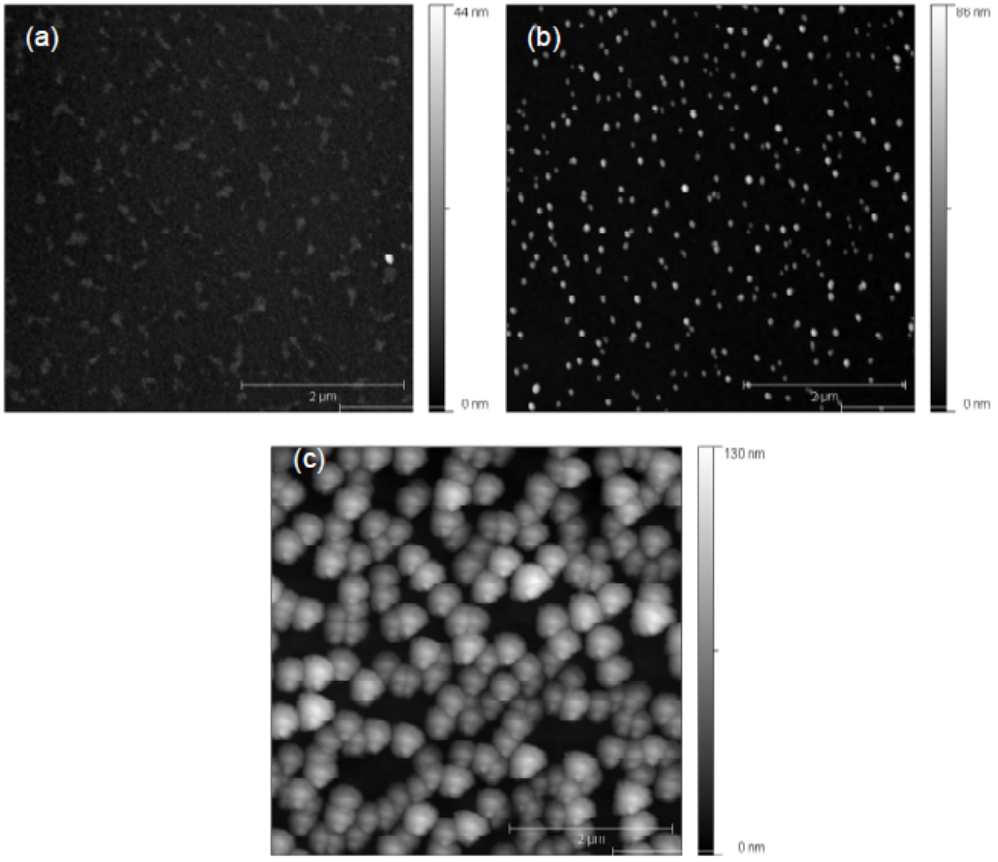

Figure 4.5 AFM images of a 45nm thick oxygen rich sample (grown at 10^{-3} mbar oxygen) with 1.4nm RMS roughness (a), a 45nm thick oxygen poor sample (grown at 9×10^{-5} mbar oxygen) with 4.5nm RMS roughness (b), and 160nm thick oxygen poor sample (grown at 9×10^{-5} mbar oxygen) with 25.5nm RMS roughness

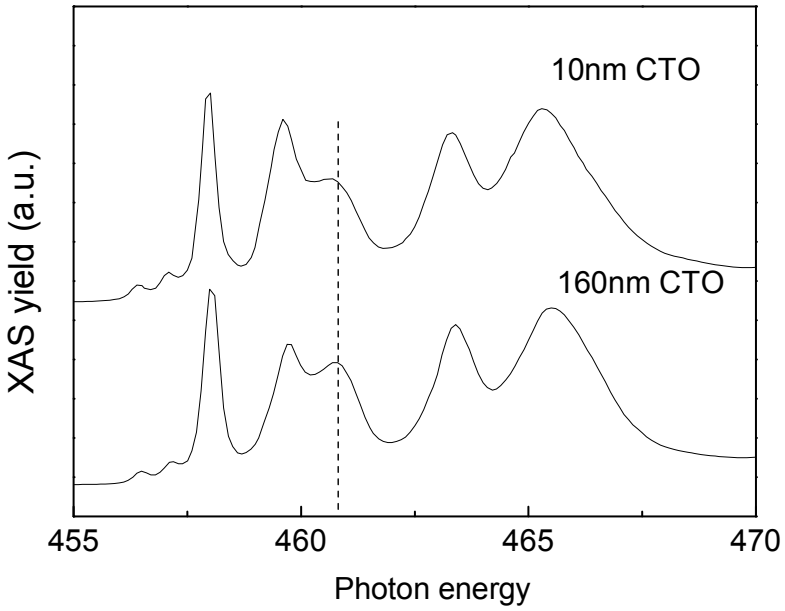

Figure 4.6 Ti *L*-edges XAS spectra for oxygen poor films (9×10^{-5} mbar) with 10nm and 160nm.

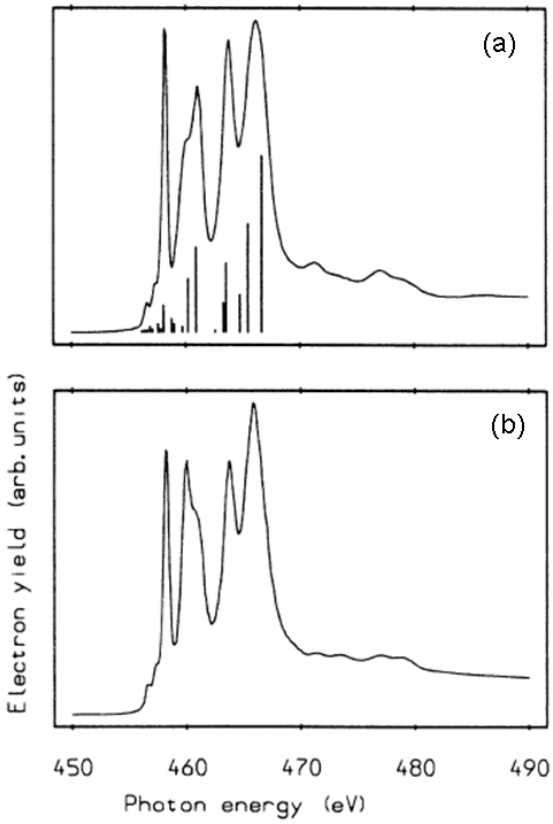

Figure 4.7 Ti *L*-edge of (a) rutile and (b) anatase TiO_2 [20].

Figure 4.8 shows the measured Co L_3 edge XAS spectrum of a 45nm thick oxygen rich- and 10nm thick oxygen poor sample, plus a calculated spectrum for Co^{2+} ions in an octahedral crystal field, obtained by ligand field multiplet (LFM) calculations as developed by Thole and co-workers, based on Cowan's atomic multiplet code and Butler's group theoretical code [21]. Interestingly, the multiplets are suppressed for oxygen poor films of 10nm. It should be noted that the spectrum with suppressed multiplet-related fine structure is quite similar to previously reported Co $L_{2,3}$ edge XAS data of rutile Co:TiO_2 thin films [22]. This issue will be addressed in detail below, following a general description of the Co L-edge spectral features based on LFM calculations.

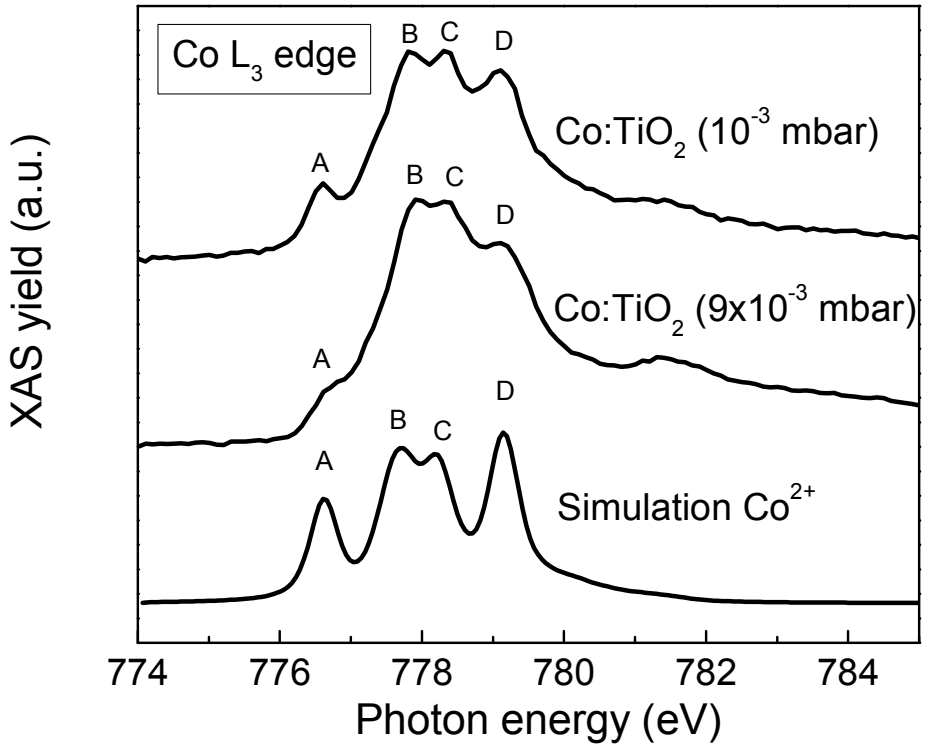

Figure 4.8 Experimental XAS data of a 45nm Co:TiO_2 thin films grown at 10^{-3} mbar oxygen (top), and 10nm grown at 9×10^{-5} mbar oxygen (middle), plus a simulation spectrum of $Co2^{+}$ (bottom) obtained by a LFM calculation.

The LFM calculation was performed for Co^{2+} ions (electronic configuration $3d^7$) in a cubic crystal field (O_h symmetry) with $10D_q$ = 1.1 eV, corresponding to a high-spin state. In LFM calculations, the interaction with the neighboring oxygen atoms is taken into account in a simple way by lowering of the ground state symmetry and the introduction of a crystal field. For cubic fields, an expression in terms of the parameters D_q, D_s, and D_t is traditionally used, where $10D_q$ corresponds to the splitting between the t_{2g} and e_g states. If $10D_q$ becomes large compared to the on-site exchange integral J, a transition from a high-spin to low-spin state results. In addition to crystal field effects, weak hybridization

effects can be "modeled" by tuning the reduction factor, κ, of the Hartree-Fock Slater integrals to account for the expansion of the 3*d*-derived wave functions in case of increasing covalence of the bonds (the so-called nephelauxetic effect). In the present case, the Slater integrals were scaled to 75% of their atomic values to account for these delocalization effects.

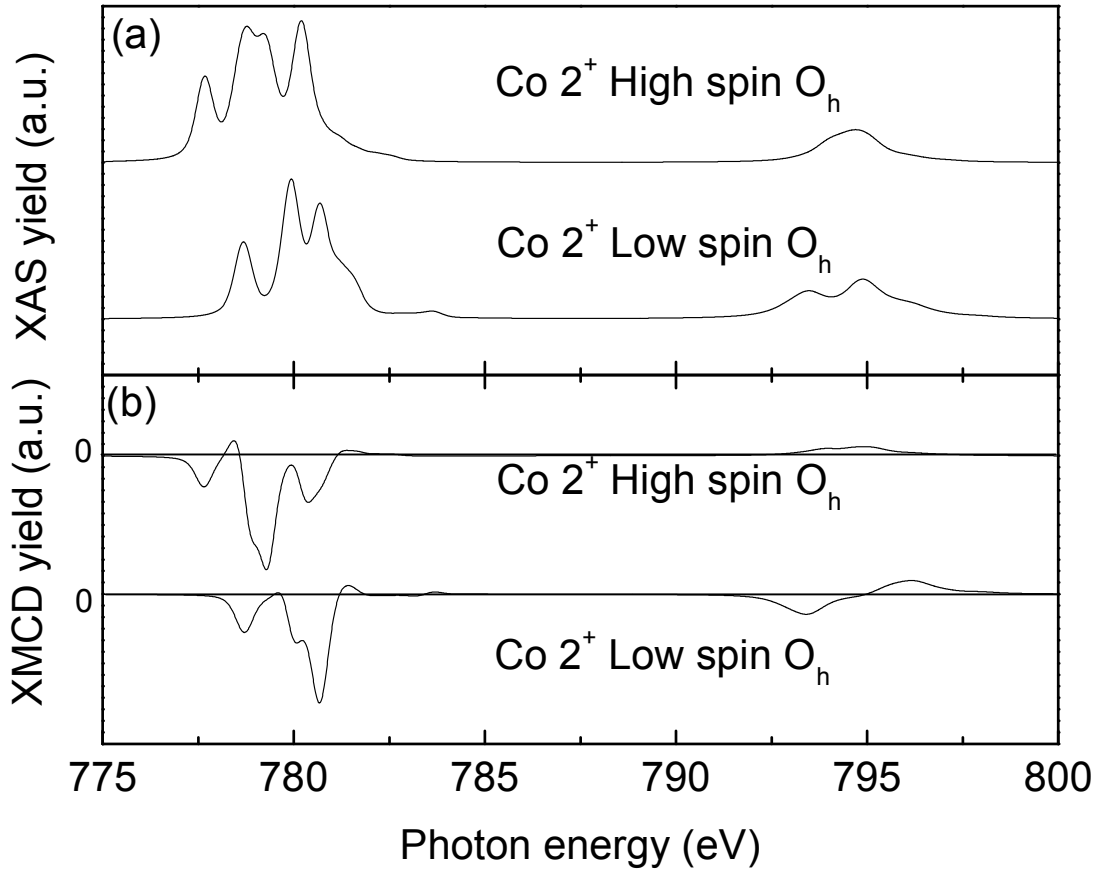

Figure 4.9 Comparison of the atomic multiplet calculation of XAS (a) and corresponding XMCD spectra (b) between high and low spin state.

The overall good agreement in the energy position of multiplet features (except for a small shift of the two central peaks B and C) between the calculated multiplet spectrum and the experimental spectrum shows that the samples contain substitutional Co^{2+} (e.g. Co^{2+} ions coordinated to six oxygen atoms resulting in an octahedral field)

The multiplet structure in XAS/XMCD spectra can be used to deduce detailed information on the electronic configuration and coordination environment of the Co-ions, as shown next. Figure 4.9 shows atomic multiplet calculations of XAS and corresponding XMCD spectra for low spin and high spin Co^{2+}. The high spin state is calculated with

Co^{2+} ions in a cubic crystal field (O_h symmetry) with $10D_q$ = 1.1 eV (as above), and the low spin state with $10D_q$ = 2.5 eV. The transition from high spin to low spin occurs when $10D_q$ surpasses $2J$ where J is the on-site exchange integral. If Co^{2+} ions contribute to magnetism, the XMCD spectra would correspond to Figure 4.9 (b). A distinct difference between different spin states can be recognized with ease. The multiplet structure in XMCD depends sensitively on a number of different characteristics of the Co-species, in particular the electronic configuration (i.e. charge state), a high- or low spin state, and the symmetry of the crystal field. Therefore, the spectral shape of the XMCD signal renders critical information on whether Co metallic or ionic states contribute to magnetism.

We now turn to the experimental XMCD results of oxygen rich and oxygen poor samples. The top panel of Figure 4.10 shows XMCD spectra (blue lines) of oxygen rich (10^{-3} mbar) and oxygen poor films (9×10^{-5} mbar), obtained by subtracting XAS measurements (black and red) performed with circularly polarized light for opposite magnetization directions [23]. The XMCD spectrum of the oxygen rich sample, which shows paramagnetism as concluded previously from magnetometry [11], was measured under application of a small magnetic field (0.08 T). The sample grown under oxygen poor conditions is ferromagnetic and was measured in remanence at zero magnetic field, after application of a 0.5 T field. A clear XMCD signal is observed for both films. It is larger by about a factor of 1.7 for the oxygen poor film. Additional XMCD measurements were performed on a reference Co metal thin film, shown in the bottom panel together with the normalized XMCD data for the $Co:TiO_2$ films. Also shown is the simulated XMCD spectrum of Co^{2+} ions in an octahedral crystal field (corresponding to the high-spin calculation in Figure 4.9). Strikingly, the XMCD spectra of both $Co:TiO_2$ films are very similar to the featureless Co-metal spectrum. This strongly suggests that the magnetic moments arise from the presence of metallic Co in the $Co:TiO_2$.

However, it should be noted that the data do not allow us to conclude that *all* magnetic moments arise from metallic Co alone. The spectra can, within the accuracy of the measurement, also be described reasonably by metallic Co (featureless XMCD) plus a contribution to the magnetism from Co-ions (XMCD with atomic multiplet structure) of up to 30%. These superimposed contributions would produce an XMCD spectrum with a weak multiplet structure that is hard to distinguish from the XMCD spectrum of pure Co metal. This is illustrated with Figure 4.11, which shows Co metallic (measured from 2nm thick Co metal thin film) and Co^{2+} ionic XMCD spectra (calculated) are superimposed with a varying intensity ratio. The multiplet structure in the XMCD spectra containing up to 30 % (in terms of a relative amplitude) Co^{2+} cannot be distinguished easily.

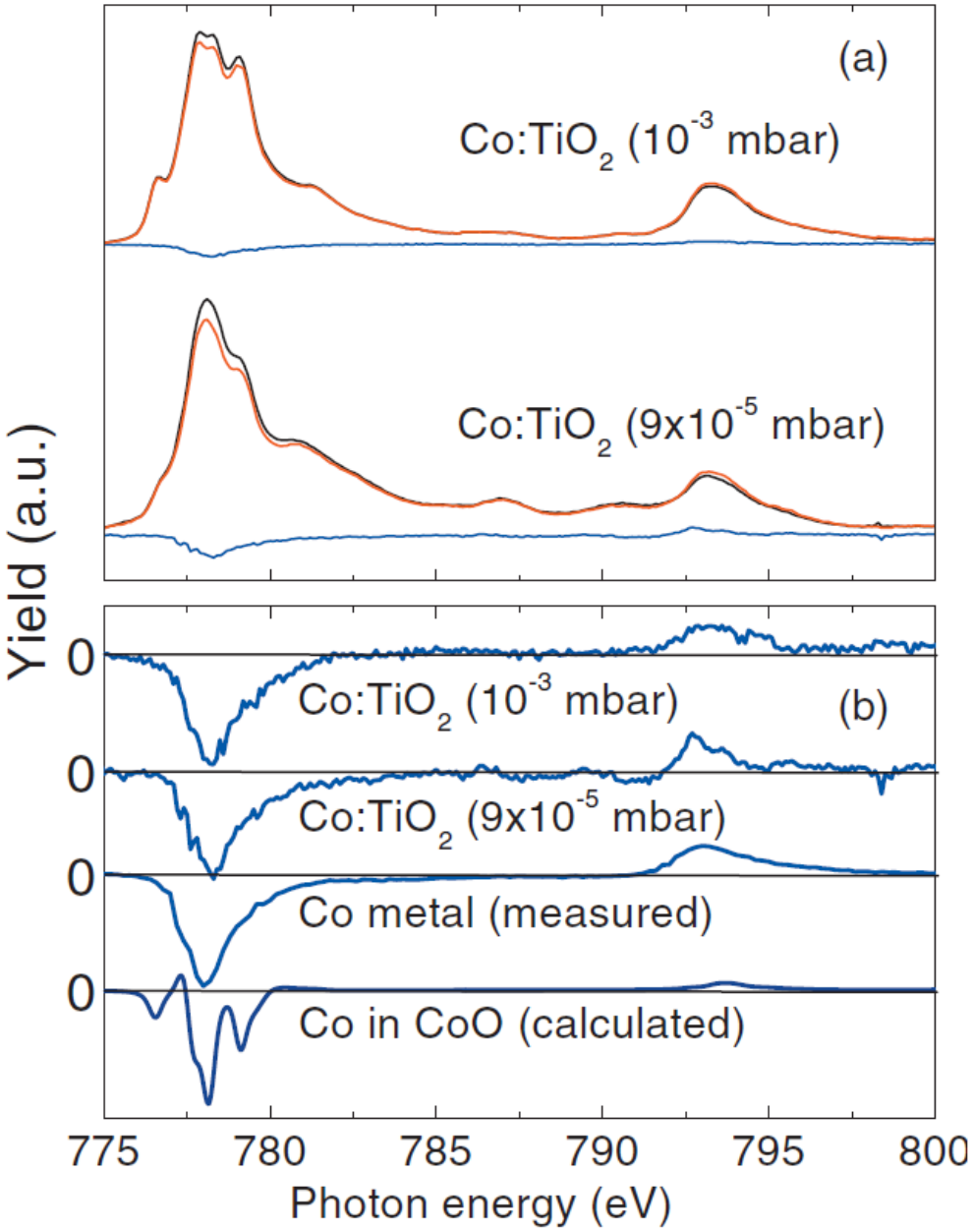

Figure 4.10 (a) Two Co $L_{2,3}$ edge XAS spectra recorded with circularly polarized light of helicity anti-parallel (red line, I^-) and parallel (black line, I^+) to the magnetization, respectively, for a 45 nm Co:TiO2 film grown at 10^{-3} mbar oxygen, and a 10 nm Co:TiO2 film grown at 9×10^{-5} mbar oxygen. Also shown (in blue line) is the resulting $L_{2,3}$ edge XMCD, obtained as the difference ($I^- - I^+$). (b) Magnified $L_{2,3}$ edge XMCD, displayed together with the XMCD of a 2 nm thick reference Co metal film, and the simulated XMCD spectrum of Co^{2+} in O_h symmetry. The four spectra are normalized to obtain the same peak amplitude around 778 eV [23].

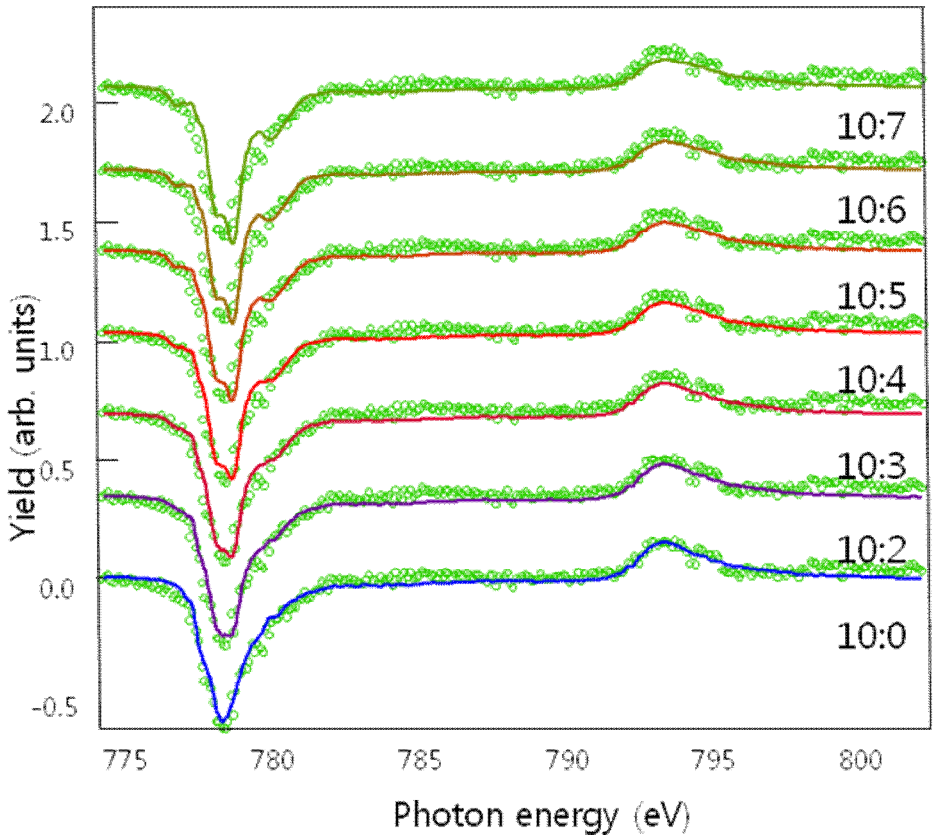

Figure 4.11 Weighted sums of XMCD of metallic Co (measured from 2nm Co thin film) and Co 2+ ionic (calculated with the same parameters as used in Figure 4.8).

The results described above show that the Co distribution is heterogeneous, consisting of metallic Co (as seen in XMCD) and ionic Co^{2+} (as seen in XAS). This suggests that the suppressed XAS multiplet structure in oxygen poor sample is related to a featureless Co metal contribution superimposed on the spectral features related to Co^{2+} ions. To test whether this indeed yields a reasonable description of the results, we subtracted weighted Co-metal spectra (blue lines in Fig. 4.12) obtained from the Co-metal reference sample. The difference spectra after subtraction (red lines in Fig. 4.12) represent the Co^{2+} contributions, and indeed show a more pronounced multiplet structure. The weight of the subtracted Co-metal contribution was taken such that, for both samples, the multiplet features labeled B, C, and D, are all at about the same height in the difference spectra. Using this criterion, the difference curves closely mimic the spectral shape of CoO, which contains Co^{2+} in an octahedral crystal field of essentially the same strength (1.05±0.05 eV [24]) as we deduce for Co:TiO_2 (1.1 eV) from LFM calculations. Note that it is preferable to compare with experimental data of "standard" samples when possible, due to the fact that LFM calculations do not capture all the details of the experiments. The weights of the metallic Co contribution to the total XAS intensity amount to 60% and 40% (in terms of peak heights) for the Co:TiO_2 films grown under oxygen poor and

oxygen rich conditions, respectively. The stronger suppression of the Co^{2+} multiplet structure for the oxygen-poor grown Co:TiO_2 sample is thus consistent with the presence of a larger amount of metallic Co. After the Co metal contribution is subtracted, the multiplet features (red lines) are not exactly the same for the two samples. There is some additional broadening of the multiplet structure for the oxygen-poor grown film that cannot be explained exclusively by the presence of a metallic Co contribution. This broadening can be due to variations in the local crystal fields, perhaps due to oxygen vacancies and/or other defect structures. In addition, we cannot completely rule out some finite contribution of hybridization with (and magnetic coupling to) conduction electrons, which would result in effects on the XAS spectrum of Co:TiO_2 that remain unknown.

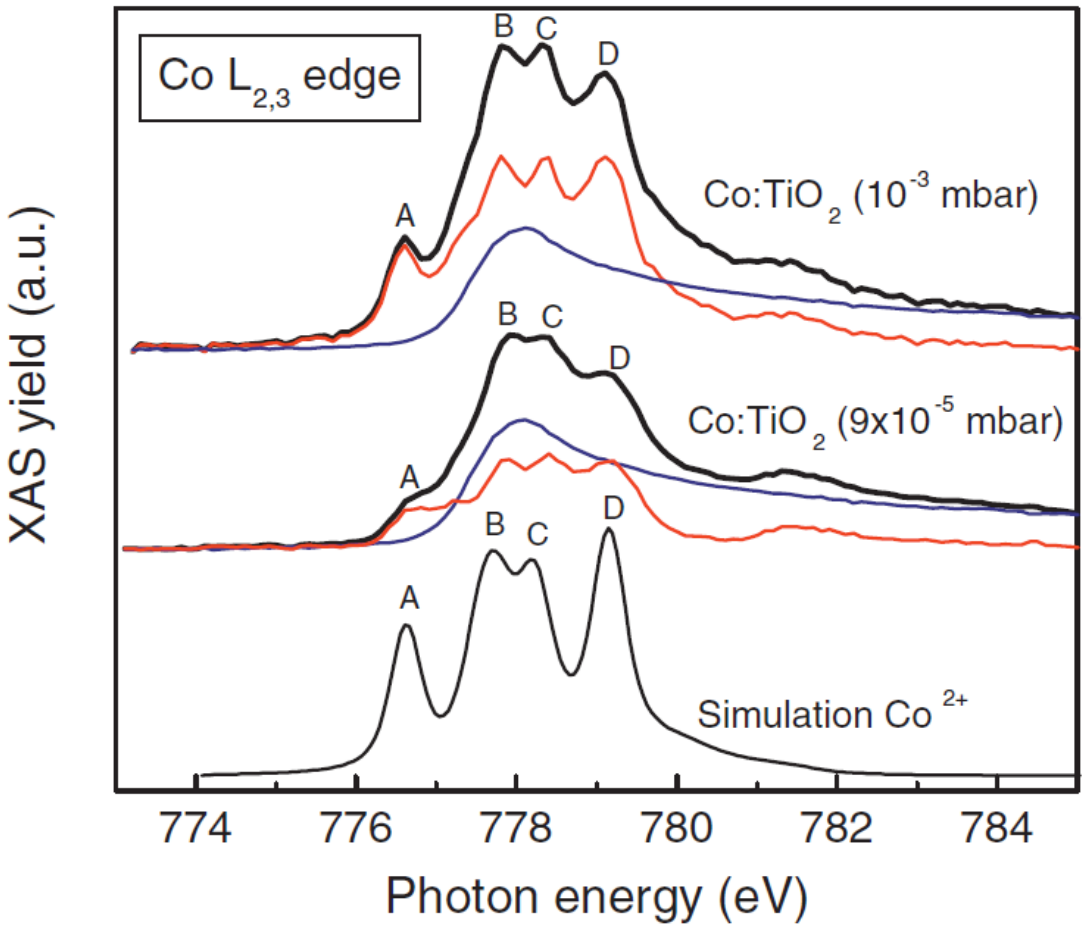

Figure 4.12 Black lines: experimental XAS data of a 45 nm Co:TiO_2 film grown at 10^{-3} mbar oxygen, a 10 nm film grown at 9×10^{-5} mbar oxygen, and the simulated spectrum of Co^{2+} ions. Red lines: difference spectra with a much clearer fine structure obtained by subtraction of a weighted metallic Co contribution (blue lines) from the measured XAS spectra, as described in the text.

4.4 HRTEM and EFTEM study of Co segregation

We performed crosssectional bright field imaging, HRTEM and complementary EF-TEM measurements on 45nm thick oxygen rich-, 45nm thick oxygen poor-, and 160nm thick oxygen poor samples. EF-TEM uses specific energy loss peaks of transmitted electrons to obtain spatial maps of the concentration of a particular chemical element.

Figure 4.13 shows cross sectional bright field imaging of both 4.5nm oxygen poor- and oxygen rich samples. The oxygen poor sample exhibits regions of dark contrast underneath outgrowths, which are not observed for the oxygen rich sample. As will be shown EF-TEM analysis, these dark contrast regions correspond to Co-rich phases resulting from Co segregation. Similar evidence for Co segregation is repeatedly observed within the oxygen poor sample below each outgrowth. The average distance between outgrowths is on the order of 1 m, well matched with the distribution of such outgrowths in the AFM image (Figure 4.5b). Figure 4.14 shows high resolution TEM images of both samples, indicating that both films are well ordered and epitaxial. A certain area (Fig. 4.14 (a)) in the oxygen rich sample shows a mosaic spread with moiré fringes due to a superposition of signals arising from different crystal orientations.

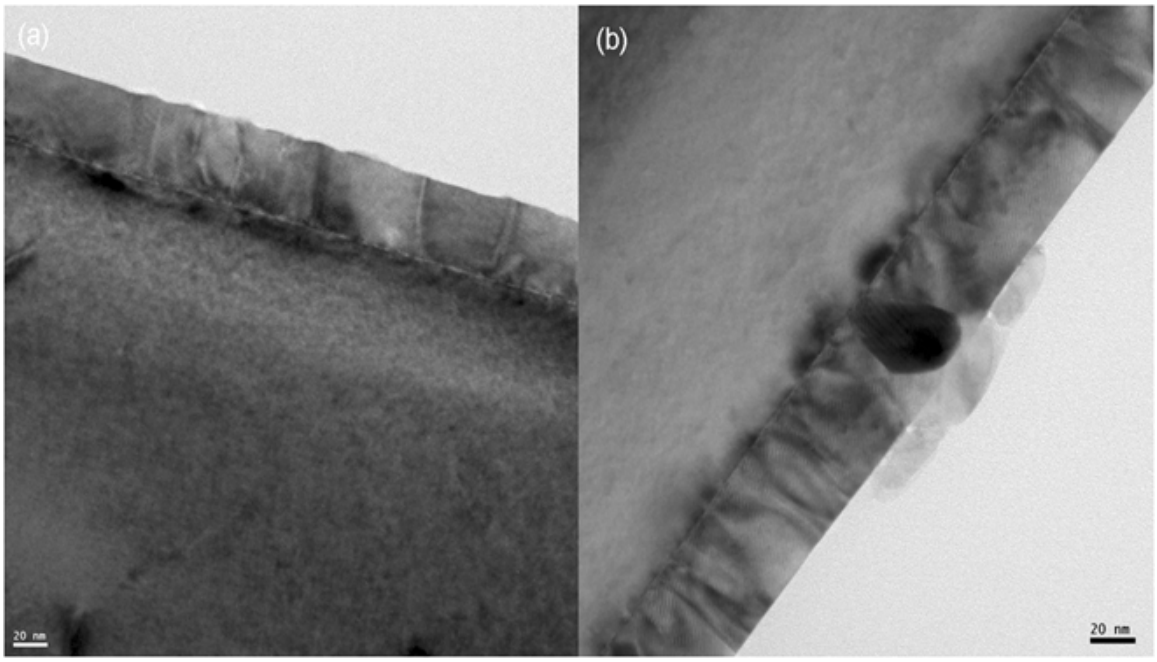

Figure 4.13 Crosssectional bright field images of 45nm thick oxygen rich sample (grown at 10^{-3} mbar oxygen) (a) and 45nm thick oxygen poor sample (grown at 9×10^{-5} mbar oxygen) (b).

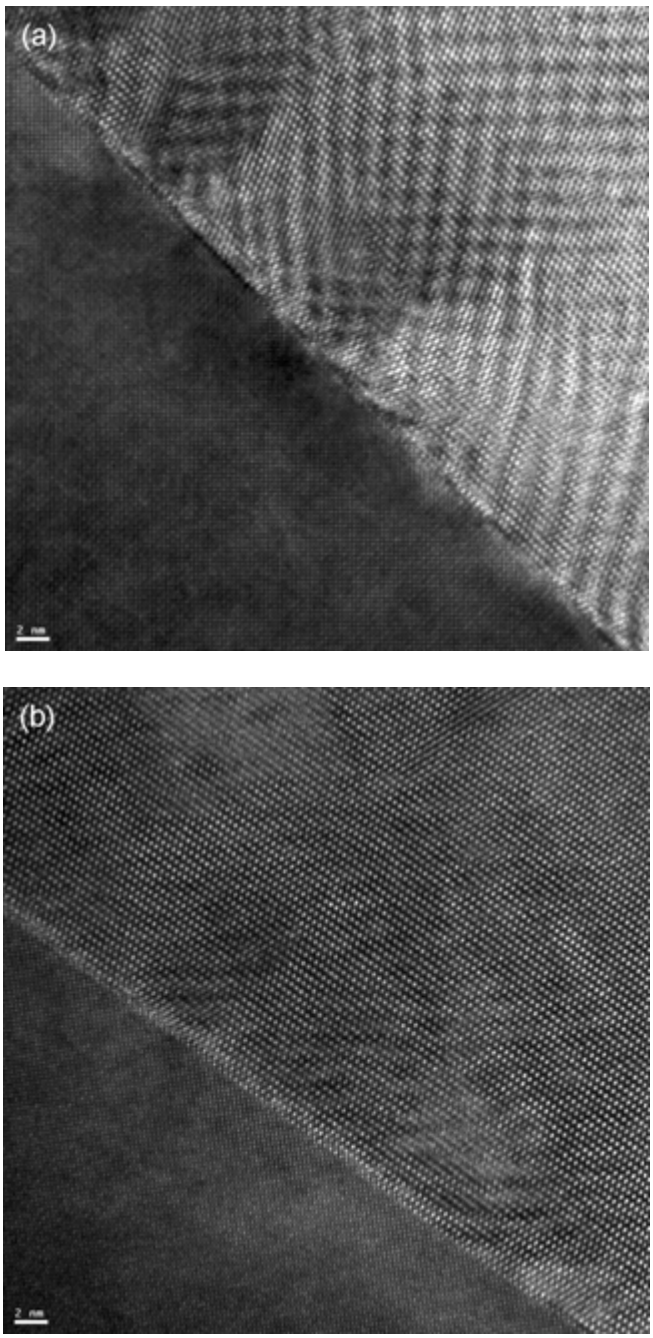

Figure 4.14 Cross sectional high resolution TEM images of a 45nm thick oxygen rich sample (grown at 10^{-3} mbar oxygen) (a) and a 45nm thick oxygen poor sample (grown at 9×10^{-5} mbar oxygen) (b).

Next, we discuss the EF-TEM analysis of the Co:TiO_2 samples, focusing on evidence for Co-segregation. Finding the Co metal clusters in the paramagnetic oxygen rich grown Co:TiO_2 thin film is by no means an easy task considering that the superparamagnetic Co particle size is below 10nm. Notwithstanding, for the Co:TiO_2 thin film grown under oxygen rich conditions, tiny regions of enhanced Co concentration near the surface were observed (Figure 4.15 (a)). In contrast, for the Co:TiO_2 thin film grown under oxygen poor conditions, relatively large Co-rich clusters emanating from the substrate/film interface and spanning the full film thickness (Fig. 4.15 (c)), which appeared as dark contrast regions in bright field imaging (Figure 4.13b), were easily spotted using EF-TEM.

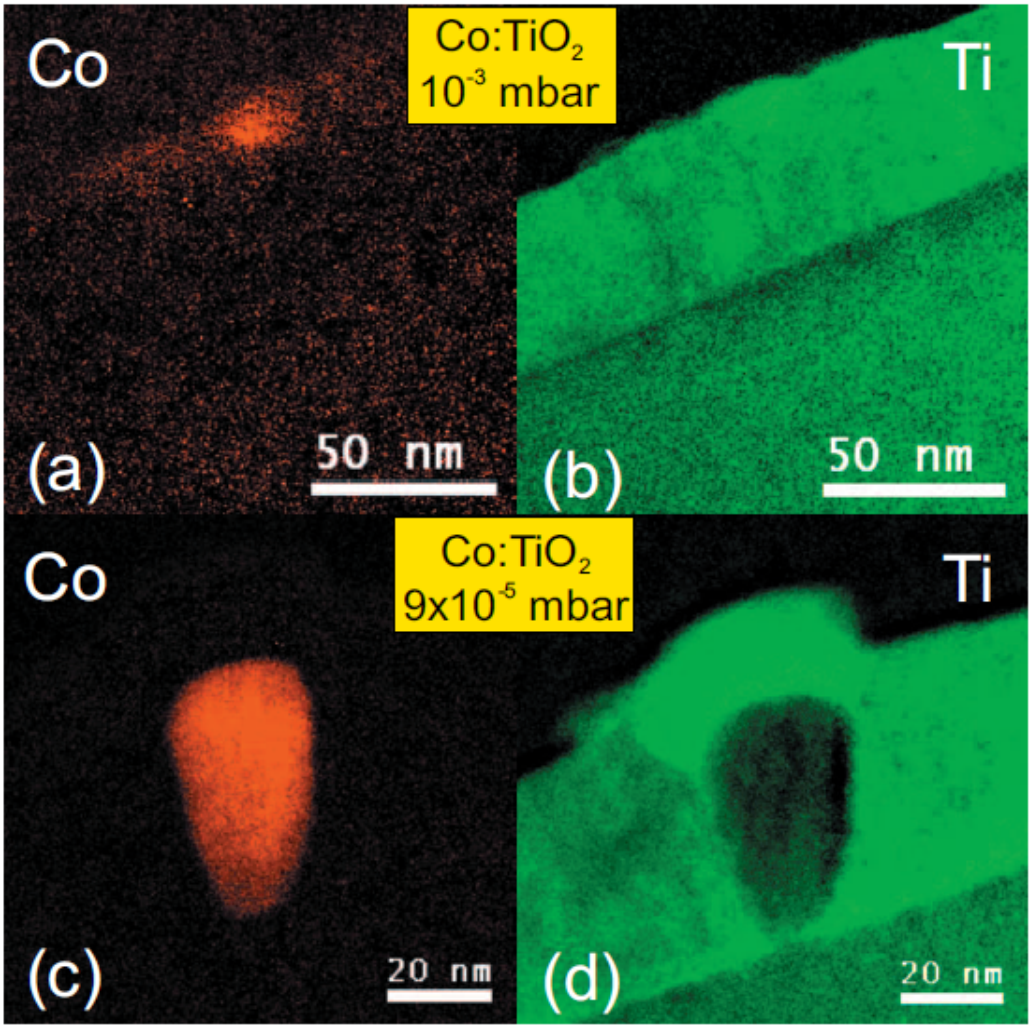

Figure 4.15 EF-TEM images of a 45 nm Co:TiO_2 film grown at 10^{-3} mbar oxygen (a) and (b) and a 45 nm Co:TiO_2 film grown at 9×10^{-5} mbar oxygen (c) and (d). Images (a) and (c) represent maps of the concentration of elemental Co (in red), while (b) and (d) are maps for Ti (in green).

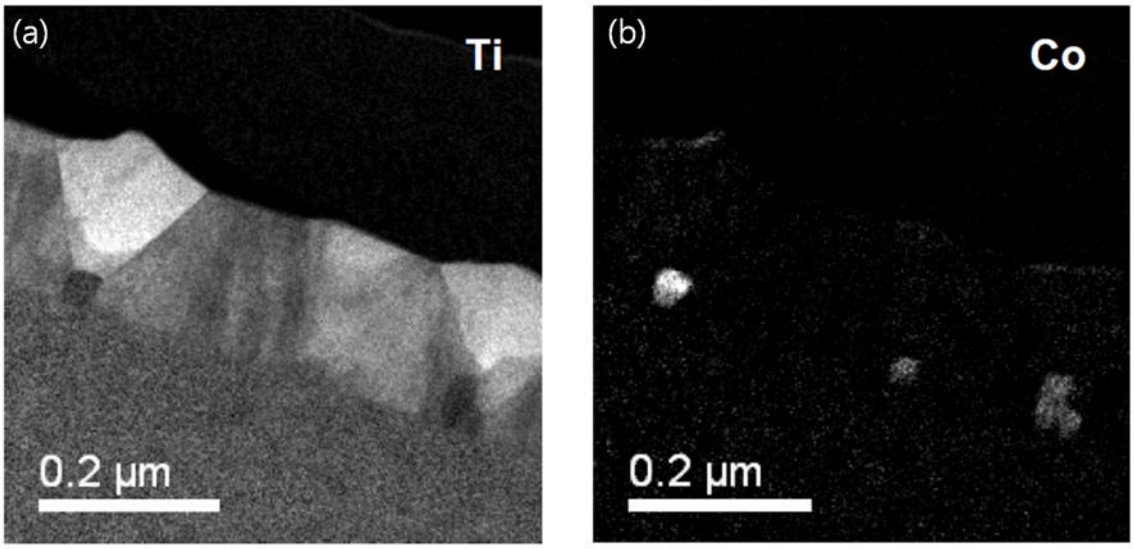

Figure 4.16 EF-TEM images of a 160 nm Co:TiO_2 film grown at 9×10^{-5} mbar oxygen. The image represents the map of the concentration of Ti (a), and Co (b).

Figure 4.16 shows the EF-TEM image of 160nm thick Co:TiO_2 thin film. Again, Co-rich clusters are readily visible, as well the accompanying outgrowths. The (EF-)TEM results confirm the conclusions from the XAS and XMCD measurements that the Co distribution is inhomogeneous. Furthermore, the EF-TEM images confirm that Co-segregation preferentially occurs below a rutile outgrowth, as distinguished in the Ti map, Figure 4.16(a). This suggests that Co diffuses by dislocations and form clusters below a rutile phase which is the more thermodynamically stable polymorph of TiO_2.

4.5 Heterogeneous electronic properties of Co^{2+} ions in Co:TiO_2

Here we discuss a more detailed analysis of the electronic properties of ionic cobalt (Co^{2+}) in Co:TiO_2. XAS spectra reveal heterogeneity other than the previously discussed metallic phases. Charge transfer satellites are found consistently for "thick" (160 nm) films, and not for significantly thinner films. This indicates a variable degree of hybridization with ligand states. We discuss samples with different defect density, which we control via the oxygen pressure during growth, and the film thickness.
We start with a comparison of the Co $L_{2,3}$-edges of three representative Co:TiO_2 thin films with varying defect density, but all with a cobalt concentration of 1.4 at.% (Figure 4.17). The different cases are: a 45nm oxygen rich film, plus 10nm and 160nm thick oxygen poor films. As discussed previously, oxygen rich films exhibit a high structural quality. These oxygen rich films show very flat surfaces (see Figure 4.5 (a)), a well defined epitaxial relation with the STO substrate (Figure 4.14), only very few parasitic phases such as outgrowths and Co-rich clusters (Figure 4.15 (a) and (b)), and sharp Co

$L_{2,3}$-edge features (Figure 4.12). In contrast, oxygen poor samples show an increased roughness (Figure 4.5 (b)), exhibit significantly stronger Co heterogeneity (Figure 4.15 (c) and (d)), and start to show an increasing areal density of rutile outgrowths with increasing thickness (Figure 4.5 (c)). The inclusion of oxygen vacancies stimulates the formation of lattice defects, which become more abundant as the thickness increases and the strain relaxes via the formation of e.g. dislocations.

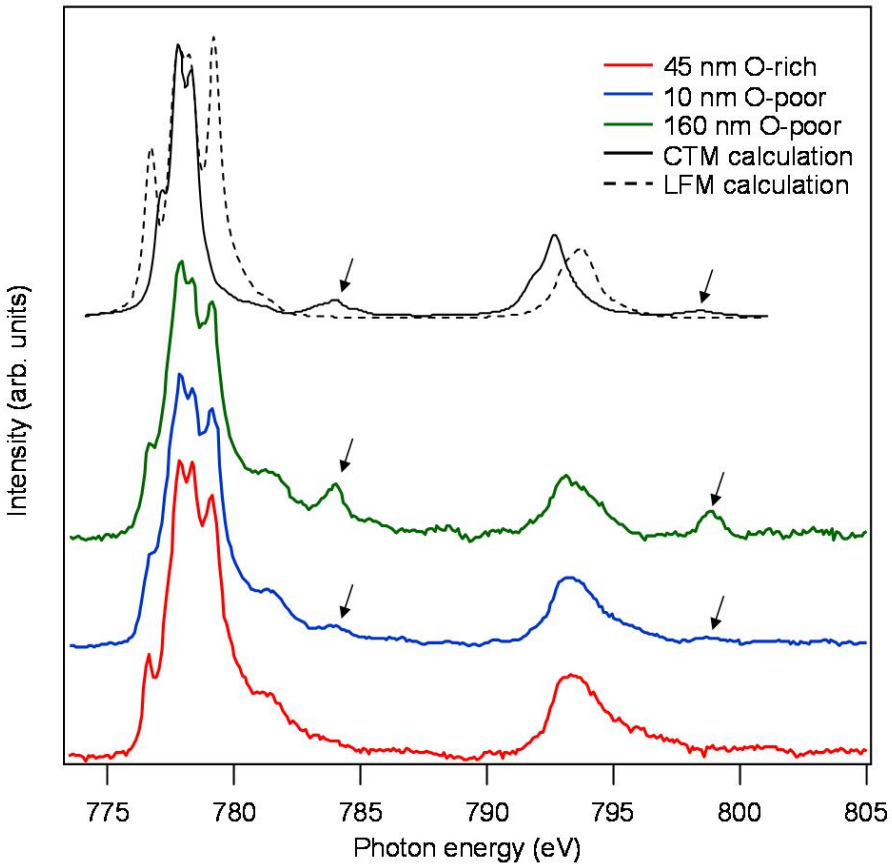

Figure 4.17 Co *L*-edge XAS spectra (normalized to the same height) of three different Co:TiO_2 thin films: a 45 nm oxygen rich film (red, bottom), a 10 nm oxygen poor film (blue, 2nd from bottom), and a 160 nm oxygen poor film (green, 3rd from bottom). Simulated spectra obtained from LFM (black dotted line, top) and CMT (black solid line, top) calculations are also shown.

Upon first inspection, the Co $L_{2,3}$-edge spectra of all three samples look similar. However, we observe a distinct satellite feature, about 7 eV above the L_2 and L_3 edges (marked in arrow), in the XAS spectra of the oxygen poor samples which is absent (or at least too weak to be discernable) for the oxygen rich film. The intensity of this satellite feature is clearly highest for the 160nm thick film. Both the absence of the feature in oxygen rich samples, exhibiting high structural quality, and its increased spectral weight with increasing film thickness, which is known to be accompanied by the formation of defects, points towards a relation between the satellite peak and the defect density. We confirmed these findings for a range of oxygen poor samples prepared under identical

conditions with thickness 10, 20, 40 and 160 nm, and consistently found the strongest satellite features for the thickest films.

It should be pointed out that similar observations have already been made by other researchers, for similar Co-doped oxides. Lussier *et al*. reported Co *L*-edge data of both rutile and anatase Co:TiO_2 (Co concentration 7 at.%) that showed a similar feature for rutile samples, but not for anatase [25]. Although the authors pointed out the difference, the origin of the peak was not explained. Liu *et al*. also observed a satellite feature in Co *L*-edge XAS spectra of Co:ZnO (5 at.% Co) and Co/Al:ZnO (5 at.% Co, 1 at.% Al) [26]. The authors did not include a calculation, but did attribute the feature to ligand-to-metal charge transfer, which they considered to be dependent on the extent of delocalization of donor defect states (e.g. oxygen vacancies and Al ions in their samples).

We now discuss charge transfer multiplet (CTM) calculations (using the same code as used for LFM calculations [21]) in order to explain the presence of the CT satellite peaks. In these calculations, the ground state and final state configurations were modeled as a mixture of $3d^7$ and $3d^8\underline{L}$, where $\underline{L}$ denotes a ligand hole. Such a configuration models a situation in which a part of the ionic charge is transferred to the ligands via hybridization of electronic states. The calculated spectrum shown in Figure 4.17 was obtained by setting the ground state energy difference between the $3d^7$ and $3d^8\underline{L}$ configurations to Δ= 1.5 eV. The energy difference in the final state, i.e. for the configurations $2p^53d^8$ and $2p^53d^9\underline{L}$, was set to $\Delta' = \Delta + U_{pd} + U_{dd}$ = -0.5 eV. It is thus reasonably assumed that the core-hole potential U_{pd} is 2 eV larger than the on-site Hubbard *d*-*d* repulsion energy U_{dd} [27]. The transfer integrals, which determine the effective hopping bandwith that couples the two electronic configurations and are thus a measure of the degree of hybridization, were set to T_{eg} =2 and T_{t2g}=1 eV. These are typical values applied for transition metal oxides featuring σ-bonding, where larger values are expected for e_g orbitals pointing towards the oxygen ligands [27]. The crystal field parameter $10Dq$ was set to 1.1 eV in both initial and final state, as in the LFM calculations. Using these parameters, we obtain a CT satellite feature with a fairly strong intensity, at the same energetic position relative to the main $L_{2,3}$-edges where it appears in the experimental data. In this respect, the CTM calculations seem to describe the observations well. It is clear, however, that a description in which all Co-ions are in a mixed $3d^7$ and $3d^8\underline{L}$ state falls short, since the Co *L*-edge, apart from the satellite, strongly resembles that of a pure $3d^7$ configuration for all samples. This observation again points towards Co heterogeneity, in which some Co ions are strongly coupled to donor defect states in the gap that are energetically close to the 3*d* states, while others are not. Given that the samples indeed contain various different phases (e.g. Co-rich clusters, rutile outgrowths), this is not too surprising. The XAS spectra can thus best be interpreted as a sum of various different contributions, related to a Co^{2+} $3d^7$ configuration, Co^{2+} with a mixed $3d^7$ and $3d^8\underline{L}$ configuration, and metallic Co.

Finally, we show an exceptional case, namely that of a 2 nm Co:TiO_2 film, deposited onto a layer stack comprising STO(substrate)/$La_{0.7}Sr_{0.3}MnO_3$(LSMO 8.5 nm)/STO(3.1nm), similar to structures we used in our studies of magnetic tunnel junctions (MTJs) containing ultrathin Co:TiO_2 layers (see also Chapter 6) [28]. Since the film thickness is merely 2 nm, corresponding to the height of about 2 anatase unit cells (c-axis 0.915 nm), such films exhibit considerable strain as can be deduced from a comparison of the (bulk) lattice parameters: a_{LSMO} = 0.3873 nm, a_{STO} = 0.3905 nm, $a_{anatase}$ = 0.3785 nm. This leads to a distortion of the TiO_6 octahedra away from their equilibrium

geometry, which gives rise to a slightly different quasi octahedral bonding environment for substitutional Co-ions. Indeed, the XAS multiplet structure of the 2 nm Co:TiO_2 film confirms this (Figure 4.18). The multiplet splitting is somewhat reduced as compared to that of thicker films. This can be modeled in the most straightforward way via a reduction of the cubic crystal field strength 10*Dq* (see Figure 4.18). Such a reduced 10*Dq* value is consistent with tensile strain in the Co:TiO_2 film, and a correspondingly larger unit cell volume, resulting from the different lattice parameters of the materials in the stack.

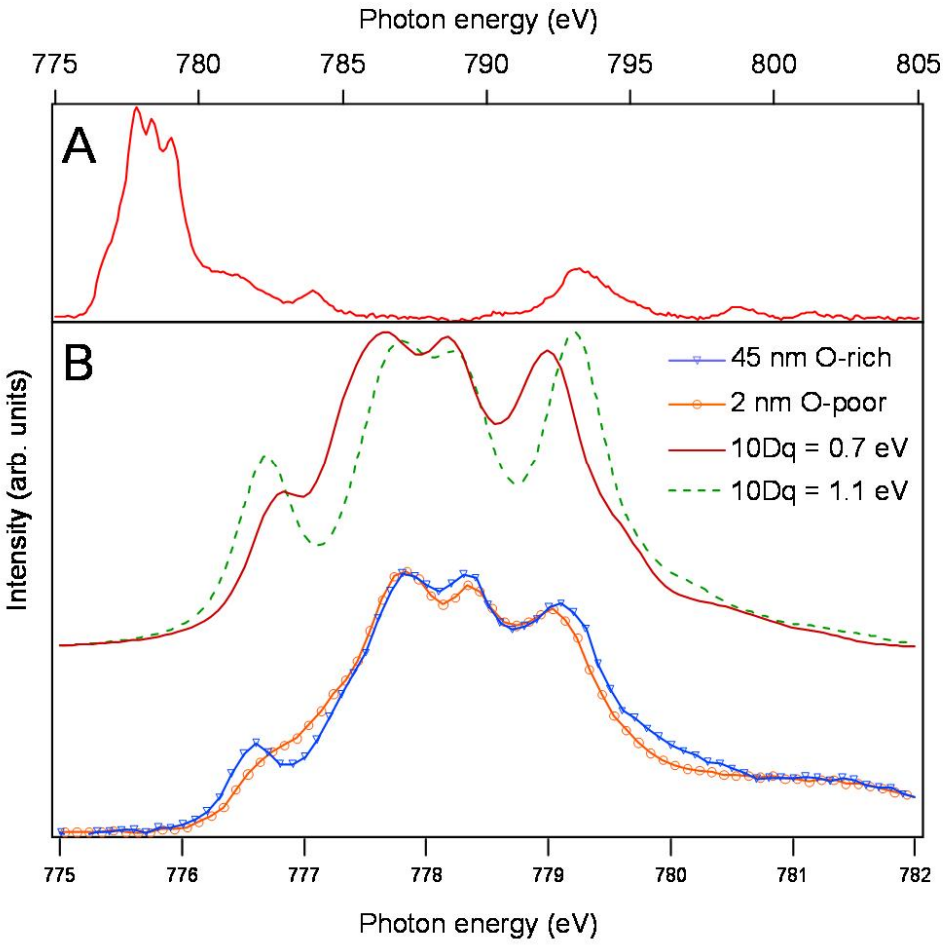

Figure 4.18 (A) Co *L*-edge spectrum of a 2 nm oxygen poor Co:TiO_2 film in a MTJ stack (see text), (B) Co L_3-edge spectra of the same 2 nm Co:TiO_2 film (blue triangles) and a 45nm oxygen rich Co:TiO_2 film (orange circles), accompanied by calculated spectra using LFM calculations with 10*Dq* set to 1.1 eV (green dotted line) and 0.7 eV (red solid line).

Also this sample, comprising a 2 nm Co:TiO_2 film, exhibits clear CT-satellite peaks at the Co *L*-edges. At first this seems surprising considering the discussion above, where the increased intensity of the CT- feature was correlated with a higher density of defect gap-states in thick (e.g. 160 nm) films. For a 2 nm film, a scenario involving stronger CT peaks, as compared to 10 or 20 nm thick films, resulting from a larger density of donor defect states is not realistic. Instead, the CT features may arise from interfacial electronic

states involving Co(3*d*) orbitals, and STO and/or TiO_2 interface states. Indeed, it is expected that Co-ions prefer interfacial positions, due to the large mismatch between the Co^{2+} and Ti^{4+} ionic radii.

4.6 Conclusion

We find that the Co distribution is heterogeneous for Co:TiO_2 films grown under oxygen rich as well as oxygen poor conditions, and more so for the latter. The presence of substitutional Co^{2+} (as observed in XAS spectra) can be correlated with the earlier observation of impurity band conduction [11], whereas metallic Co contributes to the ferromagnetism and AHE (observed with XMCD and EF-TEM) [6]. Based on the XAS spectra, approximately half of the 1.4% Co is estimated to be metallic. Assuming a magnetic moment of 1.7 Bohr magneton per Co metal atom, the corresponding magnetization is 3.2 kA/m. This is consistent with the previously measured [6, 11] remanent magnetization of 2 to 4 kA/m, but smaller than the saturation magnetization (6-8 kA/m). However, the magnetometry data were obtained on thicker films (200 nm). Also, the fraction of metallic Co content derived from the XAS spectra refers to the XAS signal amplitude. Converting this to an atomic fraction needs to take the probing depth and a possible inhomogeneous depth profile of the metal/ion ratio into account.

We also observed distinct satellite peaks at about 7 eV above the main Co *L*-edges, and model these features using charge transfer multiplet calculations. A fairly good agreement is obtained for a mixed $3d^7$ and $3d^8\underline{L}$ electronic configuration with a ground-state energy difference of about 1.5 eV. Strong CT satellite peaks are consistently found for the thickest (160 nm) oxygen poor films. We attribute the CT peaks to the interaction of Co(3*d*) electrons with donor defect states in the band gap (which become more abundant for thicker films), that are energetically close to and significantly hybridized with these Co(3*d*) states. These findings add to the complex, heterogeneous electronic structure of Co:TiO_2 thin films, and may important for the understanding of the rich (magneto-)electronic properties of these materials. Our observation of a relation between the CT satellite intensity and the defect density may be also be helpful for understanding the reports of similar satellite peaks in the literature.

Finally, it should be pointed out that the XMCD data do not completely rule out a finite contribution of magnetism arising from ionic Co magnetic moments. Hence, our data does not establish the complete absence of ferromagnetism and the AHE due to the coupling of Co^{2+} ions by the conduction electrons. Nevertheless, any evidence for ordered Co^{2+} derived magnetic moments is elusive, while there is clear proof for the presence of metallic Co-clusters (EF-TEM) and the corresponding magnetism (XMCD). Our results thus point to an extrinsic origin for magnetism in Co:TiO_2.

References

[1] T. Dietl, H. Ohno, F. Matsukura, J. Cibert, and D. Ferrand, Science **287**, 1019 (2000).

[2] Y. Matsumoto, M. Murakami, T. Shono, T. Hasegawa, T. Fukumura, M. Kawasaki, P. Ahmet, T. Chikyow, S. Koshihara, and H. Koinuma, Science **291**, 854 (2001).

[3] H. Toyosaki, T. Fukumura, Y. Yamada, K. Nakajima, T. Chikyow, T. Hasegawa, H. Koinuma, and M. Kawasaki, Nat. Mater. **3**, 221 (2004).

[4] S. R. Shinde, S. B. Ogale, J. S. Higgins, H. Zheng, A. J. Millis, V. N. Kulkarni, R. Ramesh, R. L. Greene, and T. Venkatesan, Phys. Rev. Lett. **92**, 166601 (2004).

[5] K. Ueno, T. Fukumura, H. Toyosaki, M. Nakano, and M. Kawasaki, Appl. Phys. Lett. **90**, 072103 (2007).

[6] R. Ramaneti, J. C. Lodder, and R. Jansen, Appl. Phys. Lett. **91**, 012502 (2007).

[7] H. Toyosaki, T. Fukumura, Y. Yamada, and M. Kawasaki, Appl. Phys. Lett. **86**, 182503 (2005).

[8] Y. Hirose, T. Hitosugi, Y. Furubayashi, G. Kinoda, K. Inaba, T. Shimada, and T. Hasegawa, Appl. Phys. Lett. **88**, 252508 (2006).

[9] R. J. Kennedy, P. A. Stampe, E. Hu, P. Xiong, S. von Molnar, and Y. Xin, Appl. Phys. Lett. **84**, 2832 (2004).

[10] H. Toyosaki, T. Fukumura, K. Ueno, M. Nakano, and M. Kawasaki, Jpn. J. Appl. Phys., Part 2 **44**, L896 (2005).
[11] R. Ramaneti, J. C. Lodder, and R. Jansen, Phys. Rev. B **76**, 195207 (2007)

[12] E. Hu, S. von Molnar, P. A. Stampe, R. J. Kennedy, and Y. Xin, Appl. Phys. Lett. **92**, 012114 (2008).

[13] J.-Y. Kim, J.-H. Park, B.-G. Park, H.-J. Noh, S.-J. Noh, J. S. Yang, D.-H. Kim, S. D. Bu, T.-W. Noh, H.-J. Lin, H.-H. Hsieh, and C. T. Chen, Phys.Rev. Lett. **90**, 017401 (2003).

[14] T. C. Kaspar, S. M. Heald, C. M. Wang, J. D. Bryan, T. Droubay, V. Shutthanandan, S. Thevuthasan, D. E. McCready, A. J. Kellock, D. R. Gamelin, and S. A. Chambers, Phys. Rev. Lett. **95**, 217203 (2005).

[15] A. Chambers, *Surf. Sci. Rep* **61** (2006), p. 345.

[16] J. M. D. Coey, M. Venkatesan, and C. B. Fitzgerald, Nature. Mater. **4**, 173 (2005).

[17] T. Jungwirth, J. Sinova, J. Masek, J. Kucera, and A. H. MacDonald, Rev. Mod. Phys. **78**, 809 (2006).

[18] P. Gambardella, S. S. Dhesi, S. Gardonio, C. Grazioli, P. Ohresser, and C. Carbone, Phys. Rev. Lett. **88**, 047202 (2002).

[19] J. Stohr. *NEXAFS spectroscopy, springer series in surface science 25*, and J. Stohr, H. C. Siegmann, *Magnetism from fundamental to spin dynamics springer series in solid state sciences vol 152*.

[20] G. van der Laan Phys.Rev. B **41** 12366 (1990).

[21] R. D. Cowan, *The theory of the Atomic Structure and Spectra* (University of California Press, Berkley, 1981); P. H. Butler, *Point Group Symmetry Applications: Methods and Tables* (Plenum, New York, 1981).

[22] K. Mamiya, T. Koide, A. Fujimori, H. Tokano, H. Manaka, A. Tanaka, H. Toyosaki, T. Fukumura, and M. Kawasaki, Appl. Phys. Lett. **89**, 062506 (2006).

[23] Y. J. Lee, M. P. de Jomg, and R. Jansen, Appl. Phys. Lett. **96,** 082506 (2010)

[24] F. M. F. de Groot, M. Abbate, J. van Elp, G. A. Sawatzky, Y. J. Ma, C. T. Chen, and F. Sette, J. Phys.: Condens. Matter **5**, 2277 (1993).

[25] A. Lussier, J. Dvorak, Y.U. Idzerda, S.R. Shinde, S.B. Ogale, and T. Venkatesan, Phys. Scripta **T115**, 623 (2005)

[26] X.C. Liu, E. Shi, Z.Z. Chen, T. Zhang, Y. Zhang, B.Y. Chen, W. Huang., X. Liu, L.X. Song, K.J. Zhou, and M.Q. Cui, Appl. Phys. Lett. **92**, 042502 (2008)

[27] F.M.F. de Groot, Chem. Rev. **101**, 1779 (2001)

[28] Y. J. Lee, A. Kumar, I. J. Vera Marún, M. P. de Jong, and R. Jansen, IEEE Trans. Magn. **46** (2010) 1683

Chapter 5

Anomalous Hall effect and impurity band conduction in anatase Co:TiO_2 magnetic semiconductor

In chapter 5, the effect of introducing a TiO_2 buffer layer at the STO/Co:TiO_2 interface on the magnetic and structural properties of anatase Co:TiO_2 magnetic semiconductor with low Co concentration (1.4 at.%) is investigated by employing complementary techniques such as AHE, VSM, XRD, and EFTEM. In this chapter, we will show that insertion of the buffer layer leads to AHE suppression accompanied by a reduction of the density of Co clusters, and a different depth distribution of such clusters. We check the validity of the indirect impurity band exchange model for anatase Co:TiO_2. We conclude that the experimental findings indicate extrinsic origins of magnetism in Co:TiO_2.

5. 1 Introduction

Dilute magnetic semiconductors (DMS) are characterized by a unique property i.e. carrier mediated magnetism; ferromagnetism and carrier spin polarization are controlled by the carrier density via doping or electrical gating, which makes DMS systems highly interesting for spintronic applications. One of the well known characteristics of dilute magnetic semiconductors is the anomalous Hall effect (AHE), which results from the interaction between carriers and magnetism. The measurements of anomalous Hall effects in a field effect transistor configuration (FET) have played a crucial role in confirming carrier mediated magnetism in (Ga,Mn)As and (In,Mn)As systems by showing electrical control of the Curie temperature (T_c) [1] and magnetization direction [2]. Recently, following theoretical predictions by Dietl [3], wide band gap oxides and nitrides have been extensively studied as a fascinating class for room temperature DMS for practical spintronic applications. In particular, Co doped TiO_2 (Co:TiO_2) is one of the most extensively studied materials which have been reported to show room temperature ferromagnetism [4], magneto-optical dichroism [5-6], and AHE in rutile, anatase, and even amorphous phase [7-10].

However, the origin of ferromagnetism at room temperature in Co:TiO_2 remains controversial. Numerous, partially conflicting, observations have been reported that point towards both intrinsic and extrinsic magnetic behavior. The controversy persists partially due to the fact that the presence of a small amount of heterogeneity in otherwise homogeneous samples may escape detection by (in-house) structural characterization methods such as x-ray diffraction (XRD) and high resolution transmission electron microscopy (HRTEM). The observation of ferromagnetic signals using standard, macroscopic magnetometry techniques such as vibrating sample magnetometry (VSM) and superconducting quantum interference device (SQUID) measurements in such samples can therefore not be taken as unambiguous proof of intrinsic carrier mediated magnetism. Furthermore, even the presence of AHE cannot be considered as a definite

test for carrier mediated magnetism in dilute magnetic semiconductors, since reports show that AHE is observed along with the presence of Co clusters [11]. Figure 5.1 shows a TEM image of highly reduced rutile Co:TiO_2 (2 at.%), which exhibits AHE, revealing Co nano-clusters (9-10nm) at the interface. Zhang *et al.* observed AHE in (La,Sr) TiO_3 thin films containing deliberately embedded super-paramagnetic Co clusters [12]. They suggested that magnetic Co clusters polarize nearby electrons, which leads to extrinsic spin-orbit scattering. When the magnetic moments on the individual Co clusters are aligned, this results in a net transverse current. This mechanism is described in Figure 5.2.

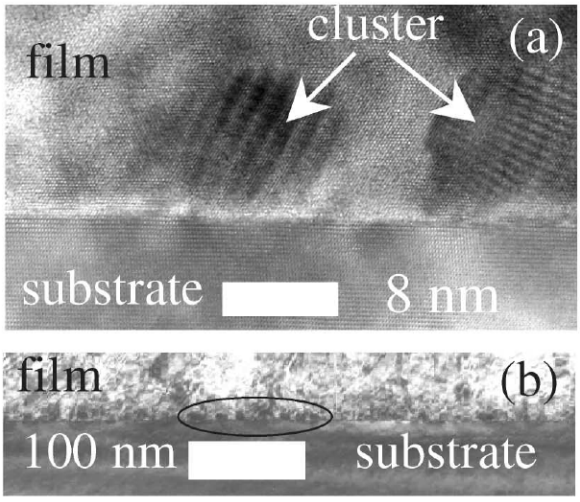

Figure 5.1 TEM images ((a) and (b)) of the $Ti_{0.98}Co_{0.02}O_2$ film at different magnifications. Some of the clusters are marked in image (b) by a black loop [11].

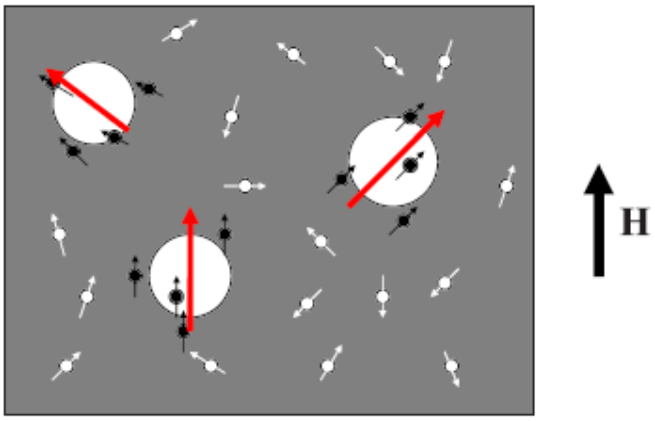

Figure 5.2 The cluster (big white dot) spins are oriented by an external magnetic field and polarize nearby conduction electrons (small black dot) [12].

In addition, no theoretical prediction has rendered a satisfactory explanation for the observed phenomena in ferromagnetic oxides. The initial theoretical prediction concerns p-type Mn doped oxides and nitrides [3], while the oxides reported to exhibit room temperature magnetism are n-type, containing oxygen vacancies. At a later stage, theoretical predictions suggested that ferromangetic exchange interaction between magnetic dopants might be mediated via carriers in the conduction band [13], or in an impurity band [14]. However, it is worth noting that most of the reports on rutile and anatase Co:TiO_2 show that claims of magnetic properties involve thin films grown under rather low oxygen pressures (typically below 10^{-5}mbar) while exhibiting relatively high Co doping concentrations (above 5 at.% Co), which are both known to play a significant role in the formation of Co-rich clusters. Considering the above in combination with the fact that there are also many reports of the observation of room temperature magnetism along with the presence of Co clusters [15-17], the validity of the claims of intrinsic, carrier mediated magnetism is debatable.

In previous reports, we observed room temperature ferromagnetism, AHE [9], and impurity band conduction in anatase Co:TiO_2 with low Co concentration (1.4 at.%) grown under oxygen poor conditions [18]. These observations are, in principle, consistent with a mechanism of indirect ferromagnetic exchange interaction mediated by carriers in a spin-split impurity band [14], indicating intrinsic carrier mediated magnetism. Figure 5.3 shows plots of the Hall coefficient, R_H, as a function of temperature for films grown at different oxygen pressure.

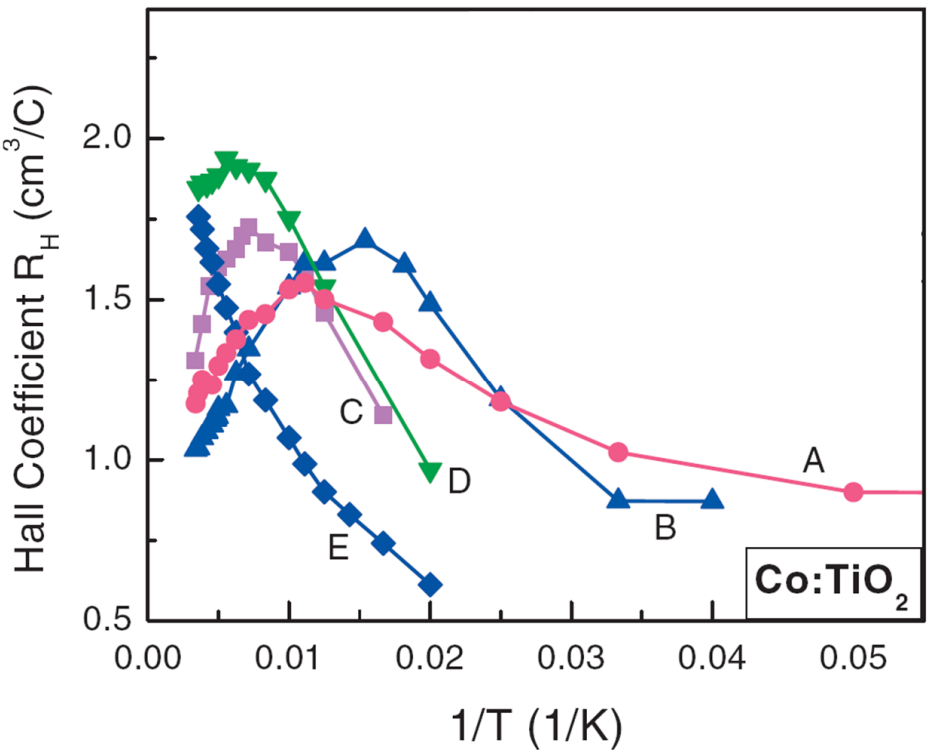

Figure 5.3 Hall coefficient for Co:TiO_2 films grown at 5 Hz and different oxygen pressure: (A) 7×10^{-5} mbar, (B) 5×10^{-4} mbar, (C) 8×10^{-4} mbar, (D) 2×10^{-3} mbar, and (E) 6×10^{-3} mbar.

A clear maximum is observed in R_H that shifts from low to high temperature as the oxygen pressure during growth increases. The Hall maximum is characteristic for systems featuring the presence of two competing conduction channels [19-20]. At high *T*, transport is dominated by conduction band electrons thermally excited from shallow donors, while at low *T*, transport is dominated by carriers in a donor-derived impurity band. The shift in the Hall maximum towards higher *T* for more oxgygen-rich films is fully consistent with such a picture. A reduction of the amount of oxygen vacancies (i,e, shallow donors) leads to narrowing of the impurity band, which in turn results in a higher activation energy for exciting carriers into the conduction band.

Here, we study the effect of inserting a TiO_2 buffer layer at the STO/Co:TiO_2 interface on the magnetic and structural properties of anatase Co:TiO_2 grown under oxygen poor (9×10^{-5} mbar) conditions with complementary techniques such as AHE, VSM, XRD, and EFTEM. Since the Co distribution is heterogeneous for Co:TiO_2 films grown on STO under oxygen poor conditions, as studied in the aforementioned previous report [16], a TiO_2 buffer layer is introduced in order to increase the homogeneity of Co. Furthermore, we will investigate the validity of the employment of AHE for verification of carrier mediated magnetism, and check whether or not the indirect impurity exchange model applies to Co:TiO_2.

5.2 Experimental details

Epitaxial thin films of anatase Co:TiO_2 (1.4 at.%) with/without TiO_2 buffer layer (20nm, 10^{-3} mbar, 550^{o}C) were grown by pulsed laser deposition on TiO_2-terminated (100) $SrTiO_3$ substrates under oxygen poor (9×10^{-5}mbar) conditions. X-ray diffraction, using a high resolution 4 circle x-ray diffractometer, was carried out to investigate the structural properties of 165 nm thick Co:TiO_2 films, with/without buffer layer, and to check for Co heterogeneity. The details of the measurements are described in Ch.4.2. Magnetization measurements were performed with a vibrating sample magnetometer (VSM) at room temperature, on 160 nm thick Co:TiO_2 films with/without buffer layer. Electrical transport characterization, including Hall and resistivity measurements, was conducted in a temperature range from 10 to 300 K using a four terminal van der Pauw geometry in magnetic fields up to 1 T. EFTEM and HRTEM measurement were performed on 40 and 160 nm thick Co:TiO_2 films with/without buffer layer.

5.3 Results

Figure 5.4 and 5.5 show θ-2θ x-ray diffraction spectra measured on 165nm thick Co:TiO_2 films without and with buffer layer respectively. Since a θ-2θ scan investigates only out-of-plane Bragg points in the reciprocal space, it may not be a robust characterization method to detect otherwise offset grown Co clusters (different c-axis orientation). However, clear evidence for the presence of Co metal clusters is nevertheless detected in case of the Co:TiO_2 film without buffer layer (Figure 5.5). Even offset θ-2θ scans (not shown), also reveal Co peaks, thus showing the evidence of randomly oriented Co clusters in the entire film. It should be noted that the AHE measurements in Ref. [9] were carried out for films (550, 185nm) thicker than 160nm, also grown without buffer layer. Since clustering has been shown to be more prevalent as the film thickness increases (see

also TEM and EFTEM measurements presented in Ch 4), this means that AHE occurs in presence of Co clusters.

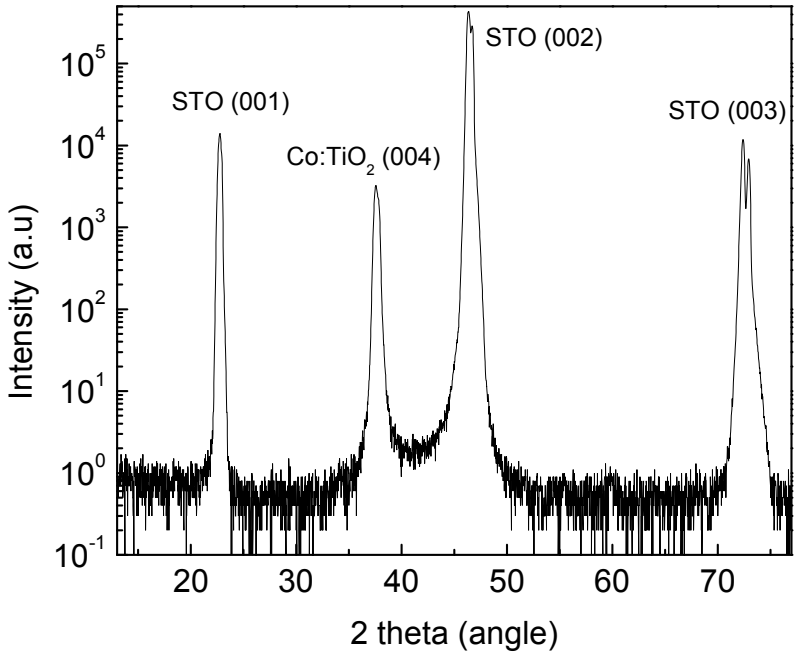

Figure 5.4 θ-2θ x-ray diffraction spectrum of a 160nm Co:TiO_2 film (9×10^{-5} mbar) with buffer layer

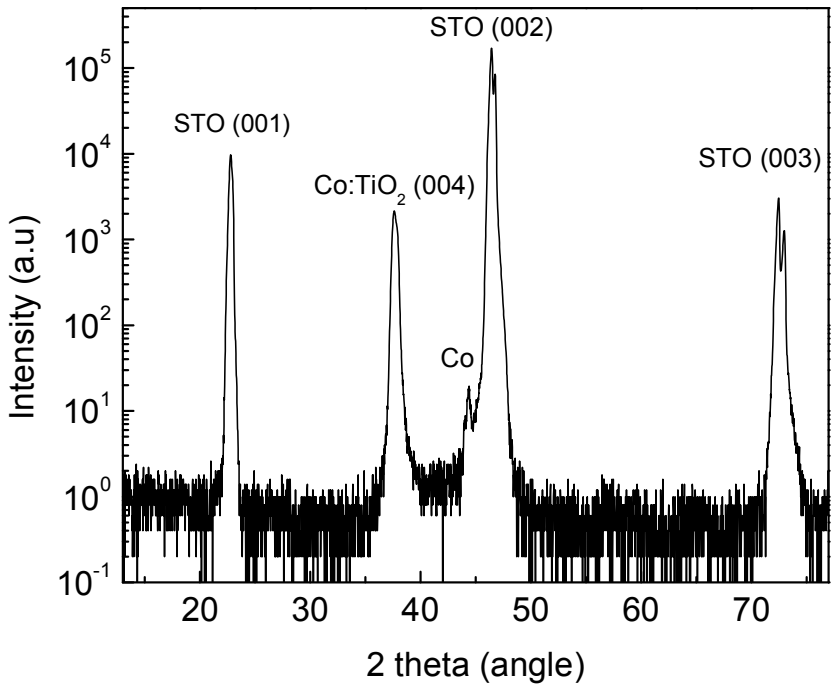

Figure 5.5 θ-2θ x-ray diffraction spectrum of a 165nm Co:TiO_2 film (9×10^{-5} mbar) without buffer layer.

In contrast, the Co:TiO_2 film with buffer layer does not exhibit any traces of Co clusters in the XRD spectrum (see Figure 5.4). It can thus be concluded that, in this case, the amount of metallic Co is below the detection limit.

AFM and EFTEM measurements show that, indeed, the insertion of the buffer layer results in clear differences concerning the formation and distribution of Co clusters in the thin film. EFTEM analysis reveals that Co clustering is accompanied by the formation of rutile outgrowths (see also Chapter 4), which emanate from the Co clusters and protrude significantly from the surface. Hence, by mapping the areal density of such outgrowths using AFM, we can also obtain an estimate of amount of Co clusters per unit area. Figure 5.6 shows that a significantly reduced areal density of rutile outgrowths (and thus Co clusters) is present on Co:TiO_2 thin films when the buffer layer is inserted. However, Co:TiO_2 thin films with buffer layer show a higher RMS roughness, 53nm, than without buffer, 25nm, despite the reduced areal density of the outgrowths. This is due to the fact that the height of outgrowths on Co:TiO_2 thin films with buffer layer is higher (~200nm) than is the case for films without buffer layer (~70nm).

This difference in height is correlated with the location at which the Co clusters form, as is evident from the EFTEM results displayed in Figure 5.7 and 5.8. For films without buffer layer, the Co clusters are located at the film/substrate interface, while they appear close to the surface if a buffer layer is included. From this observation we conclude that the buffer layer plays a prominent role in reducing the amount of defects at the interface, such as dislocations and grain boundaries, which are favored nucleation sites of Co clusters and the accompanying rutile outgrowths. Instead, Co clusters form at defects sites within the films, most probably generated above a certain critical thickness. This is clearly illustrated by Figure 5.7, which shows that Co clusters emanate at the surface for 45nm Co:TiO_2 thin film *with* buffer layer, not at the interface. In stark contrast, Co clusters segregate from the interface and span the entire film thickness for a 45nm Co:TiO_2 thin film *without* buffer layer. The formation of Co clusters above the critical thickness in Co:TiO_2 thin film with buffer layer results in higher rutile outgrowths than is the case for films without buffer layer.

Upon combining the AFM and EFTEM results, it is clear that the insertion of a buffer layer leads to (1) a reduction of the density of clusters and outgrowths, and (2) the formation of Co clusters above a critical thickness. This verifies that the insertion of a buffer layer produces a more homogeneous Co distribution in the thin film. However, it is worth noting that Co clusters are still observed in Co:TiO_2 thin films with buffer layer by EFTEM measurements, but not by XRD (see Figure 5.4). This confirms that XRD is not a robust technique to detect a small number of tiny metallic clusters in the thin film. This analysis shows that it requires carefulness when employing XRD for confirming the homogeneity of doping elements in DMS research.

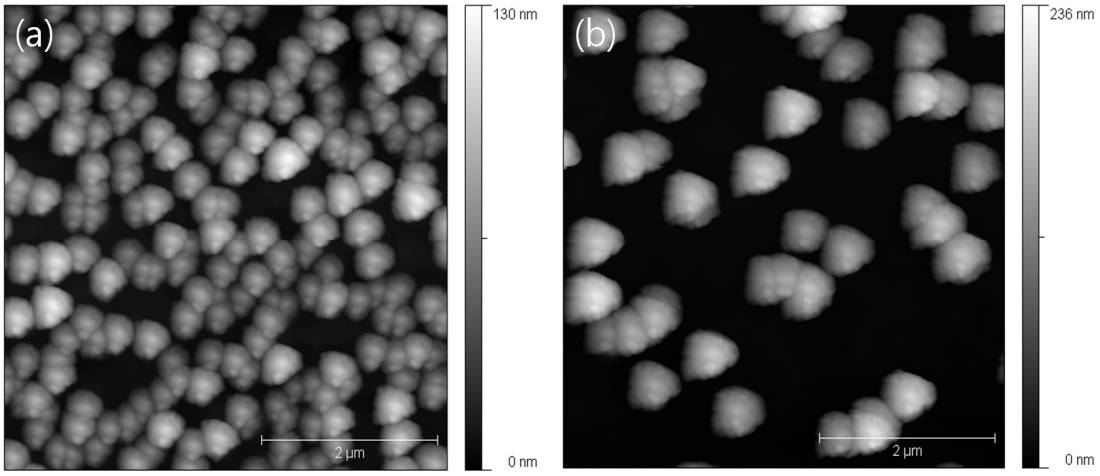

Figure 5.6 (a) AFM images of a 165nm thick oxygen poor sample (grown at 9×10^{-5} mbar oxygen) without buffer layer (RMS roughness: 25nm), (b) 160nm thick oxygen poor sample with buffer layer (RMS roughness 53nm)

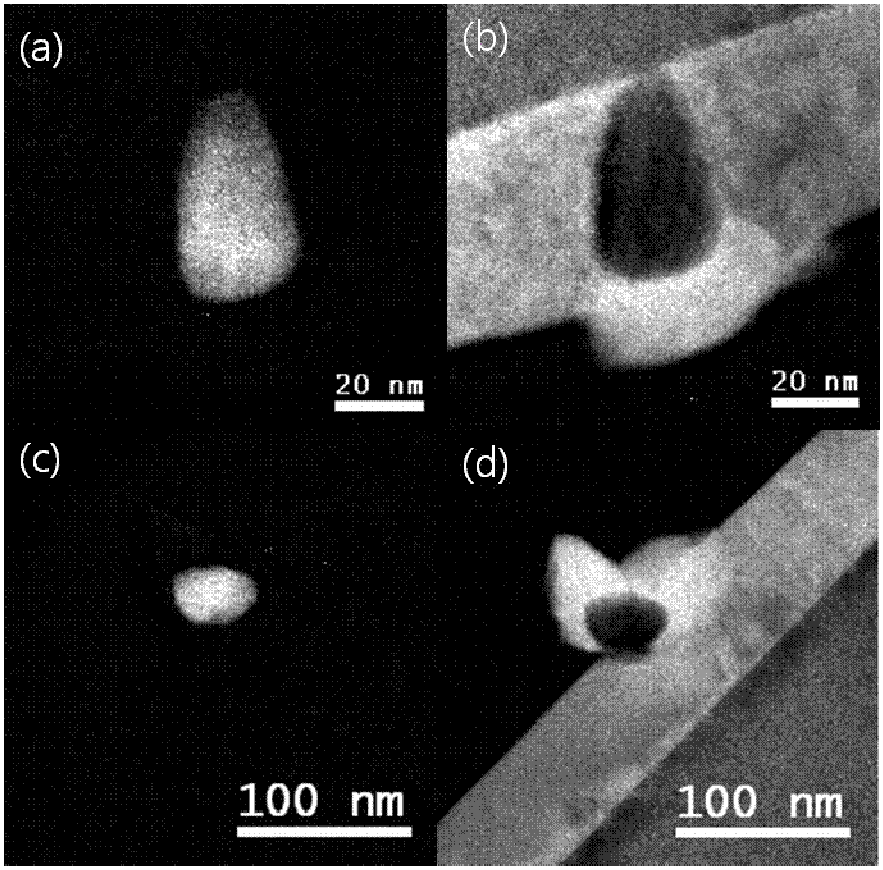

Figure 5.7 EF-TEM images of a 45 nm Co:TiO_2 film grown at 9×10^{-5} mbar oxygen without buffer layer (a) and (b) and Co:TiO_2 film grown at the same oxygen pressure with buffer layer (20nm) (c) and (d). Images (a) and (c) represent maps of the concentration of elemental Co (in white), while (b) and (d) are maps for Ti (in white).

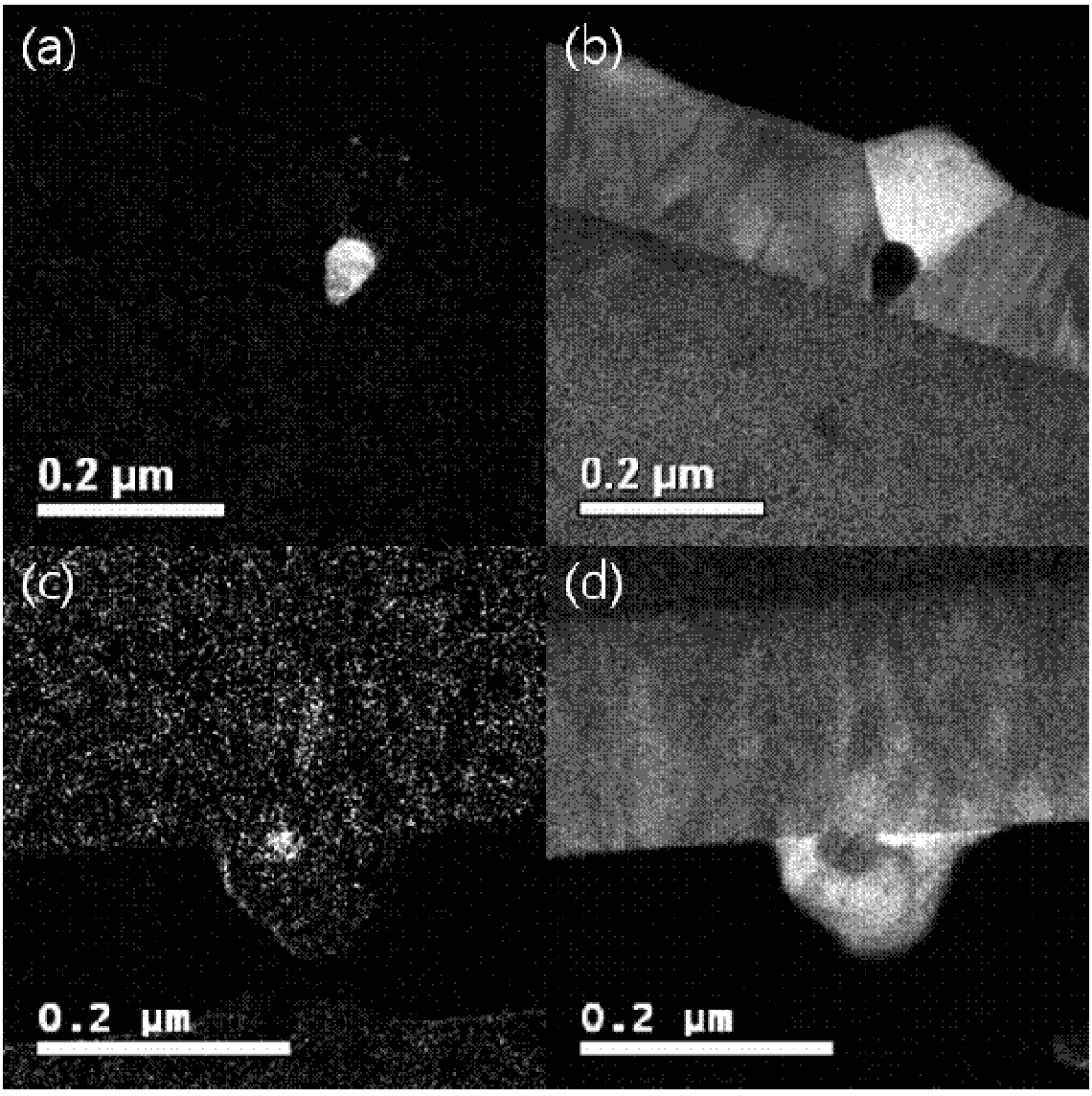

Figure 5.8 EF-TEM images of a 165 nm Co:TiO_2 film grown at 9×10^{-5} mbar oxygen without buffer layer (a) and (b) and Co:TiO_2 film grown at the same oxygen pressure with buffer layer (20nm) (c) and (d). Images (a) and (c) represent maps of the concentration of elemental Co (in white), while (b) and (d) are maps for Ti (in white).

Next, we describe electrical transport measurements of 165nm thick Co:TiO_2 thin films with and without buffer layer. Figure 5.9 shows the resistivity versus temperature, between 10 and 300K. The resistivity ρ of the Co:TiO_2 thin film without buffer is about a factor of two or three smaller than that of the film with buffer, within the whole temperature range. The resistivity of Co:TiO_2 films with and without buffer layer remains relatively constant in magnitude compared to that of pure anatase thin films, indicating degenerate conduction behavior. In contrast, pure anatase thin films show activation transport, for which ρ increases exponentially with $1/T$ within two orders of magnitude [18]. Both films with and without buffer layer do not exhibit hopping transport behavior, as occurs in some systems containing metallic clusters. Such a transport mechanism would be characterized by the relation $\log(\rho) \sim T^{-1/2}$ at low temperature [21].

Figure 5.10 shows the Hall coefficient R_H versus temperature for both Co:TiO_2 films with and without buffer layers. The carrier concentration n_0 is obtained from the relation $R_H = 1/ne$. The carrier concentrations for Co:TiO_2 films with and without buffer layers at room temperature are 8.6×10^{18} /cm^3 and 2.3×10^{19}/cm^3 respectively. The decreased carrier concentration and thus increased resistivity for the Co:TiO_2 thin film with buffer layer (within the whole temperature range) can be related by the fact that the insertion of buffer layer suppresses the rutile outgrowths; The defect density in the films differs, as can be seen for instance from the larger amount of nucleation sites for clusters and outgrowths in films without buffer. Defect sites (e.g. dislocations, vacancies) act as donors, such that a higher density of such defects also produces a higher carrier concentration.

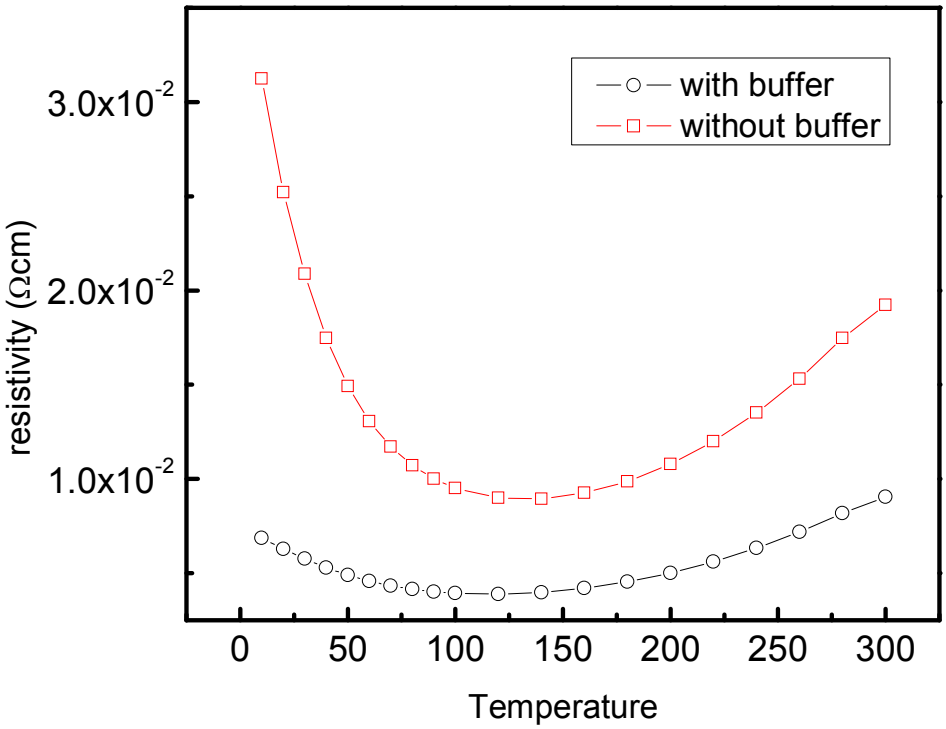

Figure 5.9 Resistivity of 165 nm Co:TiO_2 film grown at 9×10^{-5} mbar oxygen with (open square) and without buffer layer (open circle).

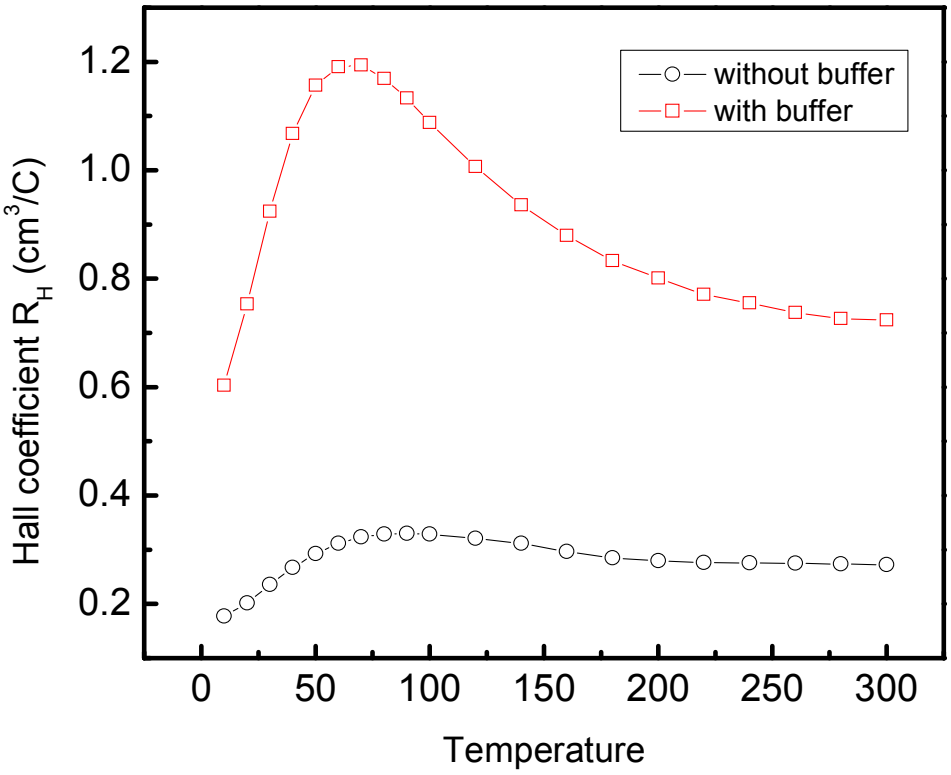

Figure 5.10 Hall coefficient of 165 nm Co:TiO_2 film grown at 9×10^{-5} mbar oxygen with (open square) and without buffer layer (open circle) .

Both Co:TiO_2 films with and without buffer layers show Hall maxima, at 70K and 90K respectively in Figure 5.10. The Hall maximum can be explained by a combination of conduction processes involving different kinds of carriers with different mobility [19]. In heavily doped semiconductors, an impurity band develops above a certain doping (i.e. "impurity") concentration. The impurity band is formed by the finite overlap between wave functions of localized impurities. At high temperature, carriers that are thermally excited into the conduction band dominate the transport behavior, while impurity conduction becomes noticeable at low temperature by a charge exchange between adjacent impurity centers [19,22]. Hung suggested that the competing conduction process in two bands (impurity band and conduction band) results in a single maximum in the Hall curve at a temperature at which the impurity band and conduction band conductivities are similar [22]. Simply, the Hall coefficient and resistivity are expressed as follows by two the band model [19].

$$R_H = \frac{n_c e u_c^{\,2} + n_i e u_i^{\,2}}{\left(n_c e u_c + n_i e u_i\right)^2} \qquad (5.1)$$

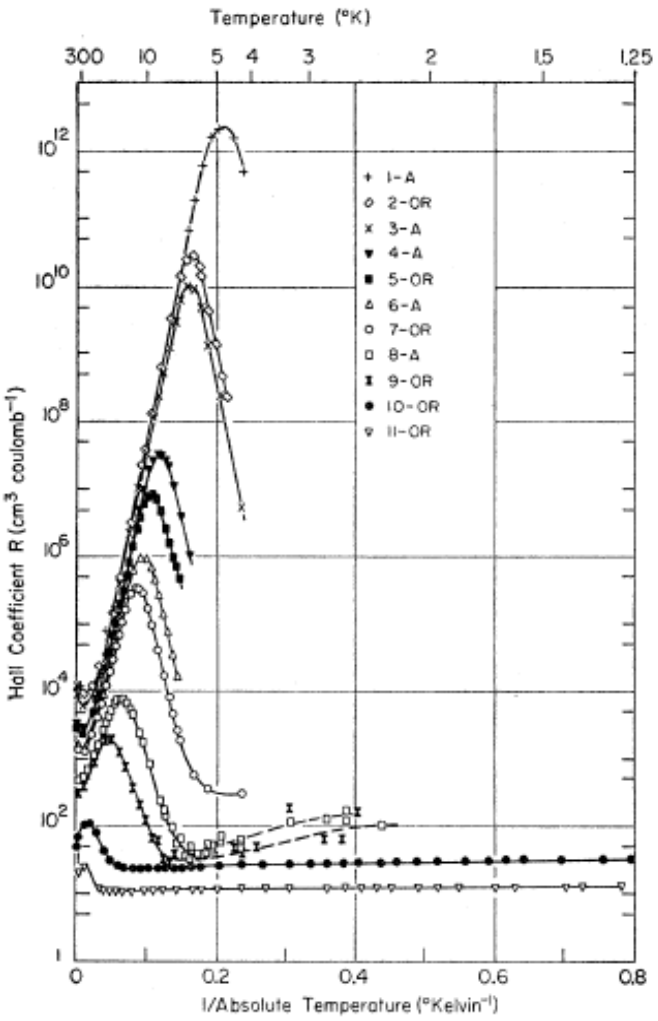

Figure 5.11 Hall coefficient of transmutation doped germanium (*p* type) as a function of 1/*T*. The two lowest curves (solid circle (10 OR) and open inverse triangle (11OR) show metallic conduction behavior with carrier concentration $1.51\times10^{17}/cm^3$ and $4.97\times10^{17}/cm^3$ respectively [22].

$$\rho = 1/(n_c e u_c + n_i e u_i) \qquad (5.2)$$

where n is the carrier concentration, and u is the mobility of conduction band (c) and impurity band (i).

Therefore, the observed Hall maximum for both Co:TiO_2 films with and without buffer layers confirms the presence of an impurity band. It is worth noting the results of the previous work on impurity doped Germanium by Hung in Figure 5.11 [19, 22]. In the case of intermediate doping concentrations ($<10^{16}/cm^3$), the Hall coefficient first increases exponentially upon cooling, then reaches a maximum at a certain temperature (below 10K) and subsequently decreases sharply by several orders in magnitude with decreasing temperature. In contrast, highly doped semiconductors ($10^{17}/cm^3$) do not show

such a large variation (of several orders of magnitude) of the Hall coefficient. In particular, such systems exhibit a virtually temperature independent Hall coefficient at low temperature (below 10K), as 10-OR and 11-OR in Figure 5.11. Increasing the impurity concentration leads to (1) a decrease of the Hall maximum in magnitude, and (2) a shift of the Hall maximum towards higher temperature. These trends are consistent with our results, which show that the Co:TiO_2 film without buffer layer exhibits a lower Hall coefficient (higher carrier concentration) and higher Hall maximum temperature.

From Figure 5.9 and 5.10, the magnitude of the change of the Hall coefficient and the resistivity behavior of both Co:TiO_2 films with and without buffer layer indicates degenerate metallic conduction in an impurity band. This degenerate behavior is explained by the Mott criterion, equation 5.3.

$$n_c^{1/3} r_H > 0.25 \qquad (5.3)$$

When the transfer integral related to the overlap of wave functions surpasses the on-site electron-electron repulsion, the metal-insulator transition occurs [23]. r_H is the effective Bohr radius determined by the dielectric constant and electron effective mass. The critical concentration (n_c) for carrier delocalization for anatase TiO_2 was calculated as 6×10^{18} [18]. The carrier concentrations of both Co:TiO_2 films with and without buffer layers satisfy the Mott criterion.

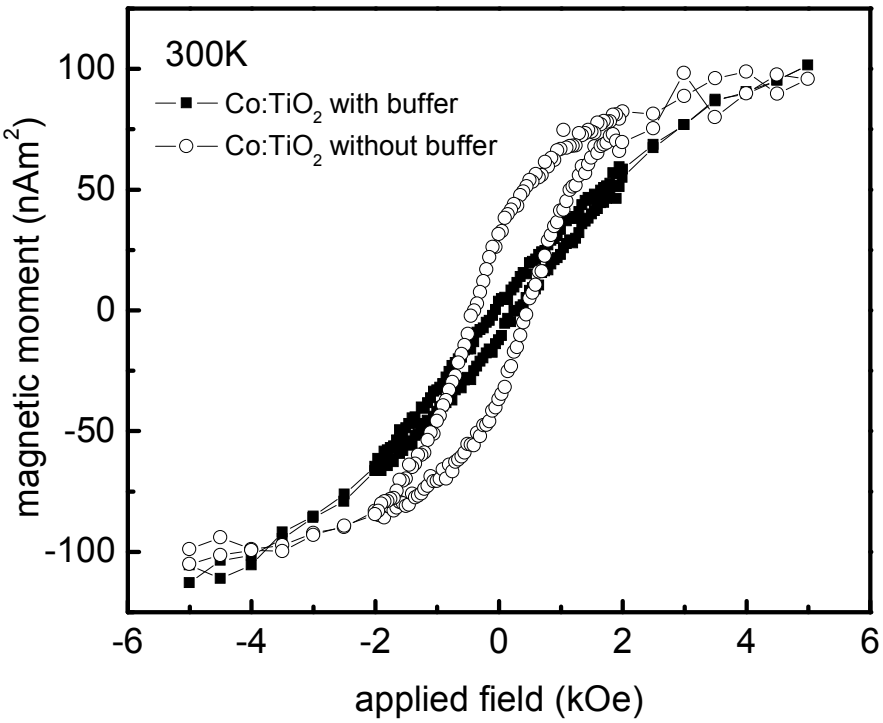

Figure 5.12 Magnetic moment versus out-of-plane field for 165 nm Co:TiO_2 films grown at 9×10^{-5} mbar oxygen with (solid square) and without buffer layer (open circle) at room temperature.

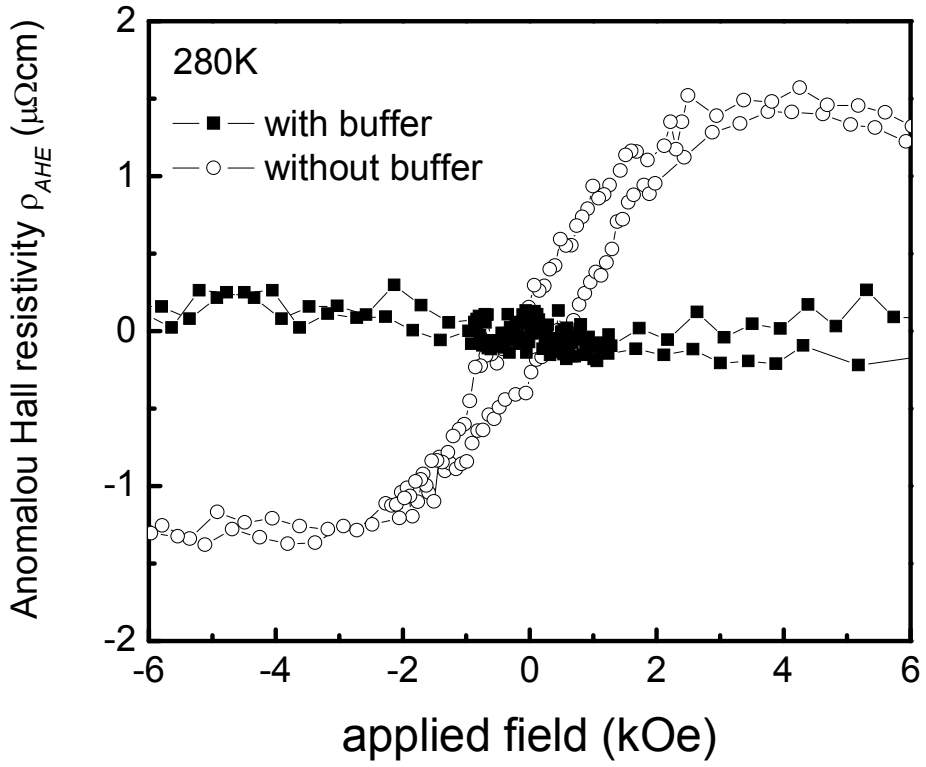

Figure 5.13 Anomalous Hall resistivity after subtracting linear ordinary term for 165 nm Co:TiO_2 films grown at 9×10^{-5} mbar oxygen with (solid square) and without buffer layer (open circle) .

The VSM result in Figure 5.12 shows that both 165 nm thick Co:TiO_2 films with and without buffer layers are ferromagnetic at room temperature. This means that ferromagnetism occurs simultaneously with the presence of metallic impurity band conduction. Impurity band conduction is of interest for establishing the nature of carriers not only in ferromagnetic insulating Mn:GaAs near the metal-insulator transition but also in ferromagnetic insulating oxides. Coey suggested that ferromagnetism can be mediated by the spin split impurity band formed by percolating *F* center defects in oxides [14]. Therefore, it is a highly relevant and hotly debated question whether ferromagnetism in anatase Co:TiO_2 is mediated by carriers in a spin split impurity band and isolated Co magnetic moments, or results from metallic clusters as shown in Figure 5.7 and 5.8.

Figure 5.13 shows the AHE resistivities for 165nm thick Co:TiO_2 films with and without buffer layers, obtained by subtracting the linear ordinary Hall contribution from Hall measurement. The Hall resistivity in ferromagnets is expressed empirically in equation, 5.4, consisting of ordinary and anomalous terms.

$$\rho_{xy} = R_0 B + \mu_0 R_s M \quad (5.4)$$

The first term is the ordinary Hall contribution where R_0 is the ordinary Hall coefficient, and B is the magnetic induction. It is related to the deflected motion of carriers by Lorentz forces proportional to the external magnetic field. The second term is the anomalous term, proportional to the perpendicular component of magnetization (M) in the ferromagnet (R_s: the anomalous Hall coefficient, μ_0: permeability in vacuum).

From the comparison of Figure 5.12 and 5.13, several observations can be made. The most striking finding is that, for the Co:TiO_2 thin film *with* buffer layer, the hysteresis shapes of the AHE and magnetization (VSM) measurements are completely different; the anomalous Hall effect is totally suppressed, while the VSM measurement still shows a ferromagnetic hysteresis loop. In contrast, the ρ_{AHE} for the Co:TiO_2 thin film *without* buffer layer shows only a slightly different hysteresis loop compared to that of the perpendicular magnetization in Figure 5.12; The ρ_{AHE} (M) shows a coercive field of ±440 (480)Oe, and a remanence of about 20 (30)% of the value at saturation. However, it should be noted that Co:TiO_2 thin films without buffer layers above 185nm thickness show a very similar hysteresis shape for ρ_{AHE} and M [9].

The suppressed AHE in Co:TiO_2 films with buffer layers can be explained by the fact that the insertion of the buffer layer reduces the overall density of Co clusters, prevents the nucleation of such clusters at the STO/Co:TiO_2 interface, and instead leads to the formation of Co clusters above a certain critical thickness. The repeatedly formed Co clusters at the interface in Co:TiO_2 films without buffer layers may induce spin polarization by extrinsic (i.e. induced by the clusters) spin orbit scattering, and thus give rise to a transverse anomalous Hall resistivity. In contrast, the AHE in Co:TiO_2 films with buffer layers is suppressed by (1) the reduction of Co clusters and (2) the formation of the Co clusters above a critical thickness, such that they always appear close to the surface of the film, often even inside the rutile outgrowths. From Figure 5.7 and 5.8, it is evident that Co clusters formed in the rutile outgrowths, protruding outside the surface, cannot contribute to the transverse anomalous Hall resistivity, since these clusters are not located within the path of the current that flows through the Co:TiO_2 during the measurement. However, it can be argued that carrier mediated magnetism cannot be ruled out for Co:TiO_2 films with buffer layers, since the twice or three times smaller carrier concentration may reduce the ferromagnetic exchange interaction and thus the AHE signal. However, the insertion of the buffer layers produces also more isolated Co magnetic moments in the thin film (less Co goes into clusters), as can be seen from XRD, and EFTEM results. Therefore, a suppression of the ferromagnetic exchange interaction, by a reduction of the carrier concentration, is not expected. The scenario outlined above, in which a smaller carrier concentration and a reduced density of Co clusters suppresses the AHE in Co:TiO_2 films with buffer layers, is therefore the most plausible.

It is also worth investigating the scaling relation in the observed AHE in Co:TiO_2 films, since the scaling exponent is related to the origin of the AHE. The possible origins of an AHE are classified as an intrinsic mechanism related to the Berry phase of Bloch electrons in solids [24], and two extrinsic ones, skew scattering [25] and the so-called side jump mechanism [26]. The extrinsic origins are related to asymmetric scattering of carriers due to spin orbit interaction. The anomalous resistivity (ρ_{AHE}) in skew scattering has a linear dependence on the longitudinal resistivity (see equation 5.5). The intrinsic mechanism and the side jump effect both have a quadratic dependence (equation 5.6).

$$\rho_{yx}^{AH} \propto \rho_{xx} \qquad (5.5)$$

$$\rho_{yx}^{AH} \propto \rho_{xx}^{2} \qquad (5.6)$$

Recent theory developed by Onoda proposed three different scaling regions with anomalous conductivity (σ_{AHE}) vs longitudinal conductivity (σ_{xx}), [27] and the follow-up experiment by Miyasato confirmed these scaling regions for various ferromagnets, including pure transition metals, oxides, and chalcogenides (see Figure 5.14) [28]. The AHE conductivity is expressed by equation 5.7 and the scaling exponent (α) is dependent on the origin of the AHE.

$$\sigma_{xy}^{AH} = \frac{\rho_{yx}^{AH}}{\rho_{yx}^{2} + \rho_{xx}^{2}} \approx \frac{\rho_{yx}^{AH}}{\rho_{xx}^{2}} = \rho_{yx}^{AH}\sigma_{xx}^{2} = s\sigma_{xx}^{\alpha} \qquad (5.7)$$

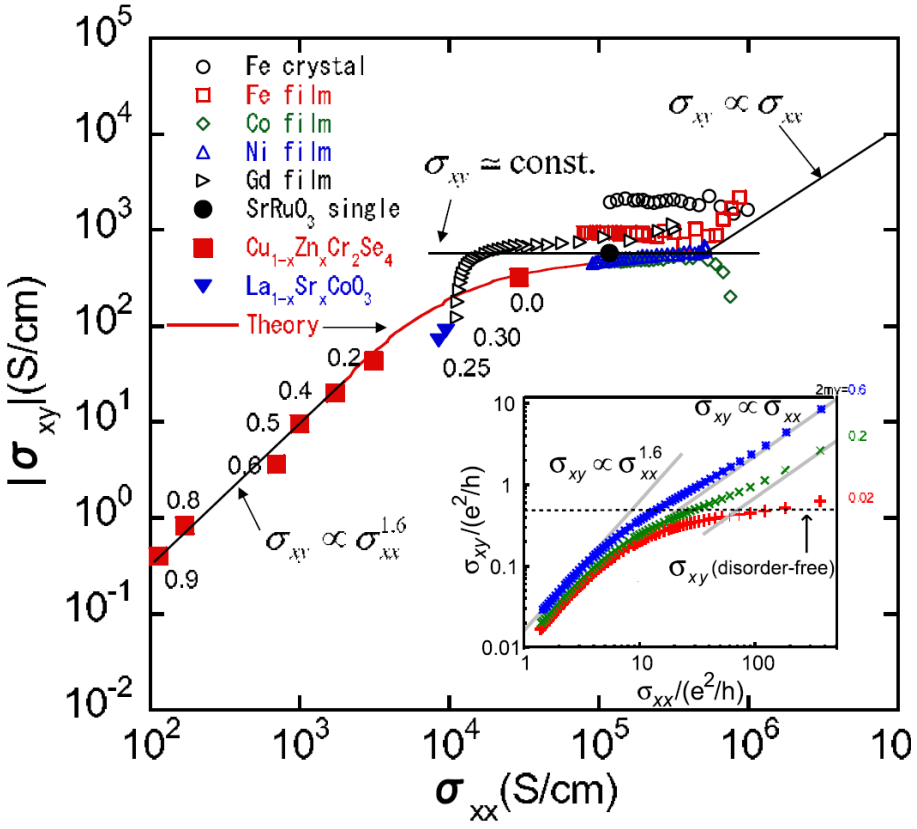

Figure 5.14 Absolute value of anomalous Hall conductivity (σ_{xy}) as a function of longitudinal conductivity (σ_{xx}) in pure metals (Fe, Ni, Co, and Gd), oxides (SrRuO3 and $La_{1-x}Sr_xCoO_3$), and chalcogenide spinels ($Cu_{1-x}Zn_xCr_2Se_4$) at low temperatures [28].

For low conductivity material, α is predicted to be 1.6 [27]. The 1.6 scaling exponent was found experimentally in rutile Co:TiO_2 [29], (Ga,Mn)As [30], and magnetic oxides [31]. The scaling relation is obtained experimentally by changing the conductivity. In intrinsic DMS, a wide range of conductivities can be obtained by changing the temperature or the doping concentration in order to determine the scaling exponent. However, it is difficult to obtain a distinct scaling exponent in anatase Co:TiO_2, since the conductivity does not change much within the whole temperature range. In particular, the anomalous Hall effect in anatase Co:TiO_2 without buffer layer is observed within the whole temperature range. Moreover, the anomalous Hall resistivity remains approximately the same, e.g. is nearly independent on temperature. In contrast, α in rutile Co:TiO_2 is observed as 1.5~1.7. Rutile Co:TiO_2 shows different Hall behavior than anatase Co:TiO_2; for the rutile system, the anomalous term is dominant over the normal Hall term at 300 K, whereas the normal Hall term becomes dominant at lower temperature due to the rapidly decreased carrier concentration by two orders of magnitude (from 10^{22} to 10^{20}) [29].

The observation of AHE with the presence of metallic clusters in Co:TiO_2 thin films is consistent with the previous report by Shinde *et al*. Here, by the insertion of a buffer layer, we however also show that the AHE disappears when the density of Co clusters is reduced, and, perhaps more importantly, the Co clusters form above critical thickness instead of at the substrate/film interface. Due to the latter, many of the clusters reside close to the surface e.g. inside the rutile outgrowths, such that they fall outside of the current path and thus cannot contribute significantly to the AHE. These results confirm that the presence of AHE itself does not mean intrinsic, i.e. carrier mediated, magnetism in DMS research. Zhang pointed out that the AHE originating from extrinsic metallic clusters is featured by a very small value of the ratio of the anomalous Hall resistivity to the longitudinal resistivity ($\rho_{AHE}/\rho_{xx} \sim 10^{-4}$) compared to that ($10^{-2}$) observed in intrinsic DMS [12]. Co:TiO_2 films without buffer layers show very small values of ρ_{AHE}/ρ_{xx}, about 10^{-4}, again indicating the extrinsic origin of the AHE, due to metallic clusters.

Ramaneti *et al.* suggested that strong interaction between Co spins and mobile carriers produces a Kondo effect in anatase Co:TiO_2 films [18], featured by a logarithmic increase of the inverse Hall mobility at low temperature. However, the strong exchange coupling associated with the Kondo effect results in localized donor levels, which will not couple Co magnetic moments ferromagnetically [32]. If a Kondo effect is present in our Co:TiO_2 films, the substitutional (or interstitial) Co^{2+} does not contribute to the ferromagnetism. This would confirm once again that the observed Co clusters are the cause of AHE and ferromagnetism, without any discernible contribution of carrier mediated ferromagnetism. In order to verify the presence of a Kondo effect, we determined the inverse Hall mobility versus temperature of Co:TiO_2 films with and without buffer layers (see Figure 5.15). The measurement shows that the inverse Hall mobility of Co:TiO_2 films with and without buffer layer follows a quasi logarithmic dependence on temperature, in principle consistent with Kondo scattering of the conduction electrons. The corresponding Kondo temperatures, extrapolated to the horizontal axis, are 70K and 110K for Co:TiO_2 films with and without buffer layer respectively. However, considering the fact that the Kondo temperatures determined for the Co:TiO_2 films with and without buffer layer are relatively high compared to those in metals (usually below 10K), this effect may not be related to Kondo scattering but to other scattering mechanisms.

To confirm or rule out whether alternative scattering mechanisms may indeed explain the observations, we scaled the data with the appropriate exponents for various scattering mechanisms. Figure 5.16 shows the Hall mobilities of Co:TiO_2 films with and without buffer layers versus $T^{3/2}$, *i.e.* according to a scaling relation that is featured by ionic scattering at low temperature. It is evident that this scaling relation applies almost perfectly up to 50K (353 $K^{3/2}$) for both Co:TiO_2 films with and without buffer layers. According to this analysis, the temperature dependence of the mobility at low temperature (below 50K) can be fully understood according to an impurity scattering mechanism. Therefore, there is no need to invoke the presence of a Kondo effect in these systems. We thus conclude that Co:TiO_2 does not show a genuine Kondo effect, which was previously thought to arise from a strong interaction between Co spins and electrons in the impurity band.

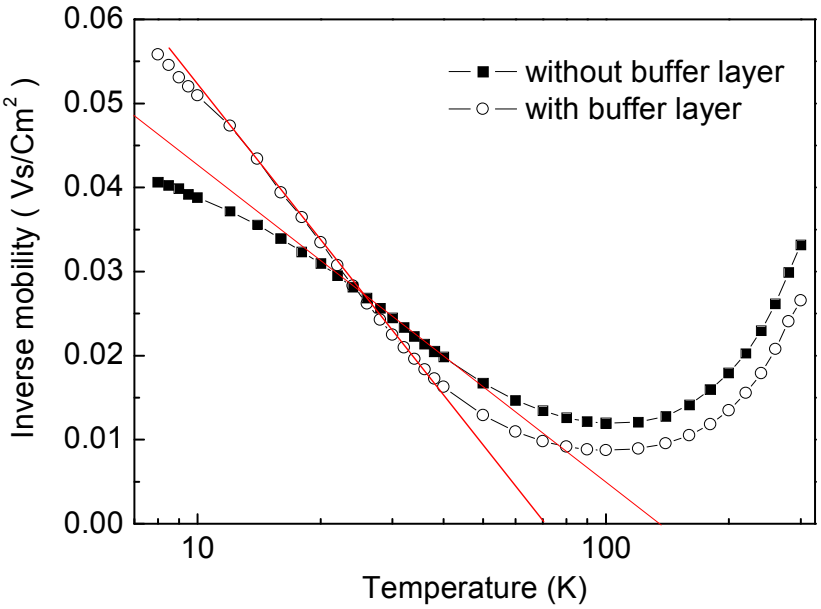

Figure 5.15 Inverse Hall mobilities with temperature for 165 nm Co:TiO_2 films grown at 9×10^{-5} mbar oxygen with (solid square) and without buffer layer (open circle).

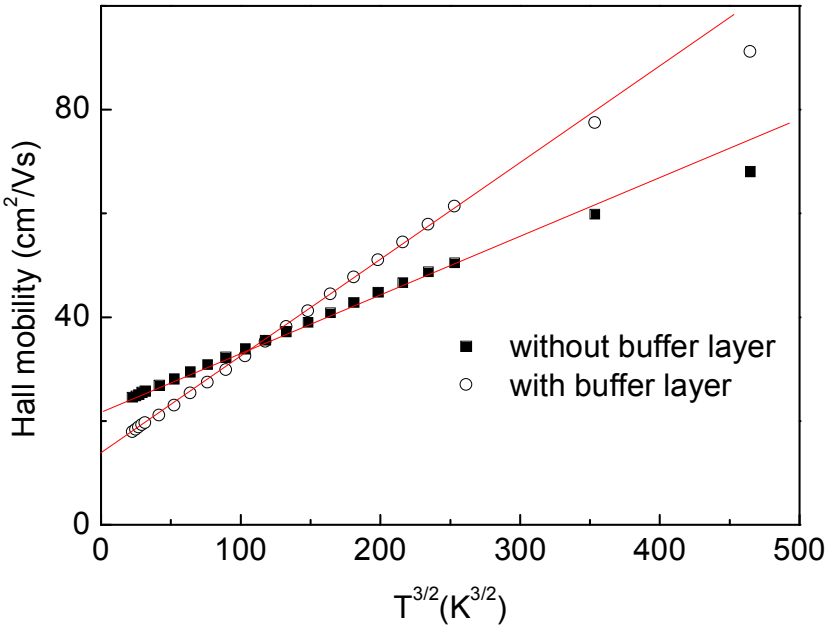

Figure 5.16 Hall mobilities with $T^{3/2}$ for 165 nm Co:TiO_2 films grown at 9×10^{-5} mbar oxygen with (solid square) and without buffer layer (open circle).

To summarize, the introduction of a TiO_2 buffer layer at the STO/Co:TiO_2 interface leads to a reduction of the density of Co clusters and a more homogeneous Co distribution in the thin film, as concluded from XRD, AFM and EFTEM measurements. Irrespective of the introduction of a buffer layer, metallic impurity band conduction and ferromagnetism are observed simultaneously, consistent with the viewpoint that metallic impurity conduction is the possible cause of carrier-mediated ferromagnetism.
However, the AHE in Co:TiO_2 films without buffer layer can be explained well by Co clusters formed at the substrate/film interface, which give rise to an anomalous transverse Hall resistivity by polarizing nearby electrons. The very small value of the ratio of the anomalous Hall resistivity to the longitudinal resistivity (10^{-4}) also confirms that the AHE originates from Co clusters. The most clear evidence for a cluster-induced AHE is, however, the observation that the AHE is strongly (if not completely) suppressed for Co:TiO_2 films with buffer layer. Structural analysis with e.g. TEM, EFTEM and AFM shows that for such films the density of Co clusters is reduced and the Co clusters form above certain critical thickness, such that they mostly appear at the surface of the films, below or in rutile outgrowths. The latter effect places a large amount of the clusters outside of the current path, such that the associated transverse scattering contribution is greatly diminished (if not completely quenched). We conclude that metallic impurity band conduction co-occurs with ferromagnetism due to Co clusters. Based on the analysis presented here, carrier mediated magnetism in Co:TiO_2 seems to be a highly unlikely scenario.

References

[1] H. Ohno, D. Chiba, F. Matsukura, T. Omiya, E. Abe, T. Dietl, Y. Ohno, and K. Ohtani, Nature **408**, 944 (2000).

[2] D. Chiba, M. Yamanouchi, F. Matsukura, and H. Ohno, Science **301**, 943 (2003).

[3] T. Dietl, H. Ohno, F. Matsukura, J. Cibert, and D. Ferrand, Science **287**, 1019 (2000).

[4] Y. Matsumoto, M. Murakami, T. Shono, T. Hasegawa, T. Fukumura, M. Kawasaki, P. Ahmet, T. Chikyow, S. Koshihara, and H. Koinuma, Science **291**, 854 (2001).

[5] H. Toyosaki, T. Fukumura, Y. Yamada, and M. Kawasaki, Appl. Phys. Lett. **86**, 182503 (2005).

[6] Y. Hirose, T. Hitosugi, Y. Furubayashi, G. Kinoda, K. Inaba, T. Shimada, and T. Hasegawa, Appl. Phys. Lett. **88**, 252508 (2006).

[7] H. Toyosaki, T. Fukumura, Y. Yamada, K. Nakajima, T. Chikyow, T. Hasegawa, H. Koinuma, and M. Kawasaki, Nat. Mater. **3**, 221 (2004).

[8] K. Ueno, T. Fukumura, H. Toyosaki, M. Nakano, and M. Kawasaki, Appl. Phys. Lett. **90**, 072103 (2007).

[9] R. Ramaneti, J. C. Lodder, and R. Jansen, Appl. Phys. Lett. **91**, 012502 (2007).

[10] Yamasaki T, Fukumura T, Yamada Y, Nakano M, Ueno K, Makino T and Kawasaki M 2009 Appl. Phys. Lett. **94** 102515 (2009).

[11] S. R. Shinde, S. B. Ogale, J. S. Higgins, H. Zheng, A. J. Millis, V. N. Kulkarni, R. Ramesh, R. L. Greene, and T. Venkatesan, Phys. Rev. Lett. **92**, 166601 (2004).

[12] S. X. Zhang, W. Yu, S. B. Ogale, S. R. Shinde, D. C. Kundaliya, W. -K. Tse, S. Y. Young, J. S. Higgins, L. G. Salamanca-Riba, M. Herrera, L. F. Fu, N. D. Browning, R. L. Greene, and T. Venkatesan, Phys. Rev. B **76**, 085323 (2007).

[13] H. Raebiger, S. Lany, and A. Zunger, Phys. Rev. Lett. **101**, 027203 (2008).

[14] J. M. D. Coey, M. Venkatesan, and C. B. Fitzgerald, Nature. Mater. **4**, 173 (2005).

[15] J.-Y. Kim, J.-H. Park, B.-G. Park, H.-J. Noh, S.-J. Noh, J. S. Yang, D.-H. Kim, S. D. Bu, T.-W. Noh, H.-J. Lin, H.-H. Hsieh, and C. T. Chen, Phys.Rev. Lett. **90**, 017401 (2003).

[16] Y. J. Lee, M. P. de Jong, and R. Jansen, Appl. Phys. Lett. **96,** 082506 (2010).

[17] A. Chambers, *Surf. Sci. Rep* **61** (2006), p. 345.

[18] R. Ramaneti, J. C. Lodder, and R. Jansen, Phys. Rev. B **76**, 195207 (2007)

[19] C. S. Hung, Phys. Rev. **79**, 727 (1950).

[20] N. F. Mott and W. D. Twose, Adv. Phys. **10**, 107 (1961).

[21] R. J. Kennedy, P. A. Stampe, E. Hu, P. Xiong, S. von Molnar, and Y. Xin, Appl. Phys. Lett. **84**, 2832 (2004).

[22] H. Fritzsche, and M. Cueevas, Phys. Rev. **119**, 1238 (1960).

[23] T. F. Rosenbaum, R. F. Miligan, M. A. Paalanen, G. A. Thomas, R. N. Bhatt, and W. Lin, Phys Rev B **27** 7509 (1983)

[24] Junichiro Inoue, and Hideo Ohno, Science **309** 2004 (2005).

[25] L. Berger, Phys. Rev. B **2**, 4559 (1970).

[26] J. Smit, Physica **24**, 39 (1958).

[27] S. Onoda, N. Sugimoto, and N. Nagaosa, Phys. Rev. Lett. **97**, 126602 (2006).

[28] T. Miyasato, N. Abe,1 T. Fujii, A. Asamitsu, S. Onoda, Y. Onose, N. Nagaosa, and Y. Tokura, Phys. Rev. Lett. **99,** 086602 (2007)

[29] T Fukumura , H Toyosaki , K Ueno, M Nakano, and M Kawasaki, New J. Phys. **10,** 055018 (2008).

[30] M. Glunk, J. Daeubler, W. Schoch, R. Sauer, and W. Limmer Phys. Rev. B **80**, 125204 (2009)

[31] D. Venkateshvaran, W. Kaiser, A. Boger, M. Althammer, M. S. R. Rao, S. T. B. Goennenwein, M. Opel, and R. Gross, Phys. Rev. B **78**, 092405 (2008)

[32] Schiemann, J., König, J., Lin, and H.-H. MacDonald, Appl. Phys. Lett. **78,** 1550 (2001).

Chapter 6

Magnetic tunnel junctions with Co:TiO_2 magnetic semiconductor electrodes

In chapter 6, spin-polarized tunneling is investigated in magnetic tunnel junctions containing an ultrathin interfacial layer of Co:TiO_2 magnetic semiconductor. Co:TiO_2 layers (0 to 10 nm thick) are inserted at the $SrTiO_3$/Co interface in $La_{0.67}Sr_{0.33}MnO_3$/$SrTiO_3$/Co tunnel junctions. The main focus is on spin transport phenomena in ultrathin layers of Co:TiO_2. We will show that the ultrathin Co:TiO_2 is a paramagnetic insulator that acts as an additional tunnel barrier, in contrast to thick (~180 nm) layers grown under comparable conditions, which exhibit metallic impurity band conduction and room-temperature ferromagnetism.

6. 1 Introduction

The reported ferromagnetism in wide band gap oxides and nitrides has been of interest in the quest for a room-temperature dilute magnetic semiconductor (DMS), which is desired for the realization of practical spintronic devices. However, the origin of the reported room-temperature ferromagnetism in transition metal doped oxide semiconductors is still quite controversial [1]. One of the consequences of carrier-mediated ferromagnetism is that the carriers should be spin polarized. Here, we aim to investigate the spin polarization of the charge carriers in anatase Co:TiO_2 via spin-polarized tunneling in a magnetic tunnel junction (MTJ). Ultrathin Co:TiO_2 layers (Co concentration 1.4%) are inserted between the $SrTiO_3$ (STO) tunnel barrier and the Co metal electrode of $La_{0.67}Sr_{0.33}MnO_3$/$SrTiO_3$/Co magnetic tunnel junctions. The epitaxial $La_{0.67}Sr_{0.33}MnO_3$ (LSMO) bottom electrode in combination with the STO barrier functions as a spin analyzer with a fixed tunnel spin polarization (TSP), allowing one to probe the TSP of the interface on the opposite side of the STO barrier containing the Co:TiO_2. This provides insight into the origin of magnetism in Co:TiO_2 and the possible role of the carriers. The Co:TiO_2 thin films were grown in the anatase phase under conditions for which room-temperature ferromagnetism, AHE and metallic impurity band conduction were previously observed [2, 3]. We investigate how the sign of the tunnel magnetoresistance (TMR) and its bias dependence change upon insertion of the Co:TiO_2 layers, and compare the results with $La_{0.67}Sr_{0.33}MnO_3$/$SrTiO_3$/Co junctions without the Co:TiO_2. Similar LSMO/STO/Co junctions have been studied previously [4] and their behavior is fairly well understood, such that they serve as a suitable reference system.

6. 2 Device fabrication and experimental methods

6. 2. 1 Deposition of the layer stacks

We have grown LSMO (8.5 nm)/STO (3.1 nm)/Co (11 nm)/Au (5 nm) heterostructures onto STO(001) single crystal substrates by pulsed-laser deposition using a stoichiometric ceramic target for LSMO and a single crystalline target for STO. The substrates were chemically treated and annealed at 950 ^{o}C to obtain a TiO_2 termination [5]. Perovskites were grown at 750 ^{o}C and 1 Hz laser repetition rate under O_2 pressures of 0.35 mbar and 0.30 mbar, respectively, for LSMO and STO. After deposition of the STO barrier, the O_2 pressure was increased to 1 bar and kept at this value during cooling to room temperature, in order to obtain proper O content. Metal Co counter electrodes and Au capping layers were deposited at room temperature without O_2 gas present. Junctions fabricated according to this process are referred to as "standard junctions".

To study the tunnel spin polarization of STO/Co:TiO_2 interfaces, a series of MTJ structures was fabricated with ultrathin Co:TiO_2 films deposited onto the STO tunnel barriers. Since the growth conditions for ferromagnetic Co:TiO_2 (*i.e.* 9×10^{-5} mbar O_2 and substrate temperature of 550 ^{o}C) are radically different from the conditions used to grow the LSMO and STO perovskites, we adopted the following procedure. After growth of the STO tunnel barrier, the samples were cooled to room temperature in 1 bar O_2 as described above. Then, the layer stack was heated again to 550 ^{o}C in 9×10^{-5} mbar O_2 for the Co:TiO_2 deposition, followed by cooling to room temperature in the same 9×10^{-5} mbar O_2 pressure, and deposition of the Co and Au metals at room temperature. These conditions avoid having a high oxygen content in the Co:TiO_2 layer, which would lead to insulating behavior and loss of room-temperature ferromagnetism [3]. However, the process may lead to oxygen deficiency in the STO barrier (and in the underlying LSMO), which is known to affect the TMR of the structures [4]. Therefore, we also fabricated reference LSMO/STO/Co MTJs without the insertion of Co:TiO_2, but going through the same process as for the junction with Co:TiO_2. That is, these junctions were heated to 550 ^{o}C at 9×10^{-5} mbar O_2 for the exact same time as is required for Co:TiO_2 deposition, but without depositing any Co:TiO_2. Such samples will be referred to as "reference junctions" and are expected to have the same oxygen content in the STO barrier as junctions with the Co:TiO_2.

6. 2. 2 Photolithographic processing

Standard UV lithography is employed to define junctions with circular active areas of 150, 100, and 50 μm diameter. Each MTJ structure also comprises two rectangular reference electrodes (with a substantially larger area) such that electrical characteristics of the active junction area can be probed in a three-terminal measurement geometry (see also Figure 6.1).

The fabrication process, except for the definition of contact pads/leads, is described in Figure 6.2. The first step is to define active (B) and reference contact electrodes (E) by selective wet etching of the Au/Co layers using photolithography. The sample is coated by a layer of UV-sensitive photoresist, followed by exposure to UV light through a photomask, and subsequently developed to form the desired pattern on the surface. A

standard gold etching solution is prepared by dissolving 34g of KI and 4.5g of I_2 into a mixture of 150ml of glycerol and 300ml of DI water. This solution also etches Co, although at a much lower rate than Au. Consequently, some over-etching (sideways) of Au always occurs, which is however not critical for device operation. Before etching, samples are baked at 120 ^{o}C for 10 minutes in order to prevent the over-etching of Au relative to Co. The samples are etched first to remove the Au capping layer of about 10nm thick (and some of the Co layer beneath) for a very short time (10sec). Then, the samples are baked again at 120 ^{o}C for 1 minute. This causes the photoresist layer to flow out somewhat, such that it covers the over-etched part and thereby prevents further over-etching of Au. Finally, the samples are again dipped into the concentrated Au etching solution for several minutes to remove the remaining Co. The over-etched area, where Au is removed, looks less bright compared to the remaining Au in the optical microscopy image in Figure 6.3, taken after the ion beam etching process.

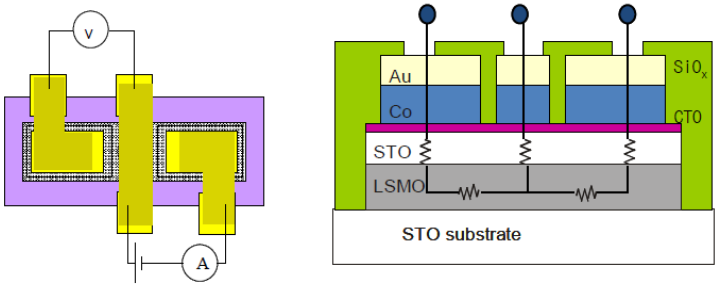

Figure 6.1 Schematic illustration of top (left) and cross-sectional view (right) of the MTJ device.

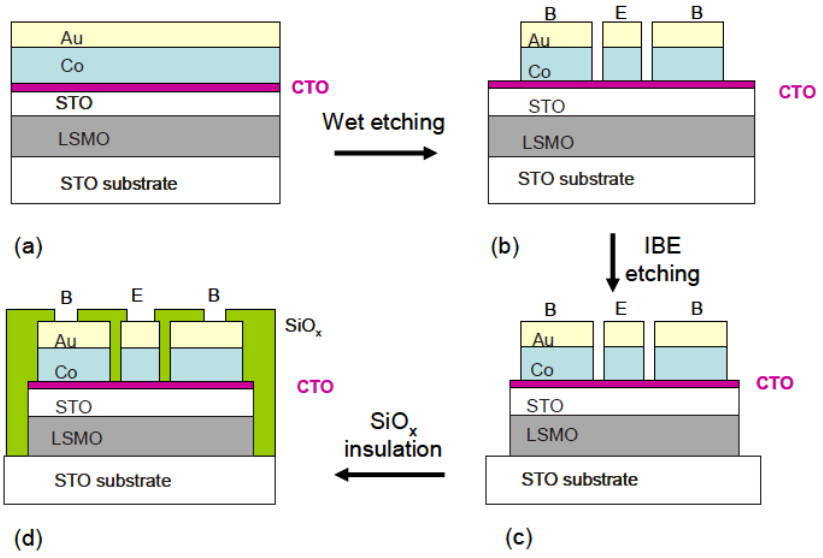

Figure 6.2 Schematic illustration of the MTJ fabrication processing steps. (a, b) The deposited Au/Co is etched to define reference (B) and active (E) contact electrodes. (c) Device isolation is done by ion beam etching (IBE). (d) SiO_x deposition is carried out for electrical isolation of the structures before depositing Au contact pads.

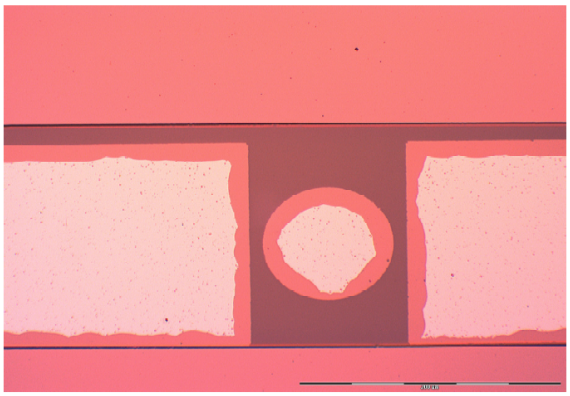

Figure 6.3 Optical microscopy image of a MTJ with 150μm diameter active area after ion beam etching.

Next, ion beam etching (IBE) is performed to etch through the STO and LSMO layers, in order to electrically isolate individual MTJs from each other on the chip (Figure 6.2 (c)). We use an Oxford Ion Fab 300, equipped with a secondary ion mass spectrometry (SIMS) detector and a sample holder featuring cooling. A beam of highly energetic Ar atoms impinge upon the sample to sputter material out from the surface, while the sputtering materials are monitored by the SIMS detector. Figure 6.4 shows a SIMS profile recorded during ion beam etching of an MTJ. The IBE is performed at two angles (between the ion beam and the sample normal), 20 degrees (for 7 minutes) and 75 degrees (for 1 minute). These angles produce a unidirectional etching profile without re-deposition of any sputtered materials at the edges. The photoresist is stripped-off by putting the sample in an ultrasonic bath of acetone for 1 hour, since photoresist that is damaged by ion bombardment takes quite long to remove.

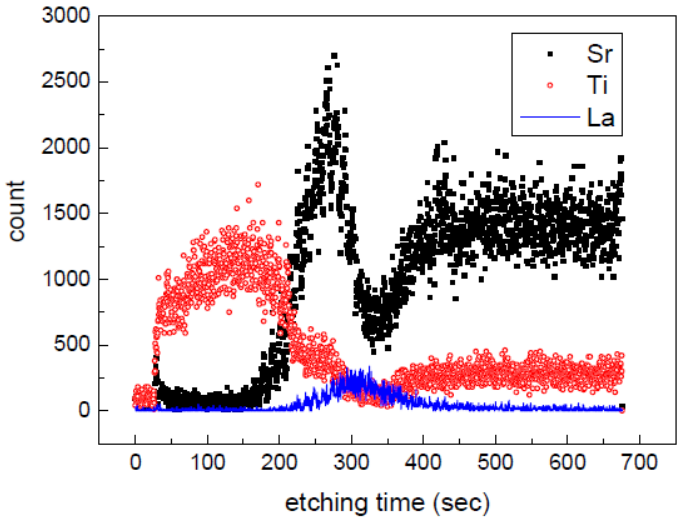

Figure 6.4 SIMS profile for ion beam etching of MTJ stacks with 5 rpm, rotating sample speed and 20 degree, the angle between beam and the normal to the sample surface. Sr, Ti and La are monitored. MTJ stacks consist of STO(substrate)/LSMO(8.5nm)/STO(3nm)/Co:TiO_2(10nm).

Subsequently, an about 200nm thick SiO_x insulation layer is deposited by RF sputtering onto a negative photoresist pattern for a photolithographic lift-off process shown in Figure 6.5. The Au contacts remain exposed, such that they can be electrically contacted in the next fabrication step. In the lift-off process, SiO_x is deposited everywhere, i.e. covering the areas with photoresist and without photoresist. In this pattern, only the Au contacts are covered with photoresist (see Figure 6.5) Therefore, when the SiO_x-covered sample is put in acetone, the photoresist dissolves away with the film on it. This leads to a SiO_x coating everywhere, except on top of the Au contacts, as shown in figure 5.1 (d). The insulation plays the role of avoiding any electrical shorts between the Au/Cr contact leads/pads (formed in the next fabrication step) and LSMO at the side walls of the MTJ stacks, which are exposed upon ion beam etching.

SiO_x is deposited by radio frequency (RF) sputtering from a SiO_x target. This process turned out to be critical for obtaining a high device yield. Proximity to the plasma extending from the sputter target leads to MTJ failure. Therefore, off-axis sputtering or sputtering with a long distance between the target and the sample is desirable for SiO_x deposition. Moreover, the adhesion between SiO_x and substrate depends strongly on the temperature and oxygen background pressure during deposition. Initially, SiO_x deposition was carried out using a mixture of argon and oxygen as sputtering gasses, in order to improve the insulating quality of the SiO_x layers. Films prepared under these conditions, however, exhibit rather poor adhesion to the substrate, such that strip-off easily occurs. Figure 6.6 shows the detrimental effects due to strip-off of SiO_x layers during lift-off. A strongly improved adhesion is obtained in absence of oxygen flow to the deposition chamber during sputtering. The insulating properties of these oxygen deficient SiO_x layers were checked using a probe station. It was found that they show good insulating behavior in spite of the oxygen deficiency.

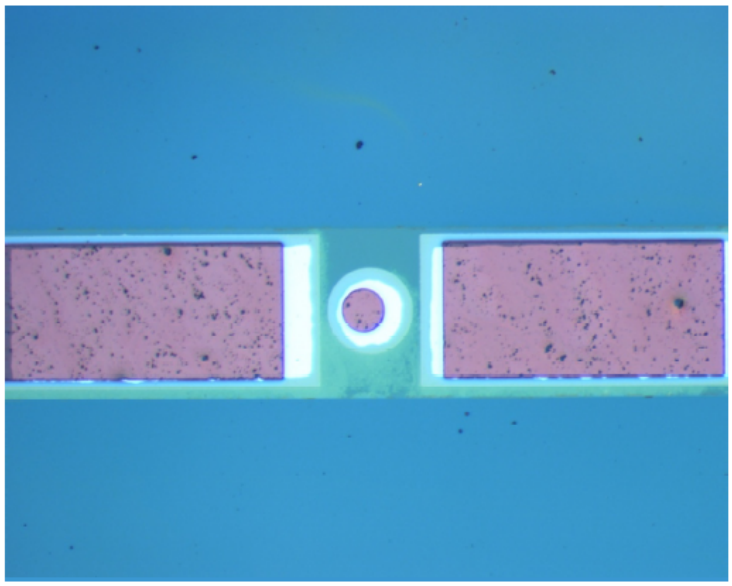

Figure 6.5 Optical microscopy image of a MTJ with a 100μm diameter active area, after patterning the negative photoresist layer used for lift-off of the SiO_x insulating layer.

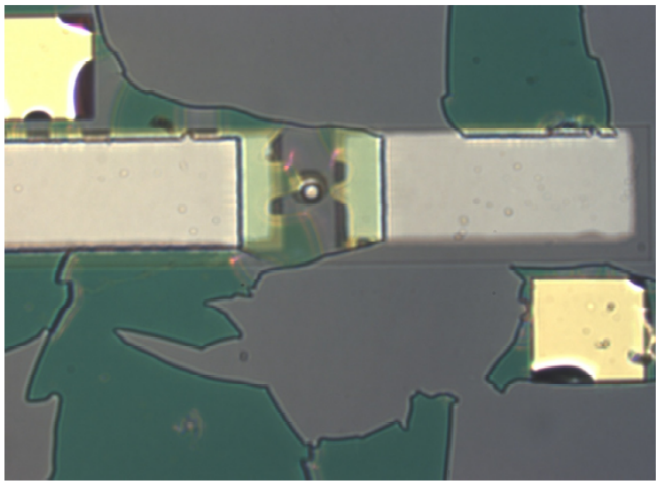

Figure 6.6 Optical microscopy image of a MTJ with strip-off of the SiO_x insulating layer after several lift-off steps.

The fabrication of bond pads for wire bonding to device cartridges and contact leads to the electrodes of the MTJs is carried out in two photolithographic steps, both involving a lift-off process. In order to enhance the adhesion of Au bond pads to the oxide substrate, an adhesion layer, typically Cr, is deposited first. Cr forms an oxide at the interface, and mixes further with Au. However, if Cr is deposited onto exposed Co, which is indeed partially exposed due to over-etching of the Au cap, alloying occurs which is detrimental for the operation of the MTJs. Therefore, we first define square contact pads for wire bonding by sputter deposition and lift-off of a Cr/Au bilayer, and subsequently connect these bond pads to the electrodes of the MTJs by sputter deposition and lift-off of Au contact leads. Figure 6.7 shows an optical microscope image of an MTJ device after final processing, ready for electrical measurements.

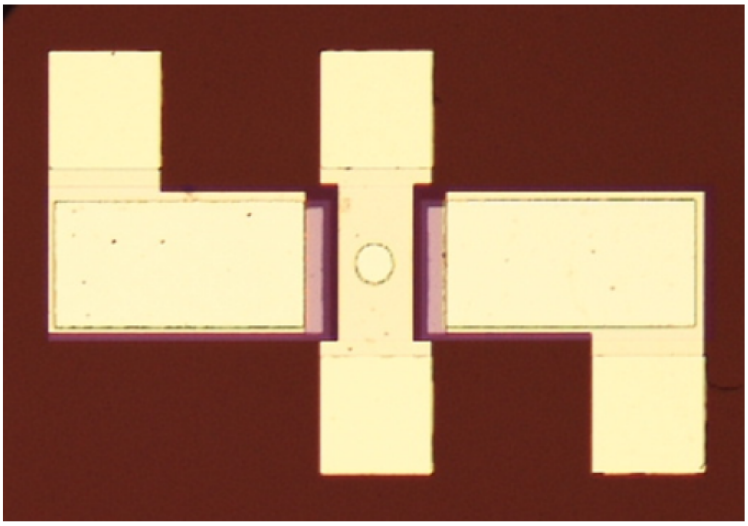

Figure 6.7 Optical microscope image of an MTJ with 100μm diameter active area after final processing.

6. 2. 3 Electronic characterization

DC current-voltage measurements were carried out in a four-point cross geometry depicted in Figure 6.1. The voltage source is applied across the reference junction B and the active junction E, giving rise to the tunneling current across the two junctions B and E. Then, the voltage is measured across the active junction E & the other reference junction B. Since no current flows through the latter, the measured voltage is entirely due to the potential drop over the active contact. In all measurements for all MTJs, a positive bias means that E is at a higher potential, which in turn means that Co is at a higher potential compared to LSMO.

Tunnel magnetoresistance (TMR) measurements are performed in magnetic fields up to 1 T. The TMR ratio is defined as $(R_{ap}-R_p)/R_p$, where R_p and R_{ap} are the junction resistances for parallel and anti-parallel magnetization of the two electrodes, respectively. For all results presented here, the condition is satisfied that the junction resistance is at least 10 times the electrode square resistance [6].

The measurements were performed in the temperature range between 10K and 300K, using either a liquid helium flow cryostat or a closed cycle He gas cooler.

6. 3 Results and discussion

Before we address the device characteristics, we briefly discuss the structural properties of the MTJ stacks. Figure 6.8 shows a high resolution transmission electron microscope image of the cross section of a layer stack STO(substrate)/LSMO/STO/Co:TiO_2/Co. The image shows the epitaxial nature of the various layers (except Co) and the sharp interfaces between them. The HR-TEM image has been also used to calibrate the thickness of the different layers. A point of concern is Co segregation and cluster formation, which would lead to spurious effects in the MTJ characteristics. Figure 6.9 shows an EFTEM image of the same structure, where the different elements in the layer stack are color-coded. We note that in this measurement, Co segregation is not observed within the Co:TiO_2 film. However, considering that the detection limit of EFTEM is about 5%, Co signals below that limit, e.g. originating from very small clusters, cannot be discerned in the image. This means that the existence of Co segregation cannot be excluded based on the EFTEM analysis alone, in fact we have observed evidence for metallic Co in 10nm films as discussed in Chapter 4. Partially due to this complication, we focused mostly on MTJs with Co:TiO_2 layers considerably thinner than 10 nm (i.e. $\leq$2nm).

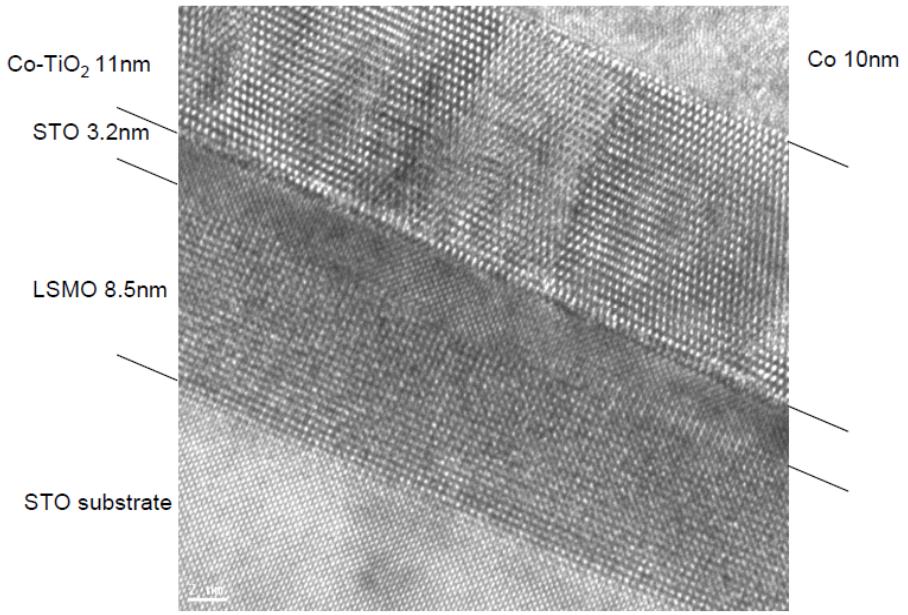

Figure 6.8 High resolution cross-sectional transmission electron microscope (TEM) image of STO(substrate)/LSMO/STO/Co:TiO_2/Co layer stack

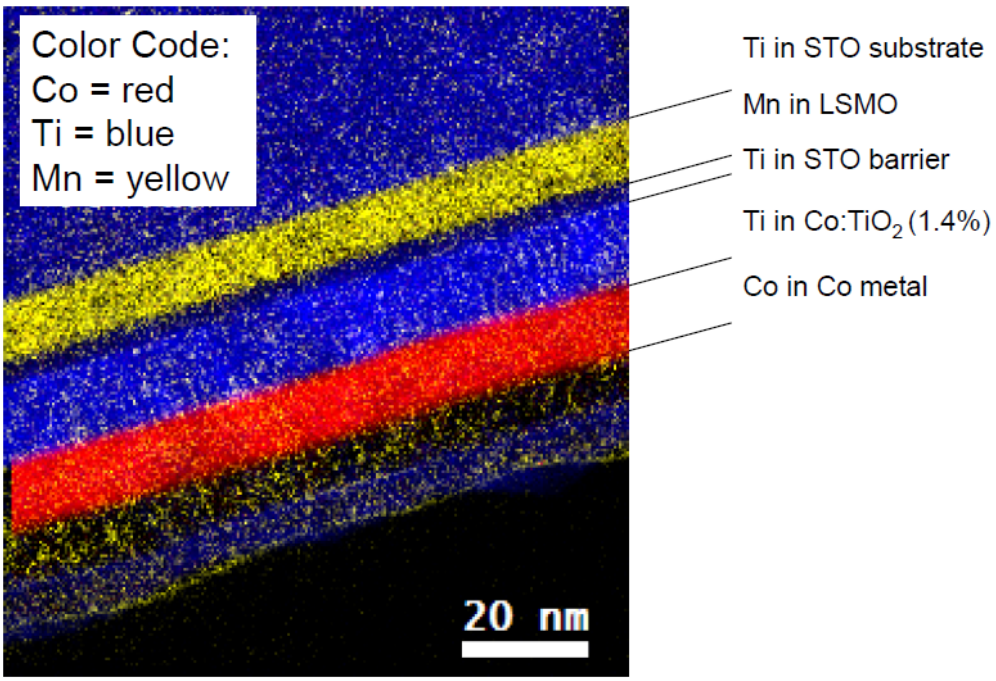

Figure 6.9 Energy filtered transmission electron microscope (EF-TEM) image of STO(substrate)/LSMO/STO/Co:TiO_2/Co layer stack. The image represents maps of the concentration of elemental Mn (in yellow), Ti (in blue), and Co (in red).

Figure 6.10 shows the variation of the TMR in the standard junction (STO(substrate)/LSMO/STO/Co) with bias voltage. The TMR is negative and asymmetric with respect to bias polarity, with a maximum TMR (absolute value) of about 20% at +300mV, and vanishing TMR for high negative bias. These results are similar to that described in previous reports [4,7]. The negative TMR is indicative of a negative tunneling spin polarization at the STO/Co interface [4,7], i.e. a higher tunnel transmission probability for minority electrons. In a very crude picture, the bias dependence of the TMR can be explained by the relative position of the DOS of Co (majority and minority *d* bands) and LSMO (majority Mn-derived *d* band) as a function of bias in Figure 6.11. Here, it is assumed that LSMO behaves as a true half metal (which is indeed a valid assumption for low temperatures [Park, J.H.; Vescovo, E.; Kim, H.J.; Kwon, C.; Ramesh, R.; Venkatesan, T.; Nature, 392 (1998) 794]), such that additional contributions involving the LSMO minority band can be neglected. According to this picture, we can expect that the negative TMR (high current for anti-aligned magnetization directions) is maximum at 400mV (Fig. 6.11 (b)), since at that bias the Fermi level of LSMO is aligned with the maximum in the minority DOS of the *d* band in Co, such that a high current is expected for the anti-parallel configuration of the magnetizations. For negative bias (Fig. 6.11 (c)), the current in the anti-parallel configuration is expected to be lower, since the tunneling electrons originate from Co-states close to E_F, away from the maximum in the minority *d* band. On the other hand, tunneling from states close to the maximum in the majority *d*-band becomes possible at negative bias, leading to an increased tunnel current in the parallel configuration. Hence, the negative TMR is suppressed, and the sign of the TMR may even reverse when the current for the parallel configuration exceeds that for the anti-parallel configuration. Our sample indeed exhibits a broad maximum in the negative TMR at positive bias, consistent with the argumentation above, but does not show a sign change of the TMR. We emphasize, however, that this argumentation strongly oversimplifies the actual processes involved, since it only considers tunneling involving the (bulk) Co *d* bands and the Mn-derived majority *d* band of LSMO. Moreover, it does not take into account the fact that the tunneling electrons always originate from a relatively narrow energy window close to E_F, since deeper-lying levels encounter a larger effective barrier height.

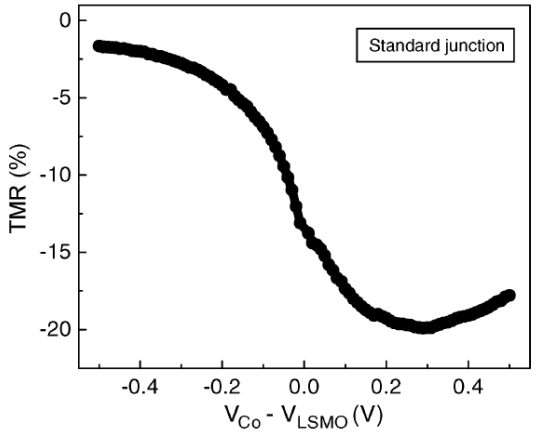

Figure 6.10 TMR versus bias voltage for a standard LSMO/STO/Co magnetic tunnel junction at 10K. Positive bias corresponds to electrons tunneling from the LSMO into the Co.

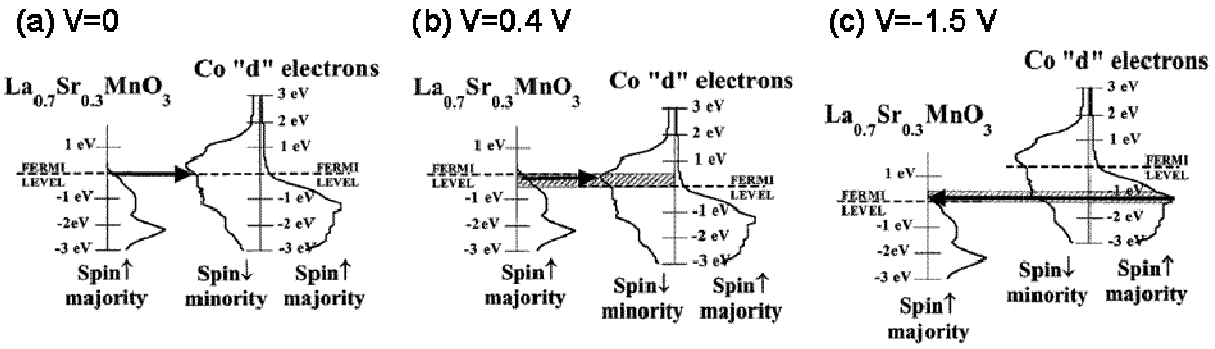

Figure 6.11 Relative positions of the d DOS in Co and LSMO for (a) a bias around zero, (b) a positive bias of 0.4 V, and (c) a negative bias of -1.15 V [7].

Figure 6.12 shows the dependence of the resistance R_p of the standard junction on temperature (T). The resistance has a maximum at about 260 K and decreases at low temperature. Such temperature dependence was also observed in similar structures [4,8], and is usually attributed to a reduced effective ordering temperature of the LSMO, accompanied by a metal-insulator transition, at the LSMO/STO interface [9]. The metal-insulator transition is accompanied by a gradual reduction of the DOS at E_F,[10-12] which leads to a reduced tunnel transmission probability and thus a higher resistance at higher temperatures. The maximum in the resistance must stem from a different mechanism, most likely thermally activated, defect assisted tunneling. Indeed, as we will show below, for oxygen deficient STO barriers, containing a large amount of defect states in the gap, a strongly increasing resistance is observed as the temperature is decreased.

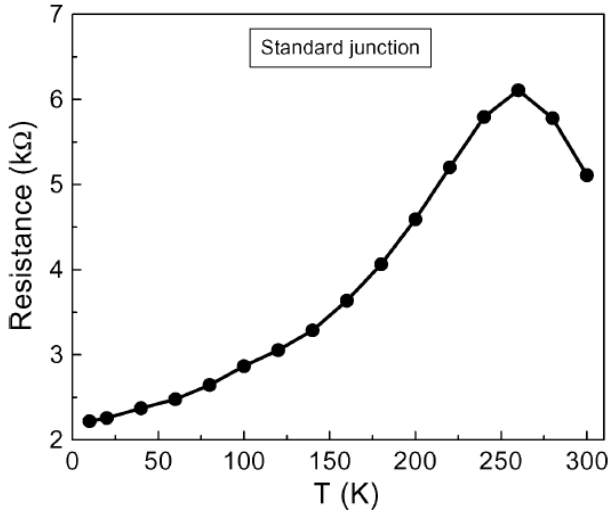

Figure 6.12 Tunnel resistance versus temperature T for a standard LSMO/STO/Co magnetic tunnel junction with parallel magnetization configuration and +100mV bias.

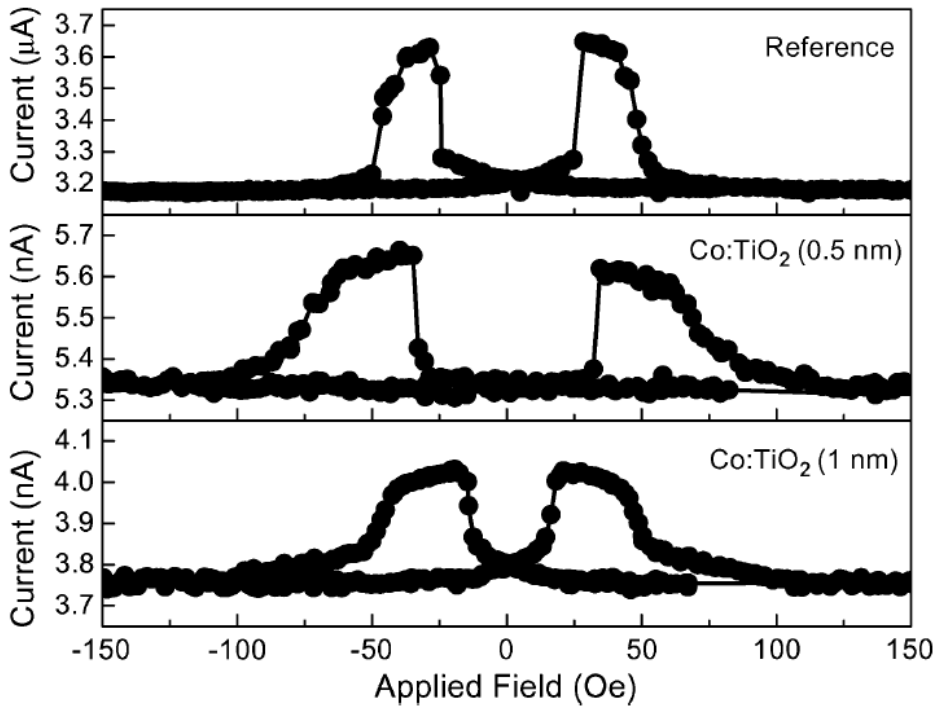

Figure 6.13 Tunnel current versus applied magnetic field for the LSMO/STO/Co reference junction (top panel), a LSMO/STO/Co MTJ with 0.5 nm of Co:TiO_2 inserted at the STO/Co interface (middle panel), and a LSMO/STO/Co junction with 1.0 nm of Co:TiO_2 inserted at the STO/Co interface (bottom panel). All data taken at 10 K and for +100 mV bias.

Next, we studied the effect of Co:TiO_2 insertion on the MTJ characteristics, for junctions with, respectively, 0.5, 1, and 2 nm Co:TiO_2 added between STO and Co. As shown in figure 6.13, a sizeable and negative TMR is observed for MTJs with 0.5 nm and 1 nm Co:TiO_2 inserted, and also for the reference junction (Co:TiO_2 deposition conditions mimicked but no Co:TiO_2 deposited). In contrast, a finite TMR for MTJs with 2 nm Co:TiO_2 is not observed. Figure 6.14 shows the bias dependence of the TMR. All junctions show an asymmetric bias dependence as for the standard junction, but with different TMR maxima: at +50 mV (+40 mV) for MTJs with 0.5 nm (1 nm) Co:TiO_2 inserted, and at +150 mV for the reference MTJ. Moreover, the TMR decreases rapidly with bias beyond the maximum, which is similar to the behavior of LSMO/STO/Co junctions with oxygen deficient barriers [4]. In contrast, standard LSMO/STO/Co MTJs feature a broad maximum at +300 mV, with a slow decay of the TMR as the bias voltage is increased to higher positive values (see Figure 6.10). For the junctions with Co:TiO_2, the magnitude of the TMR is significantly smaller as compared to that of the reference junction, and the TMR maximum becomes more narrow and shifts toward zero bias. In addition, the junction resistance increases significantly upon insertion of the 1nm (2nm) Co:TiO_2 by about 3 (5) orders of magnitude at 10 K (see figure 6.15). We can exclude that this is solely due to the loss of oxygen in the perovskites (i.e. the STO tunnel barrier and LSMO electrode), as this should also be present for the reference junction. Comparing Figure 6.12 and Figure 6.15, we observe that the reference junction has an

order of magnitude higher junction resistance in comparison with the standard MTJ. This difference is attributed to the change in oxygen content of the STO barrier and LSMO due to heating of the structure to 550 ^{o}C under oxygen poor conditions (9×10^{-5} mbar).

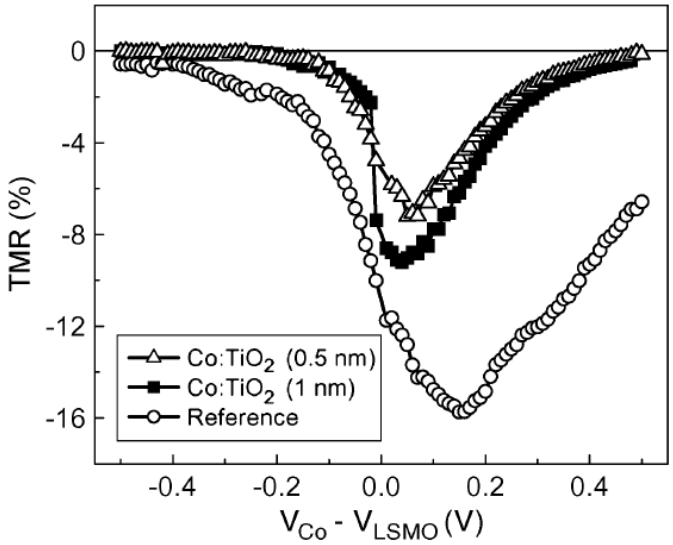

Figure 6.14 TMR versus bias for the reference junction (circles), an MTJ with 0.5 nm of Co:TiO_2 inserted (triangles), and an MTJ with 1 nm of Co:TiO_2 inserted (squares). All data were taken at 10 K.

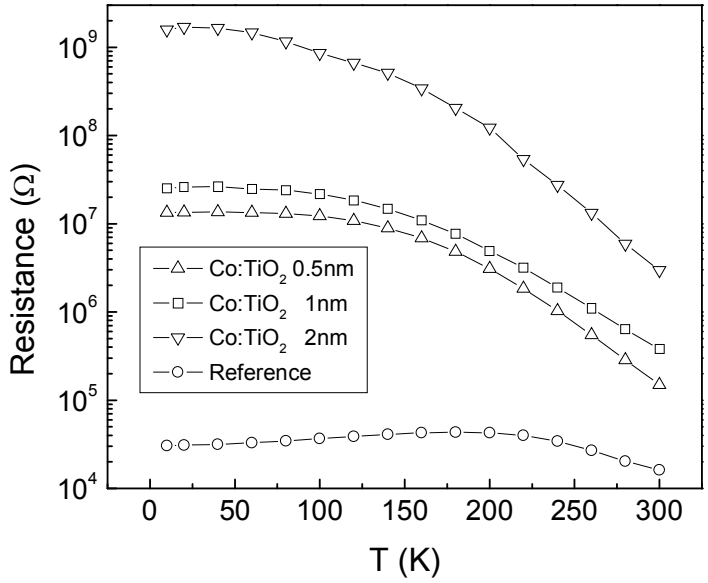

Figure 6.15 Tunnel resistance versus temperature T with parallel magnetization configuration and +100 mV bias for the reference junction (circles), an MTJ with 0.5 nm of Co:TiO_2 inserted (triangles), an MTJ with 1 nm of Co:TiO_2 inserted (squares), and an MTJ with 2 nm of Co:TiO_2 inserted (inverse triangles).

The strong increase of the junction resistance upon insertion of the Co:TiO_2, accompanied by a decrease of the TMR, provides some clues about the electronic and magnetic properties of the ultrathin Co:TiO_2 films. The higher junction resistance suggests an increased effective barrier thickness, which in turn points to insulating behavior of the inserted Co:TiO_2 layers. This is somewhat surprising since thicker films of Co:TiO_2 (~180 nm), grown under comparable conditions (550 ^{o}C at 7×10^{-5} mbar O_2) on STO substrates, exhibit metallic impurity band conduction and are (semi-)conducting with a carrier density of $5x10^{18}$ cm^{-3} and mobility of about 20 cm^2/Vs at room temperature, and resistivity of the order of 0.1 Ωcm in the range between 10 and 300 K [3]. Hence, it was expected that the inserted Co:TiO_2 would become part of the electrode, rather than act as a tunnel barrier. An ultrathin film of only a nm thick (the unit cell of anatase Co:TiO_2 along the c-axis growth direction is ~0.95 nm) may have different electronic properties and behave as a 2 dimensional system which does not exhibit impurity band formation under these growth conditions. Alternatively, the film properties may be affected by the contact with the metal Co electrode on top of it. For instance, this may lead to carrier depletion in the Co:TiO_2, leaving it insulating.

If the Co:TiO_2 is indeed insulating and acts as an additional tunnel barrier, the tunneling electrons, and the associated negative TMR, originate from the Co metal at the interface with the Co:TiO_2. Since thick, more resistive Co:TiO_2 films grown under oxygen rich conditions are found to be paramagnetic at room temperature [3], the reduced TMR is also readily explained. The spin-polarized tunneling electrons originating from the Co would then experience spin-flip scattering by paramagnetic Co ions present in the Co:TiO_2 part of the tunnel barrier, which is known [13,14] to reduce the TMR.

To exclude spin polarized tunneling due to electrons originating from ferromagnetic Co, MTJs comprising LSMO/STO/Co:TiO_2(2.0nm)/Au, without any Co layer, were fabricated. Considering the fact that even 10 nm Co:TiO_2 films exhibit heterogeneity of Co in the film [15], MTJs containing Co:TiO_2 layers with a thickness considerably below 10nm (e.g. 2nm) without Co layer were fabricated. In all cases (we checked 41 MTJs), we do not observe a finite TMR. Similar to the 2 nm Co:TiO_2 junctions *with* Co layers, these devices exhibited very high resistance (on the order of MΩ at room temperature), and a similar dependence of this resistance on temperature (see Figure 6.16).

For all devices comprising Co:TiO_2 layers, with or without ferromagnetic Co layers, we observe a strong increase of the resistance consistent with Co:TiO_2 acting as a tunnel barrier rather than a metallic contact. This explains the reduced TMR for junctions containing Co electrodes, and the absence of TMR when Co is replaced by Au. Possible explanations for the insulating behavior of the thin (≤2nm) Co:TiO_2 films were already given above.

Since Co:TiO_2 is in contact with Au, the carriers from Co:TiO_2 layer is depleted due to the difference in their work functions and thus the 2.0nm Co:TiO_2 layer acts as an additional tunnel barrier such that all the tunneling electrons would come from Au and Co:TiO_2 interface. If Co:TiO_2 is real carrier mediated dilute semiconductor, there is a possibility that it does not have enough carriers to establish long range ferromagnetic order. It might also be possible that the 2.0nm Co:TiO_2 film (~2 unit cell) has its Curie temperature so small that ferromagnetic order disappears at 10 K.

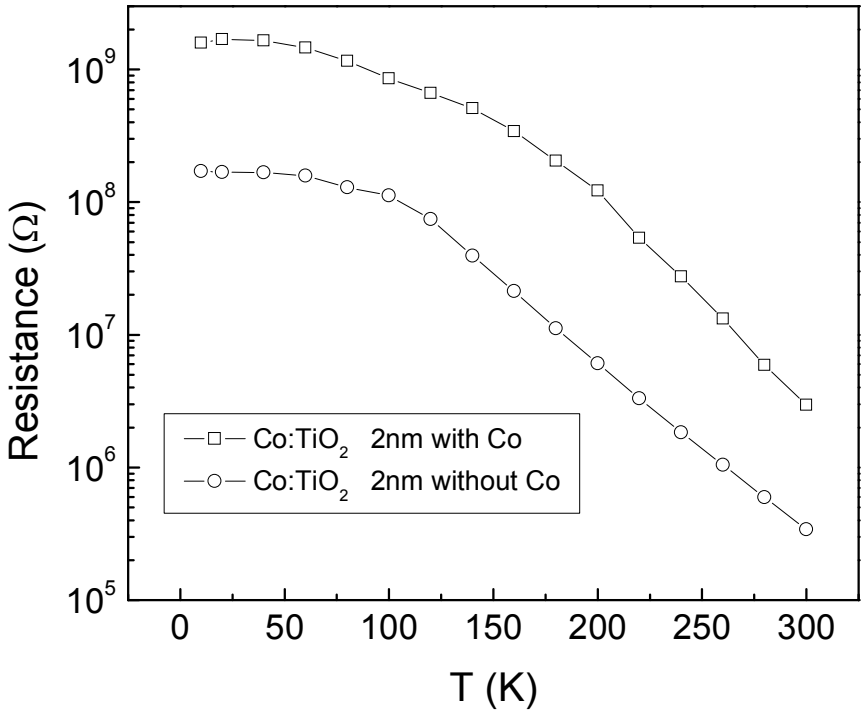

Figure 6.16 Tunnel resistance versus temperature T with parallel magnetization configuration and +100 mV bias for an MTJ containing 2 nm of $Co:TiO_2$ inserted with (squares) and without Co (circles).

6.4 Conclusion

It is found that the TMR and junction resistance of epitaxial LSMO/STO/Co magnetic tunnel junctions changes significantly upon the insertion of ultrathin layers of $Co:TiO_2$ magnetic semiconductor at the STO/Co interface. The magnitude of the TMR decreases but remains negative, while the junction resistance increases strongly. This is consistent with an effectively insulating and paramagnetic $Co:TiO_2$ adding to the tunnel barrier, with the tunneling electrons originating mostly from the $Co:TiO_2$/Co interface, and experiencing spin-flip scattering by paramagnetic Co in the $Co:TiO_2$. Because the properties of the ultrathin $Co:TiO_2$ in contact with a metal Co electrode appear different from thicker films grown under similar conditions, the experiments unfortunately do not confirm or rule out a finite spin polarization of carriers in thicker $Co:TiO_2$ films.

REFERENCES

1. S.A. Chambers, "Ferromagnetism in doped thin-film oxide and nitride semiconductors and dielectrics," Surf. Sci. Rep. **61** (2006), p. 345.

2. R. Ramaneti, J. C. Lodder, and R. Jansen, "Anomalous Hall effect in anatase Co:TiO_2 ferromagnetic semiconductor," Appl. Phys. Lett. **91**, 012502 (2007).

3. R. Ramaneti, J. C. Lodder, and R. Jansen, "Kondo effect and impurity band conduction in Co:TiO_2 magnetic semiconductor," Phys. Rev. B **76**, 195207 (2007).

4. I. J. Vera Marún, F. M. Postma, J. C. Lodder, and R. Jansen, "Tunneling magnetoresistance with positive and negative sign in $La_{0.67}Sr_{0.33}MnO_3/SrTiO_3$/Co junctions," Phys. Rev. B **76**, 064426 (2007).

5. G. Koster, B. L. Kropman, G. J. H. M. Rijnders, D. H. A. Blank, and H. Rogalla, "Quasi-ideal strontium titanate crystal surfaces through formation of strontium hydroxide," Appl. Phys. Lett. **73**, 2920 (1998).

6. J. S. Moodera, L. R. Kinder, J. Nowak, P. LeClair, and R. Meservey, "Geometrically enhanced magnetoresistance in ferromagnet–insulator–ferromagnet tunnel junctions," Appl. Phys. Lett. **69**, 708 (1996).

7. J. M. De Teresa, A. Barthelemy, A. Fert, J. P. Contour, R. Lyonnet, F. Montaigne, P. Seneor, and A. Vaures, "Inverse Tunnel Magnetoresistance in Co/$SrTiO_3$/$La_{0.7}Sr_{0.3}MnO_3$: New Ideas on Spin-Polarized Tunneling," Phys. Rev. Lett. **82**, 4288 (1999).

8. J. Z. Sun, K. P. Roche, and S. S. P. Parkin, "Interface stability in hybrid metal-oxide magnetic trilayer junctions," Phys. Rev. B **61**, 11244 (2000).

9. M. Viret, M. Drouet, J. Nassar, J. P. Contour, C. Fermon, and A. Fert, "Low-field colossal magnetoresistance in manganite tunnel spin valves," Europhys. Lett. **39**, 545 (1997).

10. R. Bertacco, A. Tagliaferri, M. Riva, L. Signorini, M. Cantoni, A. Cattoni, F. Ciccacci, B. A. Davidson, F. Maccherozzi, I. Vobornik, and G. Panaccione Phys. Rev. B **78**, 035448 (2008)

11. Park, J.H., Vescovo, E., Kim, H.J., Kwon, C., Ramesh, R., Venkatesan, T, Nature, **392** (1998) 794

12. D. D. Sarma, N. Shanthi, S. R. Krishnakumar, T. Saitoh, T. Mizokawa, A. Sekiyama, K. Kobayashi, A. Fujimori, E. Weschke, R. Meier, G. Kaindl, Y. Takeda, and M. Takano, Phys. Rev. B **53**, 6873 (1996)

13. R. Jansen and J.S. Moodera, "Influence of barrier impurities on the magnetoresistance in ferromagnetic tunnel junctions," J. Appl. Phys. 83, 6682 (1998).

14. R. Jansen and J.S. Moodera, "Magnetoresistance in doped magnetic tunnel junctions: Effect of spin scattering and impurity-assisted transport," Phys. Rev. B 61, 9047 (2000).

15. Y. J. Lee, M. P. de Jomg, R. Jansen, Appl. Phys. Lett. **96,** 082506 (2010)

Chapter 7

Conclusions

The aim of this thesis is to unravel the current puzzle of the origin of ferromagnetism in anatase Co:TiO_2. In the beginning of the new millennium, the discovery of room temperature ferromagnetism in anatase Co:TiO_2 casted the possibility of the realization of practical spintronic devices. However, a large number of conflicting results have pointed toward both an intrinsic and extrinsic origin for ferromagnetism during the last decade. The reason for this controversy can for a large part be attributed to imprudent conclusions relying on measuring magnetism without careful structural study of secondary phases in the materials under investigation. Most of the reports on an intrinsic origin of ferromagnetism in anatase Co:TiO_2 were explained in terms of the existence of the anomalous Hall effect (AHE) [1]. However, later reports suggesting that metallic clusters were observed along with AHE [2, 3] have aggravated the mystery of the origin of ferromagnetism. In this thesis, we approach the current mystery with a broad set of complementary techniques containing structural probes, spectroscopy, and transport characterization together. Previously, common approaches for detecting clusters in dilute magnetic semiconductor (DMS) research are x-ray diffraction (XRD) and transmission electron microscopy (TEM). Here, we attack the problem with more element sensitive characterization methods focusing on the detection of secondary phases.

First, synchrotron based x-ray techniques such as x-ray absorption spectroscopy (XAS) and x-ray circular magnetic dichroism (XMCD) were employed. These techniques have their strengths in providing element specific information on the electronic and magnetic properties of materials. Chapter 4 mainly discusses the results from XAS and XMCD. The main conclusion is that the Co distribution is heterogeneous for all Co:TiO_2 films grown under oxygen rich as well as oxygen poor conditions. Previous reports have suggested that the existence of Co *L*-edge fine structure in XAS is the evidence for Co ionic states and thus the incorporation of Co ions in substitutional positions of the host lattice. However, there is still a possibility that a featureless Co metallic contribution is screened by the ionic fine structure. The results contained in Chapter 4 show that a suppressed, somewhat smeared-out XAS multiplet structure in oxygen poor samples, similar to previous reports in the literature, is related to a featureless Co metal contribution superimposed on the spectral features related to Co^{2+} ions. A Co metal contribution is confirmed by XMCD measurements, which show a featureless dichroism spectrum characteristic of metallic Co. Similar metallic XMCD spectra were observed for oxygen rich films, exhibiting paramagnetic behavior, and ferromagnetic oxygen poor films. These findings clearly show that measurements of XAS *L*-edges alone may confirm the presence of ionic species, but cannot rule out secondary phases that may not yield a discernable fingerprint. In this sense, XMCD is a useful tool to check for heterogeneity in DMS research.

Energy filtered TEM (EFTEM) analysis is also employed to substantiate the XAS/XMCD measurements via elemental (in particular Co) mapping. In particular

EFTEM proved its validity for detecting tiny Co clusters near the surface in Co:TiO_2 films grown under oxygen rich conditions, while they are hardly discernable in the high resolution TEM images. In contrast, relatively large Co-rich clusters were observed, emanating from the substrate/film interface and spanning the full film thickness, for Co:TiO_2 thin films grown under oxygen poor conditions.

Along with the above results that show that Co segregates to defects sites to form clusters, strong charge transfer (CT) satellite peaks at Co *L* edges were observed for the thickest (160 nm) oxygen poor films, while thinner films showed much weaker satellites. The CT peaks can be explained by the interaction of Co (3*d*) electrons with donor defect states in the band gap. CT peaks become stronger for thicker films with a higher defect density, which may result in defect states that are more energetically close to and significantly hybridized with the Co(3*d*) states. These findings also confirm that the electronic structure of Co *ions* is heterogeneous, related to defect states in Co:TiO_2 thin films.

Chapter 5 mainly discusses the effect of improving the homogeneity of the Co distribution on the magnetic and transport properties, by the introduction of a TiO_2 buffer layer at the STO/Co:TiO_2 interface. The introduction of a buffer layer leads to a reduction of the density of Co clusters and a more homogeneous Co distribution in the thin films, as confirmed by XRD, AFM and EFTEM measurements. For Co:TiO_2 films with buffer layer, the density of Co clusters is reduced and the Co clusters form above a certain critical thickness, such that they mostly appear at the surface of the films, just below or even inside rutile outgrowths. The introduction of the buffer layer results in a dramatic effect in the behavior of AHEs: the AHE is suppressed for Co:TiO_2 films with buffer layer, while it is clearly present for Co:TiO_2 films without buffer layer. These results can be explained by a cluster-induced AHE [3]. For Co:TiO_2 films without buffer layer, Co clusters formed at the substrate/film interface give rise to an anomalous transverse Hall resistivity by polarizing nearby electrons. For Co:TiO_2 films without buffer layer, however, Co clusters placed outside the current path do not contribute to the associated transverse scattering. The very small value of the ratio of the anomalous Hall resistivity to the longitudinal resistivity (10^{-4}) also confirms that the AHE originates from Co clusters, since Co clusters polarize only nearby electrons. The results contained in Chapter 5 thus clearly show that the presence of AHE cannot be considered as a definite test for carrier mediated magnetism in dilute magnetic semiconductors.

It should be noyted that metallic impurity band conduction *and* ferromagnetism are observed simultaneously in both Co:TiO_2 films *with* and *without* a buffer layer. This is in principle possibly consistent with the viewpoint that metallic impurity conduction is the cause of carrier-mediated ferromagnetism [4]. However, the metallic impurity band conduction is found to co-occur with ferromagnetism due to *Co clusters*. It is therefore most likely that the phenomena of impurity band conduction and ferromagnetism are not related.

Chapter 6 mainly describes the effort of making magnetic tunnel junctions containing an ultrathin interfacial layer of Co:TiO_2 and their characterization. Since Co:TiO_2 thin films become defective (i.e. exhibit a growing amount of secondary phases) with increasing thickness, as can be seen in chapter 4 and 5, we aim to investigate the spin polarization of the charge carriers in ultrathin anatase Co:TiO_2 layers via spin-polarized tunneling in a magnetic tunnel junction (MTJ). It is found that the TMR and junction resistance of

epitaxial LSMO/STO/Co magnetic tunnel junctions changes significantly upon the insertion of ultrathin layers of Co:TiO_2 at the STO/Co interface. The magnitude of the TMR decreases but remains negative, while the junction resistance increases strongly. This is consistent with an effectively insulating and paramagnetic Co:TiO_2 adding to the tunnel barrier, with the tunneling electrons originating mostly from the Co:TiO_2/Co interface, and experiencing spin-flip scattering by paramagnetic Co in the Co:TiO_2.

In conclusion, the results from all studies combined support the picture that the origin of ferromagnetism in Co:TiO_2 is due to Co clusters, and not carrier mediation. Even though some of the characteristics of Co:TiO_2, such as the observed AHE, are suggestive of carrier mediated magnetism, it turns out that all magnetic phenomena described in this thesis can be traced back to metallic Co inclusions. Indeed, Co heterogeneity, which does not only manifest itself in cluster formation, seems to be unavoidable in these systems and responsible for many of their more exotic properties.

From our experiments, we cannot exclude possible contributions of uncompensated spins of CoO clusters, which play a role at low temperature [5]. Since our work mainly focuses on the origin of room temperature magnetism in Co doped TiO_2, we surely conclude that room temperature magnetism of Co doped TiO2 is due to Co clusters, which were detected with complementary characterization tools such as XMCD and EF-TEM. Our work cannot confirm that the origin of magnetism in the low temperature regime is solely from Co clusters, since our results lack the proof at low temperature. There may be uncompensated spin contributions due to CoO, or even carrier mediated interactions that play a role at low temperature. Nevertheless, the main contribution to magnetism is surely related to Co clusters, which screens the above possible scenarios.

For proving intrinsic DMS behavior, carrier mediated ferromagnetism such as tunable ferromagnetism and control of the magnetization direction by electric fields should be demonstrated by AHE measurements. This means that the ferromagnetism in intrinsic DMS should be induced by a low carrier density which is desirable for gate action. Enhanced AHE by increasing the carrier concentration is not a viable test for confirming carrier induced ferromagnetism, since metallic clusters can contribute via the polarization of nearby electrons. Therefore, the carrier density dependence of magnetic properties is the only robust method for confirming intrinsic ferromagnetism in DMS. So far, these phenomena have not yet been demonstrated in dilute magnetic oxides. For real DMS realization in oxides, there should also be a satisfactory theory to explain the carrier mediated ferromagnetism. Next, the materials should show electric control of ferromagnetism, large tunnel magnetoresistance effects, strong magneto-optical effects, and the existence of a spin-split band of carriers [6]. Since the coherently embedded spinodally decomposed phase can give rise to enhanced magneto optical and transport effects, element sensitive characterization methods, such as employed in this thesis, are a prerequisite for DMS research.

[1] H. Toyosaki, T. Fukumura, Y. Yamada, K. Nakajima, T. Chikyow, T. Hasegawa, H. Koinuma, and M. Kawasaki, Nat. Mater. **3**, 221 (2004).

[2] S. R. Shinde, S. B. Ogale, J. S. Higgins, H. Zheng, A. J. Millis, V. N. Kulkarni, R. Ramesh, R. L. Greene, and T. Venkatesan, Phys. Rev. Lett. **92**, 166601 (2004).

[3] S. X. Zhang, W. Yu, S. B. Ogale, S. R. Shinde, D. C. Kundaliya, W. -K. Tse, S. Y. Young, J. S. Higgins, L. G. Salamanca-Riba, M. Herrera, L. F. Fu, N. D. Browning, R. L. Greene, and T. Venkatesan, Phys. Rev. B **76**, 085323 (2007).

[4] J. M. D. Coey, M. Venkatesan, and C. B. Fitzgerald, Nature. Mater. **4**, 173 (2005).

[5] E. Eftaxias, and K. N. Trohidou, Phys. Rev. B 71, 134406 (2005)

[6] A. H. MacDonald, R. Schiffer, and N. Samarth, Nature Mater. **4,** 195 (2005).

Summary

Dilute magnetic semiconductors (DMS) can be tailored by doping a small amount of elements containing a magnetic moment into host semiconductors, which leads to a new class of semiconductors with the functionality of tunable magnetic properties. Recently, oxide semiconductors have attained interests for the possibility of developing room temperature dilute magnetic semiconductors. However, a large number of conflicting results have pointed towards both an intrinsic and extrinsic origin for ferromagnetism. In earlier studies of oxides in relation to DMS, the controversy originated mainly from imprudent conclusions relying on measurements of macroscopic magnetic properties without careful structural studies of secondary phases in the materials under investigation. This thesis describes the results of experiments with a broad set of complementary tools to investigate the origin of ferromagnetism in anatase Co:TiO_2, which shows room temperature magnetism and an anomalous Hall effect (AHE). In previous work carried out in the NanoElectronics group, ferromagnetism and the AHE at room temperature were observed in anatase Co:TiO_2 thin films grown under oxygen poor conditions, while the remanence and coercivity disappear for films grown under oxygen rich conditions.

We employed synchrotron based techniques, namely x-ray absorption spectroscopy (XAS) and x-ray magnetic circular dichroism (XMCD), which rely on the excitation of core-level electrons by soft x-rays. One of appealing features of these techniques for DMS studies is that they can provide element specific information on the electronic and magnetic properties of materials. Here, we focused on Co-derived electronic states.

We observed a suppressed XAS multiplet structure due to Co^{2+} ions at Co *L*-edges in oxygen poor samples, as compared to oxygen rich samples. This suppressed fine structure can be explained by a larger featureless Co metal contribution superimposed on the spectral features related to Co^{2+} ions. A Co metal contribution is confirmed by XMCD measurements, which show a featureless dichroism spectrum characteristic of metallic Co. Both oxygen poor and oxygen rich Co:TiO_2 showed a similar featureless XMCD spectrum, with the circular dichroism effect being significantly weaker for the oxygen rich case. These findings show that measurements of XAS *L*-edges alone may confirm the presence of ionic species, but cannot rule out secondary phases that may not yield a discernable fingerprint.

It can thus be concluded from the XAS/XMCD measurements that the Co distribution is heterogeneous for all Co:TiO_2 films, grown under oxygen rich as well as oxygen poor conditions. Co-heterogeniety, in the form of metallic clusters, is also confirmed by energy filtered transmission electron microscopy (EF-TEM). This means that metallic Co clusters are present in all the investigated films, and that they contribute to the ferromagnetism (as shown by XMCD) and AHE (as discussed below). We conclude that XMCD and EF-TEM are especially useful tools to check for heterogeneity in DMS research.

Using XAS, we also observed clear charge transfer (CT) satellite peaks at Co *L* edges for the thickest (160 nm) oxygen poor films. The CT peaks can be explained by the interaction of Co (3*d*) electrons with donor defect states in the band gap. It is known that Co segregates to defects sites, where it may form clusters. The observation that the CT peaks become stronger for thicker films, which exhibit a higher defect density resulting

from the relief of strain, may be related to defect states that are more energetically close to and significantly hybridized with the Co(3*d*) states. These findings also confirm that the electronic structure of Co *ions* is heterogeneous, related to defect states in Co:TiO_2 thin films.

The introduction of a TiO_2 buffer layer at the substrate/film interface, intended to reduce strain in Co:TiO_2, leads to a dramatic change of magnetic and structural properties in Co:TiO_2. First, a reduction of the density of Co clusters and a more homogeneous Co distribution in the thin films are confirmed by XRD, AFM and EF-TEM measurements. Second, the AHE is suppressed. These results can be explained by a cluster-induced AHE, also taking into account the results from EF-TEM analysis which showed that the *location* at which Co clusters form is markedly different for films with/without buffer layer. For Co:TiO_2 films without buffer layer, Co clusters formed preferentially at the substrate/film interface give rise to an anomalous transverse Hall resistivity by polarizing nearby electrons. On the other hand, for Co:TiO_2 films without buffer layer, Co clusters where mainly observed at the surface, such that they are placed outside the current path and do not contribute to the associated transverse scattering. The very small value of the ratio of the anomalous Hall resistivity to the longitudinal resistivity (10^{-4}) also confirms that the AHE originates from Co clusters, since Co clusters polarize only nearby electrons. Therefore, the presence of AHE cannot be considered as a definite test for carrier mediated magnetism in dilute magnetic semiconductors.

We also observed that metallic impurity band conduction and ferromagnetism occur simultaneously in both types of Co:TiO_2 films, with and without a buffer layer. Since the metallic impurity band conduction is found to co-occur with ferromagnetism due to *Co clusters*, we can conclude that the phenomena of impurity band conduction and ferromagnetism are not related.

Last, the spin polarization of the charge carriers in ultrathin anatase Co:TiO_2 layers is investigated by studying spin-polarized tunneling in a magnetic tunnel junction (MTJ) configuration. It is found that the tunnel magnetoresistance (TMR) and junction resistance of epitaxial LSMO/STO/Co magnetic tunnel junctions changes significantly upon the insertion of ultrathin layers of Co:TiO_2 at the STO/Co interface. The magnitude of the TMR decreases but remains negative, while the junction resistance increases strongly. This is consistent with an effectively insulating and paramagnetic Co:TiO_2 adding to the tunnel barrier, with the tunneling electrons originating mostly from the Co:TiO_2/Co interface, and experiencing spin-flip scattering by paramagnetic Co in the Co:TiO_2.

Yunjae Lee
August, 2010

Samenvatting

Verdunde magnetische halfgeleiders ("dilute magnetic semiconductors", DMS) kunnen worden verkregen door het toevoegen van een kleine hoeveelheid van een element dat een magnetische moment bevat aan een halfgeleider, hetgeen leidt tot de functionaliteit van regelbare magnetische eigenschappen. Halfgeleidende oxides zijn recent in de belangstelling komen te staan vanwege de potentie om verdunde magnetische halfgeleiders te ontwikkelen die hun magnetische eigenschappen behouden bij kamertemperatuur. Echter, een groot aantal conflicterende resultaten vormen aanwijzingen voor zowel intrinsieke alswel extrinsieke bronnen voor ferromagnetisme. In vroege studies naar oxides als DMS, bleef de controverse vooral bestaan doordat onvolledige conclusies werden getrokken uit metingen van macroscopische magnetische eigenschappen, zonder nauwkeurig onderzoek te doen naar de structurele eigenschappen van de materialen, met name met betrekking tot secundaire fases.

Dit proefschrift beschrijft de resultaten van experimenten die zijn uitgevoerd met behulp van een brede set van complementaire technieken, met als doel de bron van ferromagnetisme in anataas Co:TiO_2 te onderzoeken. Co:TiO_2 vertoond ferromagnetisme bij kamertemperatuur, gepaard gaande met een anomaal Hall effect (AHE). Eerdere studies uitgevoerd in de groep NanoElectronics wezen uit dat Co:TiO_2 dunne films gegroeid onder zuurstof arme condities bij kamertemperatuur ferromagnetisch zijn en AHE laten zien, terwijl de remanentie en coërciviteit verdwijnen indien de films onder zuurstof rijke condities worden gegroeid.

We hebben synchrotron technieken ingezet, met name x-ray absorption spectroscopy (XAS) en x-ray magnetic circular dichroism (XMCD), die functioneren via het exciteren van binnenschil-elektronen met zachte röntgenstraling. Eén van de meest aantrekkelijke aspecten van deze technieken voor het bestuderen van DMS systemen is dat element-specifieke informatie kan worden verkregen met betrekking tot de elektronische en magnetische eigenschappen. We focusseren hier op Co-gerelateerde elektronentoestanden. De van Co^{2+} afkomstige multipletstructuur in Co *L*-edge XAS spectra van zuurstofarme samples is in belangrijke mate onderdrukt ten opzichte zuurstofrijke samples. Deze onderdrukte structuur kan worden verklaard met een grotere structuurloze bijdrage afkomstig van metallisch Co aan de spectra. Een metallische Co bijdrage wordt inderdaad bevestigd door middel van XMCD metingen, die een structuurloos spectrum vertonen dat karakteristiek is voor Co metaal. Zowel zuurstofarme als zuurstofrijke samples laten een vergelijkbaar structuurloos spectrum zien, terwijl het XMCD effect beduidend zwakker is in het geval van zuurstof rijke samples. Deze bevindingen laten zien dat *L*-edge XAS spectra *alleen* wel geschikt zijn om de aanwezigheid van bepaalde ionen aan te tonen, maar niet om secundaire fases uit te sluiten die geen eenvoudig te herkennen spectra produceren.

We kunnen met behulp van de XAS/XMCD metingen concluderen dat de Co verdeling heterogeen is voor alle Co:TiO_2 films, gegroeid onder zowel zuurstofarme als zuurstofrijke condities. Co-heterogeniteit, in de vorm van metallische clusters, wordt ook bevestigd door energie gefilterde elektronenmicroscopie (EF-TEM). Dit betekend dat metallische Co-clusters aanwezig zijn in alle bestudeerde films, en dat deze clusters bijdragen aan het ferromagnetisme (zoals aangetoond met XMCD) en AHE (zie onder).

We stellen vast dat XMCD en EF-TEM bijzonder geschikte hulpmiddelen zijn om heterogeniteit te bestuderen in onderzoek naar DMS systemen.

Met behulp van XAS hebben we ook satelliet pieken, gerelateerd aan ladingsoverdracht ("charge transfer", CT), waargenomen in Co *L* edge spectra voor de dikste (160 nm) zuurstofarme films. Deze CT pieken kunnen worden verklaard met de interactie tussen Co (3*d*) elektronen en donor defecttoestanden in de band gap. Het is bekend dat Co naar roosterdefecten segregeert, waarna clustervorming kan plaatsvinden. De observatie dat de CT pieken in intensiteit toenemen voor dikkere films, waarin de defectdichtheid hoger is door relaxatie van het rooster, hangt mogelijk samen met defecttoestanden die energetisch dichtbij de Co(3*d*) toestanden liggen en hybridisatie vertonen met deze Co(3*d*) toestanden. Deze resultaten laten zien dat de elektronenstructuur van Co *ionen* ook heterogeen is, samenhangend met defecttoestanden in Co:TiO_2 films.

Het toevoegen van een TiO_2 bufferlaag aan het substraat/film grensvlak, bedoeld om de spanning in het Co:TiO_2 rooster te reduceren, leidt tot dramatische veranderingen van de magnetische en structurele eigenschappen in Co:TiO_2. Ten eerste wordt een vermindering van de dichtheid van Co clusters en een meer homogene verdeling van Co waargenomen met behulp van XRD, AFM en EF-TEM metingen. Ten tweede, is het AHE onderdrukt. Deze resultaten kunnen worden verklaard met een cluster-geïnduceerd AHE, met inachtneming van EF-TEM studies die aantonen dat de lokatie waar de clusters zich vormen sterk wordt beïnvloed door het toevoegen van een bufferlaag. Voor Co:TiO_2 films zonder bufferlaag, waarin Co clusters zich voornamelijk aan het substraat/film grensvlak bevinden, kunnen deze Co clusters aanleiding geven tot een transversale Hall weerstand via polarisatie van elektronen dichtbij de clusters. In films met bufferlaag bevinden de clusters zich echter vooral aan het oppervlak, zodat ze buiten het stroompad vallen en zodoende niet bijdragen tot transversale verstrooiing. De zeer kleine waarde van de longitudinale weerstand (10^{-4}) bevestigt ook dat het AHE van clusters afkomstig is, de Co clusters polariseren immers alleen dichtbij aanwezige elektronen. De observatie van AHE kan dus niet als een definitieve test worden beschouwd voor magnetisme overgedragen door ladingsdragers in verdunde magnetische halfgeleiders.

We hebben ook tegelijkertijd geleiding in een onzuiverheidsband en ferromagnetisme waargenomen, in beide types Co:TiO_2 films, met en zonder bufferlaag. Aangezien geleiding karakteristiek voor een metallische onzuiverheidsband tegelijk wordt waargenomen met ferromagnetisme veroorzaakt door *Co clusters*, kunnen we concluderen dat de fenomenen van geleiding in een onzuiverheidsband en ferromagnetisme niet aan elkaar zijn gerelateerd.

Ten slotte is de spin polarisatie van ladingsdragers in ultradunne Co:TiO_2 lagen onderzocht door middel van het meten van spin gepolariseerde tunnelstromen in magnetische tunnel juncties (MTJs). De tunnel magnetoweerstand ("tunnel magnetoresistance", TMR) een de weerstand van epitaxiale LSMO/STO/Co juncties blijkt sterk te worden beïnvloed door het toevoegen van een ultradunne Co:TiO_2 laag aan het STO/Co grensvlak. De grootte van de TMR neemt af maar blijft negatief, terwijl de weerstand sterk toeneemt. Dit is consistent met het toevoegen van een effectief isolerende en paramagnetische Co:TiO_2 laag, waarbij de tunnelende elektronen vooral vanaf het Co:TiO_2/Co grensvlak komen, en spin-flip verstrooiing plaatsvindt vanwege paramagnetische Co ionen in het Co:TiO_2.

Acknowledgements

When I am writing the acknowledgement, I realize that more than 4 year Ph.d life in the Netherlands finally came to an end. Time really flies. I still remember crystal clearly when I came to Enschede for the first time for an interview in January, 2006. I was pretty sure that a Ph.d career in the Netherlands would be great though I was much disappointed at the typical Dutch gloomy weather. As a matter of fact, it was not that bad. I'd really like to thank God for giving me this great chance to study in the Netherlands. I think I learned what I am and what you are more and more during the Ph.d life.

The first person I should and would like to thank is Michel, my supervisor during last 8 months. It was really fortunate to meet you during my Ph.d life. In 2007, I was in most hard time, losing my interest for Ph.d with the severe depression. I did not know how many times I murmured to myself during the day, saying that I'd like to give up and go back to Korea. However, you inspired me to go back into works again. I really enjoyed learning x-ray absorption in Sweden though meals were much more terrible than in the Netherlands. I cannot understand why Swedish food is served with fruit jam. I think that a supervisor should know how to guide a student to the right direction in academic as well as mental aspects. At this sense, you are the best supervisor I have ever met so far. I really appreciate your guidance.

I also like to thank Wilfred for being my promotor. I really appreciate your support for my graduation at Nanoelectronics group. I wish Nanoelectronics group a big success to be a leading group in the Nano science area for the future. I will always be proud that I am from NE group. I also like to thank Cock. You are always worrying whether or not I am doing good here whenever I meet you. Thanks, Cock.

It cannot be denied that I have got great supports from technicians for four years. Thijs saved my computer blown twice. Fortunately (?), I did not have any results till that time. Johnny always supported me in and outside the clean room. I enjoyed talking with you about your trip and personal things. I really appreciate your kindness. Martin helped me a lot when I worked on STM in the beginning. I asked many boring questions but you always helped me out like my big brother. I really appreciate you guys helps. I also thank Frank for supports in MASIF system. Rico also contributed to my Ph.d work significantly with nice ET-TEM images. Thanks, Rico. I also thank Karen, Thelma, Marion, Joyce, and Carolien for the support.

It was a great pleasure to see that Tamalika joined the faculty in Groningen. You always kept me not depressed on the situation I faced. I really appreciate your kindness during your stay in Twente. I am also happy to see that Saroj produced superb results in Nature. Do not forget that I was with you when you observed the result for the first time. I will miss our talk about every thing every late night. I wish you a big success in Sweden. Ivan! I cannot forget when you snored in the hotel. It was just the day before I presented in MMM. I really respect your wife, thinking of how she manages to do. I wish you a great success in Groningen.

Avijit is the only master student I supervised. In the beginning, we had a lot of troubles. Now, I believe you are one of my best friends. We proved our chemistry for solving problems during the work. I thank you for helping me the project out. I know you can do much better than me. Sandeep, Poor guy! It is a joke as you know. I wish you a great success in Japan. Tian! I hope that you produce a lot of results as much as you want.

Lucky! I wish you a good career in the Netherlands. I also like to thank the rest of previous and current members in NE group. Especially thanks to Byngchul.

I'd like to thank my parents. They suffered from four times surgery when I was far away. I am really indebted to my family members and also thank them for understanding me all the time.

I will go back to Korea. It means that working in the paradise comes to an end and working in the hell starts. I really enjoyed visiting fine arts museums and traveling last four years. I will miss all the memory in the Netherlands. There had been a lot of things happened during the past, though. However, I'd like to memorize good things here.

감사의 글

벌써 4 년 5 개월이란 시간이 흐르고 마치는 시간이 되었습니다. 네덜란드에 올때 분홍색 꿈을 가지고 왔는데...솔직히 지금은 어떤 색으로 바래졌는지 모르겠습니다. 되돌아 보니 꿈만 보고 달려온거 같은데, 제 자신이 부족하다는 것을 배우고 보이지 않던 평범한 것들에 대한 감사함을 배웠던 시간이었던거 같습니다. 앞으로 한국에서 그 감사함만 잊지 않는다면 비록 원래 가졌던 학문적인 꿈은 놓게 됐지만 신앙과 제 삶속에서 유학생활이 헛되지 않았음을 느낄거라 믿습니다.

트벤테 공대를 알게 해준 태철. 니가 없었다면 여기 못왔겠지? 포스코에서 잘 자리잡은거 같아 보기 좋다. 캠브리지 가기전까지 많이 도와주신 박병국 박사님과 사모님, 그리고 1 년 반 남짓 같이 네덜란드에 있었던 병철 선배님과 사모님께 감사드려요. 힘들때마다 격려해주신것 너무 감사드립니다. 선배님들에게 부끄럽지 않은 후배가 되어야 하는데 그러지 못해 죄송스럽고 아쉽네요.

박사 과정 동안 가장 많은 힘이 되준 용삼. 코넬에서 좋은 연구 많이 하고, 잘 자리 잡았음 좋겠다. 너 만나러 이타카까지 가다니, 같이 뉴욕갔던게 가끔 생각나네. 이제 졸업할 상훈, 훌륭한 엔지니어 상범, 애리조나에서 고생하고 있는 근용, 과기원 엑스선 실험실 노도영 교수님 및 선후배님들에게도 감사 드려요. 트벤테 후배 중석, 마인쯔로 떠난 대준, 그리고 충렬... 많이 못 챙겨줘서 미안하다. 좋은 결과 얻고 졸업하길.

뮌스터 교회 김지훈 목사님과 사모님, 강철구 목사님 내외분, 그 외 목사님들과 집사님들, 뮌스터 복음 교회 식구들, 청년들에게 감사 드려요. 국경을 넘어 교회 갈때 마다 잘 챙겨준 창훈 형, 혜언 누나, 소일, 예영, 선향, 지승, 지혜, 의영 외 모두 고맙습니다. 마지막에 친해진 재신이, 그리고 성재, 요즘 너 때문에 형이 기도한다. 이런적 없는데 말이다. 비록 네덜란드에 살았지만 유학 생활의 반 정도는 독일에서의 기억이 남아있네요. 아마 여러분들에겐 제가 잠시 스쳐지나간지 모르겠지만 저한테는 한국 말로 이야기하고 정을 나눴던 거의 모든 시간들이었습니다. 뮌스터 알트슈타트를 걷는 걸 참 좋아했는데...많이 그리울 듯 하네요.

한국 갈 때 마다 반갑게 맞아 주시는 이웅천 목사님, 윤정희 사모님, 전성수 목사님, 김마리아 사모님 감사드려요. 네덜란드 엔스헤데까지 놀러온 예나, 그리고 항상 응원해주는 슬지, 수빈, 우진이 고맙다. 유럽에서 만나기만 하면 싸운 기억밖에 없는 주희, 트로싱엔에서 잘 졸업하길. 한국에서 볼때 마다 항상 느끼지만, 영주 누나 희성 형, 규언 형, 방렬 형 고마와요. 예전 여디디야 시절이 그립네요. 하노버까지 왔는데 못만난 20 년 지기 쨈, 지금 생각해보니 많이 미안하네. 빨리 좋은 여자 만나 결혼하시길 그리고 우리 우정은 변치 않을거라 믿소. 홍식이에게도 많이 미안하네. 승엽아 결혼 축하해, 철순아 숙현아 항상 고맙다. 태어날 아이 이름은 뭐야? 가족 같은 성일, 신애, 기원이에게도 고마움을 전합니다.

저 없는 동안 많은 수술을 받으신 아버지, 그리고 어머니 감사드려요. 아들은 아버지가 얼마나 아프셨는지 알지 못합니다. 죄송하네요. 그리고 사랑합니다. 그리고 가족들에게 미안함을 전해요. 누나, 매형, 형, 형수님, 그리고 특히 동생, 결혼식때 못가서 미안해. 그리고 사랑스런 조카들 항상 건강하길 기도합니다.

2010 년 8 월 10 일, 네덜란드 엔스헤데에서

List of publications

1. **Y. J. Lee**, M. P. de Jong, R. Jansen, "Magnetism and heterogeneity of Co in anatase Co:TiO_2 magnetic semiconductor", **Appl. Phys. Lett** 96 082506 (2010).

2. **Y. J. Lee**, A. Kumar, I. J. Vera Marún, M. P. de Jong, R. Jansen, "Magnetic tunnel junctions with Co:TiO_2 magnetic semiconductor electrodes", accepted , **IEEE Trans. Mag**. (2010**)**.

3. **Y. J. Lee**, S. S. Kim, S. P Lee, H. H. Lee, D. Y. Noh, "High-Q X-ray scattering study of $In_xGa_{1-x}N$/GaN multi-quantum wells" **Thin Solid Films** 515, 5641 (2007).

4. S. N. Lee, J. Son, H. Paek, T. Sakong, W. Lee, K. Kim, E. Yoon, J. Kim, Y.H. Cho, **Y. J. Lee**, S. S. Kim, D. Y. Noh, O. Nam, Y. Park, "Effect of thermal damage on optical and structural properties on InGaN/InGaN multiple quantum wells grown by MOCVD", **J. of Crystal Growth**, 275, e1041-1045 (2005).

5. S. N. Lee, J. K. Son, H. S. Paek, T. Sakong, J. S. Kwak, K.H. Ha, O. H. Nam, and Y. Park, Euijoon Yoon, J. Y. Kim, and Y.-H. Cho, S. S. Kim, **Y. J. Lee**, D. Y. Noh, "Investigation of thermal degradation on structural and optical qualities of InGaN/InGaN MQWs," **Institute of Physics Conference Series**, Vol. 184, pp. 377 (2004)

6. Sung-Nam Lee, J. K. Son, H. S. Paek, T. Sakong, W. Lee, K. H. Kim. S. S. Kim, **Y. J. Lee**, D. Y. Noh, E. Yoon, O. H. Nam Y. Park, "Grwoth pressure dependence of residual strain and threading dislocations in the GaN layer", **Phys. Stat. Sol (c)**, 1, No 10, 2458-2461 (2004)

<u>To be submitted</u>

7. **Y. J. Lee**, *et al* "Anomalous Hall effect and impurity band conduction in Co:TiO_2 magnetic semiconductor", to be submitted to Phys. Rev. B.

8. **Y. J. Lee**, M. P. de Jong, W.G. van der Wiel, "Electronic structure of Co^{2+} ions in anatase Co:TiO_2: hybridization and metal-to-ligand charge transfer effects", to be submitted to Appl. Phys. Lett.